



PERIODIC PROPELLER FORCES IN UNSTEADY FLOW

by

NEAL ALVIN BROWN

S.B., Webb Institute of Naval Architecture
(1957)

S.M., Massachusetts Institute of Technology
(1959)

SUBMITTED IN PARTIAL FULFILLMENT

OF THE REQUIREMENTS FOR THE

DEGREE OF DOCTOR OF

PHILOSOPHY

AT THE

MASSACHUSETTS INSTITUTE OF TECHNOLOGY

June, 1964

Signature of Author.....
Department of Naval Architecture, June 2, 1964

Certified by.....
Thesis Supervisor

Accepted by.....
Chairman, Departmental Committee
on Graduate Students

ABSTRACT

PERIODIC PROPELLER FORCES IN UNSTEADY FLOW

by

Neal Alvin Brown

Submitted to the Department of Naval Architecture and Marine Engineering on June 2, 1964 in partial fulfillment of the requirements for the degree of Doctor of Philosophy.

Ship screws experience vibration inducing periodic forces at blade frequency and its multiples because of their operation in the circumferentially non-uniform flow field of the wake. These forces are presently computed on the basis of either quasi-steady analyses or stripwise application of the Sears function for the unsteady lift of a two-dimensional airfoil subjected to sinusoidal gusts. The quasi-steady analyses are correct only at zero frequency while the unsteady strip theory is presumed correct only at high frequencies because of the neglect of three-dimensional effects in the latter.

Using a vortex sheet model, the linearized integral equation for the bound vorticity of the blades is derived. This is simplified by approximations analogous to those made by Reissner for the plane wing. The difference between the downwash in the three and two-dimensional flows is determined in a vortex line model of the propeller. The analysis proceeds on the basis of computing a correction to the two-dimensional unsteady strip theory to account for three-dimensional effects.

The downwash difference in the vortex line model is shown to be calculable for any harmonic number by harmonic analysis of certain functions which represent the angular distribution of the contributions of the shed vorticity to the induced velocity.

The need for experimental data pertinent to the evaluation of the theoretical analysis is noted. An instrumented shafting system for the direct dynamic measurement of blade frequency thrust and torque in the propeller tunnel is described. Results obtained in tests in a carefully mapped axial velocity field with a blade order harmonic content are presented.

Numerical results show that the three-dimensional analysis is identical with the steady flow lifting line at zero frequency and converges to the strip theory result at high harmonic numbers. For the case considered, the strip theory yields a thrust only 15% greater than the three-dimensional analysis at blade frequency. Comparison with the results of computations made with the measured flow field show that the experimental results are bracketed by the predictions of the two and three-dimensional analyses.

Thesis Supervisor: Frank M. Lewis
Title: Professor of Marine Engineering (Emeritus)

ACKNOWLEDGEMENT

The author wishes to express his appreciation to the following individuals and organizations:

Professor Frank M. Lewis for his guidance and encouragement as thesis supervisor.

Professor Justin E. Kerwin for his valuable assistance and encouragement as thesis advisor.

Professor Ir. J. Gerritsma and his staff at the Shipbuilding Laboratory, Delft, for their interest, aid and cooperation which made possible the experimental part of this work.

Mr. Kai Chang for his assistance with computer programming.

This work was accomplished, in part, through the use of the facilities and services of the M.I.T. Computation Center.

TABLE OF CONTENTS

| | Page |
|--|------|
| TITLE PAGE | i |
| ABSTRACT | ii |
| ACKNOWLEDGEMENT | iii |
| TABLE OF CONTENTS | iv |
| LIST OF FIGURES | v |
| NOMENCLATURE | viii |
| CHAPTER I INTRODUCTION | 1 |
| CHAPTER II THE INTEGRAL EQUATION FOR THE BOUND VORTICITY | 15 |
| CHAPTER III THE VORTEX LINE MODEL | 28 |
| CHAPTER IV METHOD OF SOLUTION | 44 |
| CHAPTER V COMPUTATION OF THE DOWNWASH DIFFERENCE MATRIX | 58 |
| CHAPTER VI AN APPROXIMATION FOR LOW HARMONIC NUMBERS | 76 |
| CHAPTER VII MEASUREMENT OF BLADE FREQUENCY THRUST AND TORQUE IN THE PROPELLER TUNNEL | 77 |
| CHAPTER VIII RESULTS AND CONCLUSIONS | 106 |
| REFERENCES | 123 |
| APPENDICES | 126 |
| A. Derivation of the Circulation of an Airfoil in Sinusoidal Gusts | 127 |
| B. Form of the Radial Vorticity Integrand for Small φ at $\eta = 1$ | 131 |

LIST OF FIGURES

| CHAPTER II | Page |
|--|------|
| 2.1 Coordinate Systems | 17 |
| 2.2 Coordinate Systems Projected View | 19 |
| 2.3 Vorticity Components and Non-Uniform Inflow | 22 |
| CHAPTER III | |
| 3.1 Vortex Line Model for Downwash Difference | 30 |
| 3.2 Discrete Approximation of Continuous Radial Circulation Distribution (Schematic) | 33 |
| 3.3 Vorticity Panel (Schematic) | 36 |
| CHAPTER IV | |
| 4.1 Phase Shift Due to Blade Skew | 53 |
| 4.2 Lift Coefficient - Flat Plate 2-D Airfoil in Sinusoidal Gusts. | 55 |
| 4.3 Circulation - Flat Plate 2-D Airfoil in Sinusoidal Gusts. | 57 |
| CHAPTER V | |
| 5.1 Intersection of Helices with a Plane Through the Axis at Constant Angle θ | 60 |
| 5.2 Sum Function vs. Angle for the Panel Between $\eta_1 = 1.5$ and $\eta_2 = 1.6$ | 63 |
| 5.3 Number of Turns Summed - Streamwise Vortex Lines | 67 |
| 5.4 Number of Turns Summed - Radial Vorticity | 67 |
| 5.5 Sum Function vs. Angle for the Panel Between $\eta_1 = 0.95$ and $\eta_2 = 1.05$ | 70 |

| | |
|---|------|
| CHAPTER VI | Page |
| 6.1 Harmonic Analysis of the Downwash Difference | 74 |
| CHAPTER VII | |
| 7.1 Flow Regulator - Delft Tunnel | 78 |
| 7.2 Upstream End of Tunnel Showing Velocity Control Valve Stems and Slip Rings | 80 |
| 7.3 Drive Line - Shafting System | 83 |
| 7.4 Dynamometer | 88 |
| 7.5 General View of Instrumentation | 91 |
| 7.6 Intensity Modulation Control Device for Phase Angle Measurement | 93 |
| 7.7 Axial Velocity Field - Harmonic Components | 97 |
| 7.8 Axial Velocity Field Fourth Harmonic Amplitude | 99 |
| 7.9 Axial Velocity Field Fourth Harmonic Phase Angle vrs. Mean Velocity | 100 |
| 7.10 B - Series Type Screw | 102 |
| 7.11 Experimental Results - Blade Frequency Thrust and Torque | 104 |
| CHAPTER VIII | |
| 8.1 Computed Blade Thrust Amplitude for Propeller with 110 0.59 Expanded Area Ratio | |
| 8.2 Computed Blade Thrust Phase for Propeller with 111 0.59 Expanded Area Ratio | |

| CHAPTER VIII (Continued) | | Page |
|--------------------------|--|------|
| 8.3 | Computed Blade Thrust for Propeller with 0.295 Expanded Area Ratio | 113 |
| 8.4 | Reduced Frequency Distribution | 115 |
| 8.5 | Comparison of Blade Thrust Predicted by 3-D and 2-D Analyses | 117 |
| 8.6 | Comparison of Computed and Experimental Results | 119 |

NOMENCLATURE

| | | |
|-----------------------------|---|--|
| A | = | area |
| \bar{A}_n | = | complex coefficient of n th term of circulation series |
| \bar{a}_m | = | complex coefficient of m th term of inflow perturbation series. |
| b | = | blade section semi-chord length |
| \bar{C}_L | = | complex lift coefficient |
| CI,SI | = | cosine and sine integral functions |
| \vec{D} | = | vector distance defined in (2.5) and (2.6) |
| f_n | = | n th circulation series function |
| f_s, f_r | = | streamwise and radial vorticity kernel functions defined in (2.10) and (2.11). |
| \bar{F} | = | complex lift function defined in (4.19) |
| \bar{G} | = | complex circulation function defined in (4.20) |
| h | = | blade section mean surface offset; also summation increment as in (5.8). |
| i | = | $\sqrt{-1}$, the imaginary vector |
| i, j | = | panel indices |
| $\vec{i}, \vec{j}, \vec{k}$ | = | unit vectors in the (x, y, z) directions |
| \bar{I}_s, \bar{I}_r | = | complex integrals over vorticity panels defined in (5.2) and (5.6). |
| J | = | propeller advance coefficient, defined in Figure 7.11. |
| J_0, J_1 | = | Bessel functions of the first kind |
| k | = | reduced frequency, defined in (4.15). |
| k | = | blade index |

| | | |
|-----------------------------------|---|--|
| K | = | number of blades |
| K_0, K_1 | = | modified Bessel functions of the second kind |
| K_T, K_Q | = | thrust and torque coefficients, defined in Figure 7.11 |
| l | = | wave length of disturbance |
| m | = | downstream summation index; term index in radial polynomial representation of inflow perturbation. |
| M | = | a maximum value of m for downstream summation |
| n | = | circulation series term index |
| n | = | normal coordinate in curvilinear (s, r, n) system |
| N | = | harmonic number |
| p | = | $\lambda/r = \tan \beta$ |
| r | = | radial coordinate in (x, r, θ) and (s, r, n) systems |
| r_H | = | propeller hub radius |
| R | = | propeller radius |
| s | = | streamwise coordinate in (s, r, n) system |
| s_L, s_T | = | streamwise coordinates of leading and trailing blade edges |
| s_m | = | streamwise coordinate of blade midchord as fraction of semichord length. |
| S_s, S_r | = | streamwise and radial vorticity sum functions defined in (5.5), (5.6) and (5.7). |
| t | = | time |
| u | = | axial perturbation velocity |
| $\vec{u}_s, \vec{u}_r, \vec{u}_n$ | = | unit vectors in the (s, r, n) directions |
| U | = | streamwise inflow velocity relative to a blade section |
| V | = | volts |

- \bar{w} = complex velocity normal to helical surface
 \vec{w} = induced velocity vector
 \bar{w}_N = N th harmonic complex normal inflow perturbation velocity
 \bar{w}_{2D} = complex two dimensional normal downwash velocity
 \bar{w}_{3D} = complex three dimensional normal downwash velocity
 \bar{w}_{DD} = $\bar{w}_{3D} - \bar{w}_{2D}$, the downwash difference defined in eq. (3.1)
 \bar{w}_{2D*} = complex two dimensional normal downwash due to shed vorticity
 \bar{W} = complex downwash difference due to unit circulation
 x = axial coordinate of (x,y,z) and (x,r,θ) systems, positive downstream
 y = coordinate along axis coinciding with reference line in index blade in (x,y,z) system
 z = third coordinate in (x,y,z) system
 α = initial value of argument in function to be summed, eq. (5.8)
 β = hydrodynamic pitch angle
 $\bar{\gamma}_s, \bar{\gamma}_r$ = complex streamwise and radial vorticity strength
 $\vec{\gamma}$ = vorticity vector
 $\bar{\Gamma}$ = complex circulation
 θ_k = angular coordinate of k th blade
 η = e/r
 θ = angular coordinate in (x,r,θ) system, measured from the start of a helix

| | |
|----------------------|--|
| θ_L, θ_T | = angular coordinates of the leading and trailing blade edges |
| λ | = J/π , hydrodynamic advance coefficient |
| $\mu\epsilon$ | = micro strains |
| ρ | = dummy r coordinate, fluid mass density |
| σ | = dummy s coordinate |
| φ | = dummy Θ coordinate |
| ϕ | = angular coordinate measured from reference line of index blade |
| ψ | = transformed radial variable defined in (4.3) |
| ω | = circular frequency |
| Ω | = angular velocity of propeller |

CHAPTER I

INTRODUCTION

Hydrodynamic Propeller Forces Inducing Ship Vibration

The periodic vibration generating forces acting upon the hull of a ship are due in general to the unsteady hydrodynamic interactions of the hull and propellers. These interaction forces may be classified as primary and secondary, each category consisting of both surface and bearing forces; the secondary forces being not necessarily of lesser importance than the primary ones. These forces act at the blade frequency given by the product of the rotational speed and the number of blades, and higher harmonics of this frequency.

Of the primary forces, the steady thrust and torque producing circulatory loading of the screw, plus the fluid displacement caused by the bulk of the blades create a pressure field which rotates with the screw. Relative to the screw this pressure field is time invariant, but relative to the fixed hull the flow is unsteady. The pressure field rotating with the screw sweeps over nearby hull and appendage surfaces resulting in periodic forces. These are strongly influenced by the clearance between the propeller and affected surfaces because of the attenuation with distance of the periodic pressure field. The forces of this origin can thus be reduced to any desirable level by increased clearance where this is possible.

The second of the primary forces, the bearing forces, are due to the operation of the propeller in the circumferentially non-uniform velocity field of the ship's wake. The non-uniformity is produced by the frictional boundary layer in the flow about the hull primarily, but also to some extent by the potential flow. This wake flow is steady relative to the hull but unsteady relative to the rotating screw. In particular, the flow field relative to a screw blade is periodic in one revolution. The inflow velocity at a point of a blade is thus expressible in a Fourier series in time or angular position of the screw. The wake flow corresponding to any particular harmonic is, therefore, sinusoidally distributed spacially and thus the blade can be considered to be experiencing a continuous sequence of sinusoidal gusts.

The periodic forces on each blade due to the resulting unsteady lift are summed over all the blades of the propeller. Because of the symmetrical blade arrangement, these summations are carried out selectively, resulting in general in six components of forces and moments acting on the propeller shaft at the blade frequency and the higher harmonics. The ship structure or machinery is excited by these forces either at the stern tube bearing or through the shaft itself.

These forces are not greatly effected by propeller-hull clearance due to the persistence of the wake and require changes in either the hull form or propeller form in order to reduce the non-uniformity or its net effect on the screw.

The secondary interaction forces are more difficult to describe or observe. One of these may be considered the forces on the hull resulting from the impingement of the pressure fields due to the unsteady lift of the propeller in the non-uniform inflow. Another class, perhaps more important than the first, are the bearing forces resulting from the presence of the hull and appendages in the vicinity of the operating propeller. These may be presumed due to the interference of these bodies with the flow patterns resulting from the steady circulation and blade thickness displacement of the screw. Little is known of these effects.

We shall here be concerned with the bearing forces due to non-uniformity of the inflow field.

Experimental Studies

A considerable number of experimental investigations have been carried out measuring the various components of propeller induced vibratory forces. The pioneering work in this area was done by Lewis (1) who revealed the salient characteristics of the phenomena involved by force measurements on a self-propelled model of a twin screw passenger vessel. Total force measurements giving the sum of the bearing and surface forces were made, the direction of the forces being set at will by adjustment of the relative angular positions of the two screws. The surface forces were measured separately by driving the propellers from a following model with no physical contact between the screws and the forward model on which the forces were measured. The bearing forces were found by vector subtraction of the measured surface forces from the measured total forces. These experiments revealed that for twin screw ships the surface forces

were larger than the bearing forces, being primarily due to loads on the bossings or struts in close proximity to the screw.

More recently, Lewis and Tachmindji (2) have applied these same basic techniques to the measurement of vibratory forces on models of single screw ships and, in two cases, to measurements on full scale vessels. Results of model tests showed the surface and bearing forces to be of approximately the same magnitude.

Measurement of bearing forces on self-propelled models has been developed to a high degree by Wereldsma (3). The strain gage instrumentation used has high natural frequencies making measurement of higher harmonics of the bearing forces possible. Special filtering techniques for the rejection of noise are necessary. Extensive tests with this apparatus on a model of a single screw tanker have yielded results showing the dependence of bearing forces on the number and shape of propeller blades, the loading of the screw, the aperture shape and clearance, and loading condition of the ship. (4)

The effects of radical variations in ship after body shape and corresponding propeller form on the thrust and torque fluctuations, as caused by changes in wake distribution and clearance, have been studied by van Manen and Kamps (5). Recently a propeller dynamometer has been developed by this group which is capable of measuring all six components of bearing force simultaneously (6).

Measurements of the dependence on blade area of the blade frequency thrust and torque variations with four bladed propellers and

side force and bending moment with five bladed propellers have been made extensively for an ore carrier type vessel by Krohn (7) (8). His findings of increased bearing force with increased blade area are in agreement with those of van Manen and Wereldsma (4). Comparative tests on identical ship and propeller models carried out with the equipment of Wereldsma and Krohn show differences, however, that point to insufficient natural frequency in torsion in the latter (9).

Experimental work on propeller forces in the propeller tunnel has been up to now limited primarily to the investigations of Lewis (10). Here forces on a strut in proximity to the screw are measured by an apparatus similar in principle to that used in the early model tests. Primary surface forces on the strut are measured while the screw runs under different loading conditions in open water. The insertion of wake producing screens in the flow ahead of the propeller yields the surface force on the strut due to the unsteady pressure on the propeller, one of the secondary interactions, by vector subtraction of the primary surface force.

The screw may be run on a shaft fixed in the strut while driven by the tunnel shaft through a flexible coupling. The bearing forces, at least the one perpendicular to the plane of the strut, are determined by vector subtraction from the net resulting measured force, the force obtained without connection between the propeller and strut. In open water the interference bearing force is determined in this manner. With wake producing screens the primary bearing force is determined by vector subtraction of the open water forces

from the measurements.

Propeller tunnel measurements have been made by Tachmindji and Dickerson (11) of thrust fluctuations at blade frequency and higher harmonics for a propeller in the stream of a wake producing hydrofoil. There is some doubt concerning the validity of the results because of the low natural frequency of the shafting system.

Analytical Investigations

The earliest computations of bearing forces made use of quasi-steady analyses. In these the instantaneous values of the blade forces are determined as a function of blade position as though the flow were steady relative to the blade. The variations with time which in the significant sense produce unsteady effects are ignored.

A lifting line model for quasi-steady analysis is sometimes used. Here the chordwise variation of the inflow is neglected, the velocities being determined only along the lifting line. Steady state means are used to compute induced velocities. Other methods have been proposed which use the steady state operating characteristics of propellers as determined from experiment. These so called chart methods determine the thrust and torque per blade on the basis of various averages of the inflow velocity over the radius and chord of the blade for various blade positions.

The quasi-steady methods generally yield bearing forces which are much larger than are actually measured except perhaps in some full scale measurements, the validity of which are questionable.

These procedures are illogical at the high frequencies to which they are applied, as is well known, yet they continue to be proposed.

The first consideration of the propeller in a circumferentially non-uniform flow as an unsteady phenomena was probably that of van Manen (12). In his simple analysis, the inflow variations were taken equivalent to rigid body pitching and heaving motions of the blade sections in a uniform flow. This unrealistic model was not used in connection with bearing forces however.

The definitive study of the unsteady strip theory computation of propeller thrust and torque variations in circumferentially non-uniform inflow was put forth by Ritger and Breslin (13). Here the unsteady section lift is found by the stripwise application of the Sears function for the lift of an airfoil in sinusoidal gusts, according to the local values of the reduced frequency. Unfortunately, there appears to be an arbitrary application of some three dimensional correction factors to the lift from steady propeller analyses. Also, there is considerable attention paid to such admitted second order effects as surge, which unnecessarily complicates the analysis. The Sears function is considered as a means of modifying the instantaneous angle of attack for a lifting line model of the propeller in order to modify the quasi-steady analysis. The effect of blade skew is apparently not considered.

A comparison of the Ritger-Breslin method with experimental results has been carried out by Tsakonas and Jacobs (14). Blade frequency thrust measurements made on a full size single screw ship

show rough agreement with the unsteady strip theory. Measurements on a 1/25 th scale model show rough agreement with quasi-steady theory. The wake distribution of the model is used and only amplitudes are compared in both cases. The writer questions the validity of these comparisons as well as the accuracy of the data used.

Amplitude comparison of results of the propeller tunnel blade frequency thrust measurements of Tachmindji and Dickerson with the theoretical prediction show better agreement with the quasi-steady model than with the unsteady strip theory. The experimental results, however, show generally greater amplitude than the quasi-steady results, further casting doubt upon the value of these measurements.

Krohn, in conjunction with his experiments, uses an unsteady strip theory utilizing the Sears function, but arbitrarily modifies the resulting lift at each section by application of the Eckhardt and Morgan steady flow camber correction coefficients. Comparison of the measured and computed blade frequency thrust amplitudes for a four blade propeller show the computed values to be less than the experimental, while the reverse is true for the torque. For a five blade propeller there are good agreements between computed and experimental side force and bending moment amplitudes. No phase information is given in either case.

Lewis, in conjunction with his tunnel experiments has made strip theory computations using the Sears function without extraneous corrections. Phase shifts due to skew are also considered. Computations of the side forces due to both the third and fifth harmonics

of the flow field for a four blade propeller are in good agreement both in amplitude and phase with the results of experiment. (10)

The integral equation relating the lift and downwash distributions on the blades of an oscillating propeller has been derived and investigated mathematically in great detail by Hanaoka (15). Blades of finite aspect ratio are considered, and the integral equation is derived by the use of both the acceleration potential and vortex theory. A systematic reduction to a lifting line approximation is made by application of a variation principle due to Flax. The properties of the kernel function and the finite contributions of the singularities are carefully examined. The solution, however, is left to numerical processes but due to the extremely complex forms is impractical to obtain, and perhaps not worthwhile.

Joosen (16) has derived the induced velocities from a vortex model. When expressed in Taylor's series in the radial coordinate an integro-differential equation for the radial circulation distribution results after lifting line approximations are made. Unfortunately, no further development is made and no results are given.

Prompted by the poor agreement between the available experimental results and the strip theory analysis Shioiri and Tsakonas (17) have recently attempted a three dimensional analysis. The integral equation for the finite bladed propeller in unsteady flow is derived using the acceleration potential. The kernel is simplified and the surface integral equation reduced to a line integral by the use of a Weissinger approximation.

A line of pulsating dipoles at the $1/4$ chord positions of the blades induces velocities at a line at the $3/4$ chord positions where the boundary condition is satisfied. For steady flow such an arrangement duplicates the thin airfoil performance in two dimensional flow and is approximately correct in three dimensional flow if the aspect ratio is not too low. This arrangement is used here as an approximation to the unsteady gust flow. In two dimensions the resulting lift is in exact agreement with the Sears function only at zero reduced frequency, and the two slowly diverge with increasing reduced frequency. At $k = 1.3$ both the real and imaginary parts of the lift by the Weissinger model are approximately fifty percent of the corresponding Sears values.

Due to these discrepancies this model is not expected to yield accurate results at the reduced frequencies normally encountered. Rather the authors apply the model in both a three dimensional and stripwise manner for comparative purposes. In this way it is hoped to achieve a measure of the reliability of the strip theory and the relative importance of three dimensional effects.

Numerical results are given which show a large difference between three and two dimensional results, at blade frequency for a four bladed propeller the three dimensional lift amplitude is but half the two dimensional, for example, though the phase angles are in good agreement. This seems a rather large correction at the reduced frequencies considered, and it is not known whether this is due to the peculiarities of the model or perhaps the rather unusual sector form of the blades used to facilitate computation.

General Method of Proposed Analysis

In this work the writer has attempted to develop a method of analysis based on a realistic model in which those assumptions and simplifications which are made are readily appreciated and understood. The analysis is guided by a desire to produce useful results, calculable by methods familiar in the field of engineering analysis, and capable of demonstrating the relative applicability of the various simple approximations in use.

In Chapter II the integral equation relating the bound vorticity of the propeller blades to the normal perturbation velocity in a circumferentially non-uniform inflow is derived. This is based on the familiar vortex model in which the downwash expressions involving the kernel functions are determined by Biot-Savart integration. The relations between the vorticity components on the blades and shed into the race are specified.

The integral expression for the downwash is seen to be extremely intractable in its full form. In Chapter III the downwash is written in the form of the two dimensional strip theory downwash plus a "downwash difference" due to three dimensional effects. This involves no approximations and the two dimensional representation, which presumably accounts for the greater part of the unsteady effects at high frequencies, is well known and easily applied.

The downwash difference correcting the strip theory is then approximated by a simplified model of the vortex systems which is physically reasonable. This model yields the lifting line result at zero frequency or steady flow and is seen to be analagous to the Reissner model for the oscillating plane wing.

The actual practical means of solution of the problem as represented are outlined in Chapter IV. The radial distribution of circulation is expressed in a series with complex coefficients which are to be determined. The model is divided into discrete steps in order to yield a matrix of complex downwash difference influence coefficients. The circulation and lift are shown to be those developed by the two dimensional strips if subjected to the inflow corrected by the downwash difference. Writing the boundary condition leads to a set of complex simultaneous equations for the circulation series coefficients, thus completing the approximation to the original integral equation and its inversion.

The computation of the influence coefficients, which in effect represent the kernel function of the integral equation, constitute the major part of the actual solution of the problem. In Chapter V a general method is developed whereby the influence coefficients may be obtained for any harmonic component of the inflow by harmonic analysis of certain computed functions. These functions represent the angular distribution of the contributions to the downwash difference.

Advantage is taken of the nature of the induced velocities revealed in Chapter V to provide an approximation to the induced velocities which is reasonably valid for low harmonic numbers. The reasoning of Chapter VI provides a basis for the logical application of the readily computed steady state induced velocities for the solution of the low frequency unsteady case.

The Application of Experimental Results

A great amount of confusion concerning the accuracy of various methods of determining the propeller bearing forces has resulted, in the writers opinion, from the use of inaccurate and/or irrelevant test data for comparative purposes. In particular, the writer objects to the comparison of the bearing forces measured on self-propelled models with the computed forces based on the measured model wake distributions.

A reasonable doubt exists as to whether the wake distributions measured in the absence of the screw are the same as those found with the screw working. The loaded propeller applies a reduced pressure field to the hull in its vicinity, which may be expected to affect the boundary layer at the stern, especially if separation is present.

Perhaps more important is the fact that propeller bearing forces result from the presence of the hull and appendages in the vicinity of the screw. These secondary interference forces are shown in the results of Lewis' experiments (10) to be of the same order of magnitude as the primary surface forces. With the usual clearances, therefore, these may well be of the same magnitude as the primary bearing forces.

The same objections may be raised to the use of full scale data for the evaluation of bearing force calculation methods, but in addition there is the objection that such data is often inaccurate due to the poor dynamic response of the full scale

mechanical systems. The natural frequencies of the propeller and shafting systems are often so low in full scale that effects at blade frequency are considerably magnified. With low input impedance the mass and damping of the screw also enter in to further degrade the measurements.

Bearing force measurements in self-propelled models are valuable for investigation of the total effects involved. However, the various phenomena present must be studied separately and in the absence of more inclusive theory we must design experiments to evaluate the theories that we have and not attempt such evaluation with measurements made in the presence of unaccounted influences which are possibly as great as the phenomena of interest. To this end more fundamental studies in the propeller tunnel of the bearing forces due to non-uniform flow and also interference effects are suggested. In Chapter VII a measurement system for the dynamic testing of propellers in a known velocity distribution in the propeller tunnel is described. Direct measurements of blade frequency thrust and torque at high speed is accomplished with a shafting and dynamometer system carefully designed for proper frequency response. In Chapter VIII the results of the experiments performed are used to evaluate the theoretical computation schemes proposed.

CHAPTER II

THE INTEGRAL EQUATION FOR THE BOUND VORTICITY

Basic Assumptions

The propeller is presumed to be operating in a frictionless and incompressible fluid, uninfluenced by solid boundaries such as the ship hull or appendages or by a free surface, and without cavitation.

In order to simplify the geometry of the problem the flow field in the average, relative to the screw is assumed to form a helical system of constant pitch. This requires that the circumferential mean of the axial inflow velocity be independent of radius and that the circumferential mean of the tangential inflow velocity be zero at all radii. The latter is equivalent to requiring that there be no pre-rotation of the flow approaching the screw.* Assuming that the propeller rotates with uniform angular velocity in such an inflow field, a helical system of radially invariant pitch results.

Further, the propeller is assumed to be lightly loaded in the mean inflow so that race contraction and the change in the pitch of the helical vortex systems in the race may be neglected. The mean induced velocities are therefore considered negligibly small in comparison with the relative mean inflow as far as the geometry of the flow is concerned. Radial velocities are neglected. The flow is thus assumed to lie on cylindrical surfaces of constant radius.

* A linear radial variation of the circumferential mean of the tangential inflow velocity corresponds to a solid body rotation of the inflow to the screw and does not disturb the constant pitch helical nature of the field. The result is an effective change in propeller RPM but without change in frequency of encounter of inflow variations; a complication which the writer chooses to avoid at this stage of development.

From the point of view of an observer advancing but not rotating with the propeller, the inflow velocity is allowed to vary spacially, but not in time. Both axial and tangential variations in inflow velocity are considered, but again, radial variations are neglected. In fixed axes the inflow perturbation at a given radius is obviously periodic in the angular coordinate; the fundamental period being $\frac{2\pi}{\omega}$.

To the observer rotating with the propeller the spacial variation of the inflow velocity appears as a time variation as well. Assuming a uniform angular velocity, Ω , this time variation of an arbitrary inflow perturbation has a fundamental period equal to $2\pi/\Omega$. The inflow perturbations or variations from the mean can then be expressed in terms of a Fourier series in integral fractions of this fundamental time period or, equivalently, in integral multiples of the angular coordinate.

In keeping with linear theory the inflow perturbation velocities are assumed small in comparison with the mean relative inflow velocity. Assuming linearity, all the effects on the propeller caused by the inflow perturbations: lift, pressure, and particularly vorticity must also be expressible in Fourier series of the same fundamental period as the perturbation in space and time. Further, a particular harmonic component of the inflow perturbation will result in effects on the propeller of the same harmonic number and no other. Thus, as provided by linear theory, the analysis may proceed with the individual harmonic components of the flow field, and the total result may be finally arrived at by linear superposition.

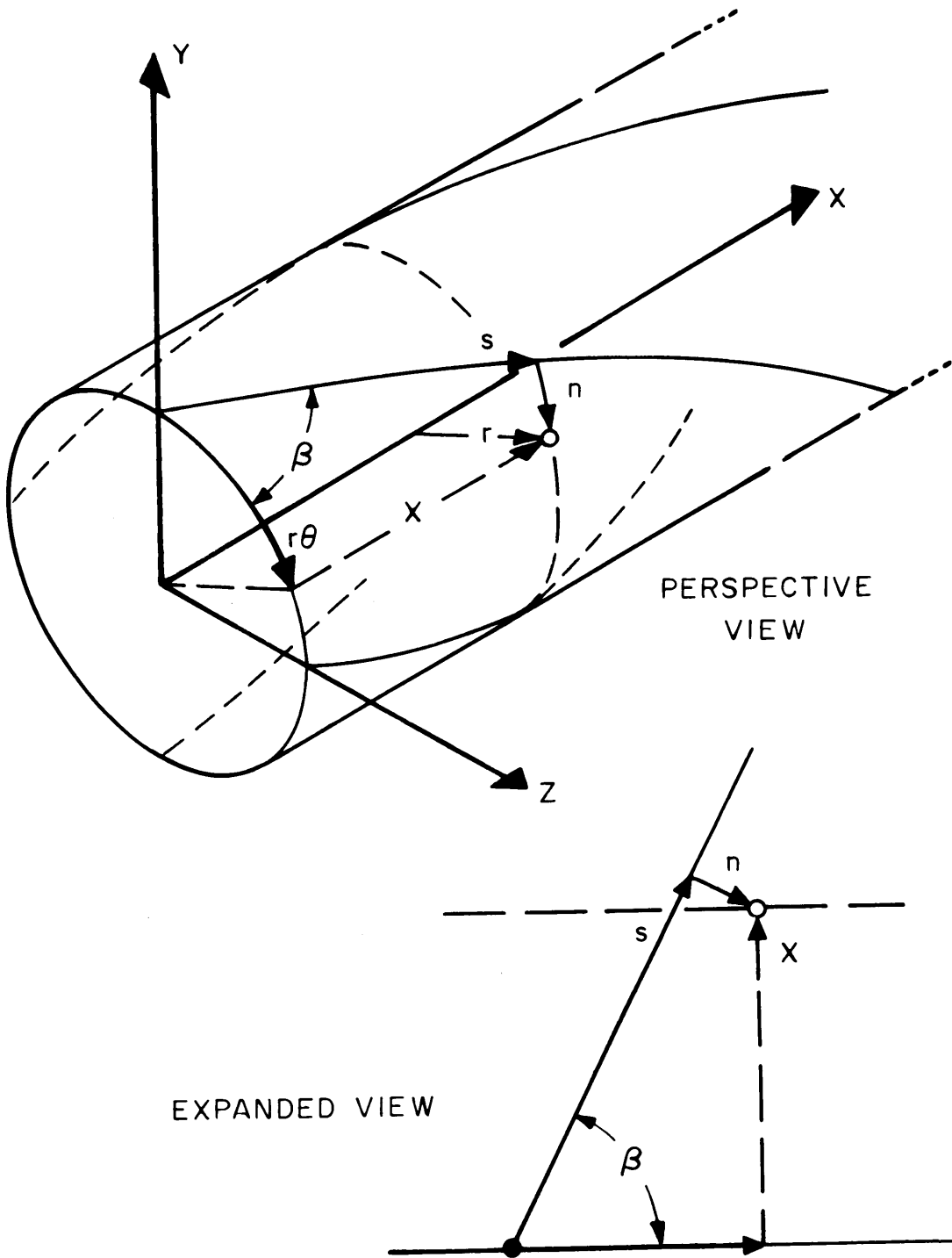


FIG. 2.1 COORDINATE SYSTEMS

The blades are assumed thin and describable by small offsets from the helical surfaces of the mean relative inflow. The bound vorticity of the blades and the shed vorticity in the race, both steady and unsteady, are assumed to lie upon these mean helical surfaces. The linearized boundary condition is satisfied upon the helical surfaces instead of upon the blade surfaces themselves.

The Kutta condition is assumed satisfied along the trailing edge in the unsteady flow.

The Kernel Functions

The coordinate systems employed in the following developments are illustrated in Fig. 2.1 and 2.2. We consider a right handed propeller of K equally spaced blades without rake. The usual rectangular (x,y,z) and cylindrical (x,r,θ) coordinate systems are retained; the x axis coinciding with the axis of the propeller. A radial reference line on the index blade coincides with the y axis. The angular coordinate, θ pertains to a particular helical surface and has the value of zero on the radial line which marks the intersection of that surface with the plane $x = 0$. If the angle between the reference lines of the k th and index blades be denoted δ_k , the total angular coordinate of a point on the helical surface of the k th blade is given by $\theta + \delta_k$.

With all coordinates made dimensionless on the basis of the propeller radius R , the rectangular coordinates of a point on the k th helical surface are given in terms of the cylindrical coordinates by:

$$\left. \begin{aligned} x &= r\theta \tan \beta \\ y &= r \cos (\theta + \delta_k) \\ z &= r \sin (\theta + \delta_k) \end{aligned} \right\} \quad (2.1)$$

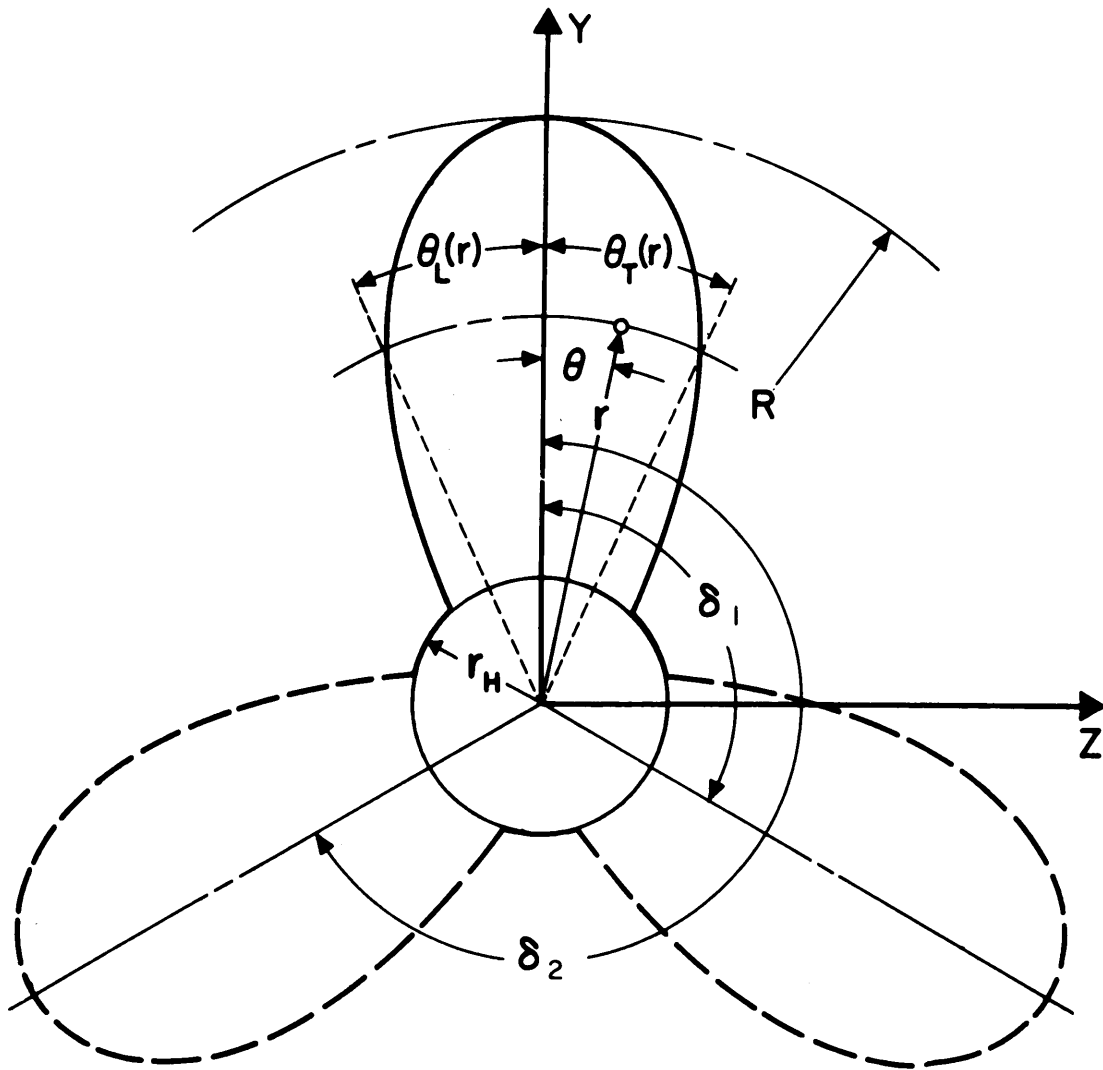


FIG. 2.2 COORDINATE SYSTEMS PROJECTED VIEW

The unit vectors of the orthogonal curvilinear coordinate system (s,r,n) along the helical surfaces are:*

$$\begin{aligned}\vec{u}_s &= \vec{i} \sin\beta - \vec{j} \sin(\theta + \delta_k) \cos\beta + \vec{k} \cos(\theta + \delta_k) \cos\beta \\ \vec{u}_r &= \vec{j} \cos(\theta + \delta_k) + \vec{k} \sin(\theta + \delta_k) \\ \vec{u}_m &= \vec{i} \cos\beta - \vec{j} \sin(\theta + \delta_k) \sin\beta + \vec{k} \cos(\theta + \delta_k) \sin\beta\end{aligned}\quad (2.2)$$

Several more geometrical relations are of use. In the expanded view, it is seen that for a point on the helix:

$$x = s \sin\beta \quad (2.3)$$

and for helices of constant pitch, $2\pi R$, the sine and cosine of the pitch angle at any radius are given by:

$$\begin{aligned}\sin\beta(r) &= \lambda / \sqrt{\lambda^2 + r^2} \\ \cos\beta(r) &= r / \sqrt{\lambda^2 + r^2}\end{aligned}\quad (2.4)$$

The vector distance between points (x,y,z) and (x_0,y_0,z_0) is given in rectangular coordinates by:

$$\vec{D} = \vec{i}(x - x_0) + \vec{j}(y - y_0) + \vec{k}(z - z_0) \quad (2.5)$$

and in cylindrical and helical coordinates by:

$$\begin{aligned}\vec{D} = \vec{i} &\left[s \sin\beta(r) - \sigma \sin\beta(\rho) \right] + \vec{j} \left[r \cos\theta - \rho \cos(\varphi + \delta_k) \right] \\ &+ \vec{k} \left[r \sin\theta - \rho \sin(\varphi + \delta_k) \right]\end{aligned}\quad (2.6)$$

where the point (x,y,z) lies on the helical surface of the index blade and the point (x_0,y_0,z_0) on that of the k th blade. The

*The sense of the normal coordinate is taken positive in the direction that a normal inflow velocity must have to produce a positive lift on the blade.

magnitude of this distance is given by:

$$|D| = \left[\lambda^2 (\varphi - \theta)^2 + r^2 + \rho^2 - 2r\rho \cos (\varphi + \delta_k - \theta) \right]^{\frac{1}{2}} \quad (2.7)$$

By the law of Biot-Savart, the vector velocity induced by a sheet of vorticity is given by the following integral over the area of the vortex sheet: (18)

$$\vec{w} = \frac{1}{4\pi} \iint \frac{\vec{\gamma} \times \vec{D}}{|D|^3} dA \quad (2.8)$$

The component of induced velocity which is normal to the helical surface at the point in question is:

$$w = \vec{w} \cdot \vec{u}_n \quad (2.9)$$

The Biot-Savart integrand for the normal induced velocity at a point (x, y, z) of the index blade due to elements of vorticity at the point (x_o, y_o, z_o) of the k th helical surface can now be written. Exclusive of the magnitude of the vorticity this is for the streamwise vorticity component:

$$\begin{aligned} & (\vec{u}_\sigma \times \vec{D}) \cdot \vec{u}_n / |D|^3 = \\ & \frac{\rho (r^2 - \lambda^2) \cos (\varphi + \delta_k - \theta) - r(\rho^2 - \lambda^2) - \rho \lambda^2 (\varphi - \theta) \sin (\varphi + \delta_k - \theta)}{\left[(\lambda^2 + r^2)(\lambda^2 + \rho^2) \right]^{\frac{1}{2}} \left[\lambda^2 (\varphi - \theta)^2 + r^2 + \rho^2 - 2r\rho \cos (\varphi + \delta_k - \theta) \right]^{3/2}} \end{aligned} \quad (2.10)$$

and for the radial vorticity component:

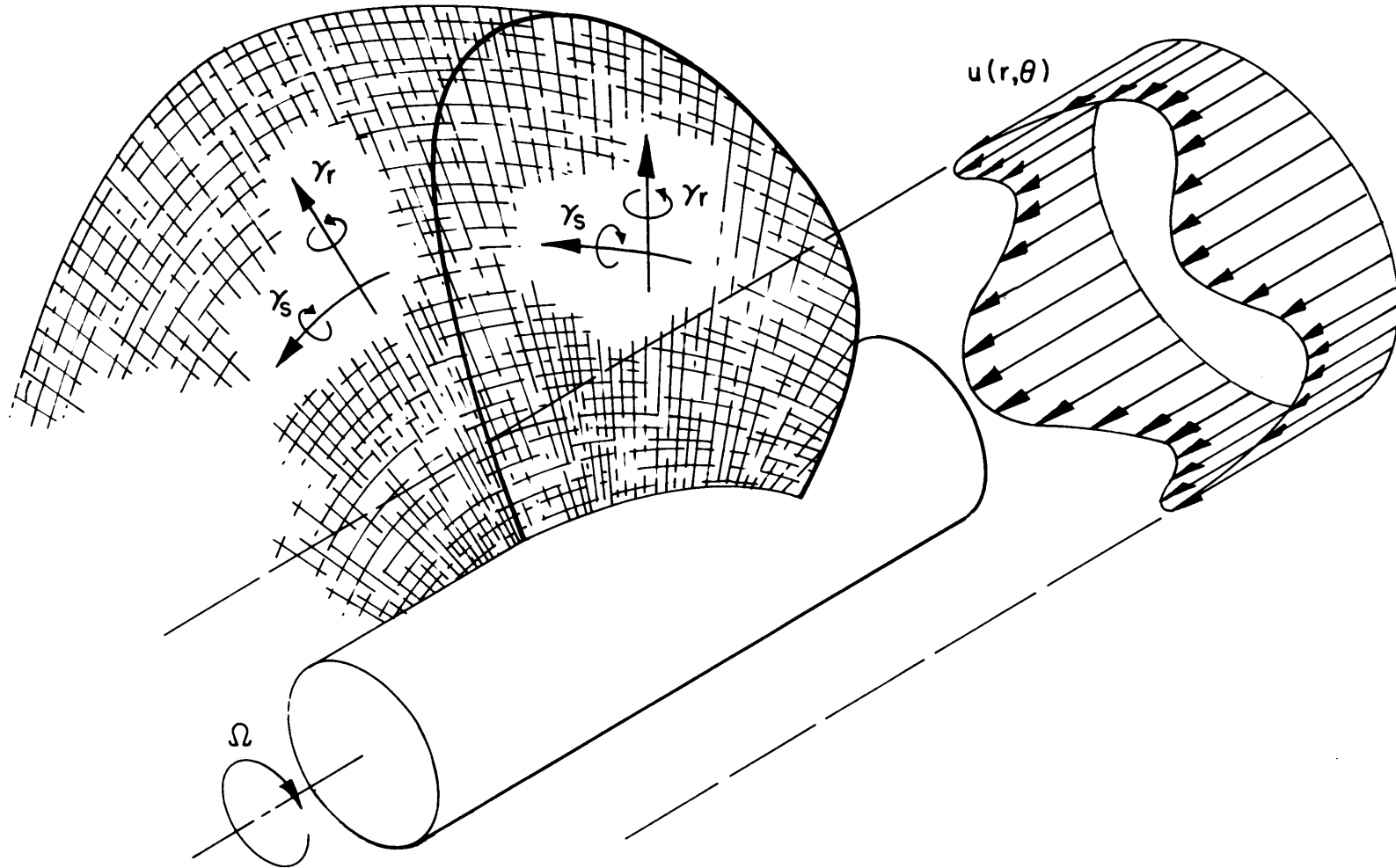


FIG. 23 VORTICITY COMPONENTS AND NON-UNIFORM INFLOW.

$$\begin{aligned}
& (\vec{u}_\rho \times \vec{D}) \cdot \vec{u}_n / |D|^3 = \\
& \frac{r^2 \sin(\varphi + \delta_k - \theta) + \lambda^2 (\varphi - \theta) \cos(\varphi + \delta_k - \theta)}{\left[\lambda^2 + r^2 \right]^{\frac{1}{2}} \left[\lambda^2 (\varphi - \theta)^2 + r^2 + \rho^2 - 2r\rho \cos(\varphi + \delta_k - \theta) \right]^{3/2}} \quad (2.11)
\end{aligned}$$

The functions (2.10) and (2.11) comprise the kernel functions of the integral equation for the bound vorticity. For brevity, these expressions may be denoted, respectively, by:

$$f_s(\sigma, \rho, s, r, k,) \text{ and } f_r(\sigma, \rho, s, r, k)$$

Vorticity Relations

The radial and streamwise vorticity components on the regions of the blades and shed into the race are illustrated in Fig. 2.3. On the blades, the strengths of both components as functions of position and time can be given in terms of vorticity at the corresponding point of the index blade, the harmonic number and the angle from the index blade of the blade in question, in the form:

$$\gamma(s, r, k, t) = \bar{\gamma}(s, r) e^{iN(\Omega t - \delta_k)} \quad (2.12)$$

By the principle of the continuity of vorticity, the streamwise vorticity component on the blade ~~may~~ ^{may} be related to the radial vorticity component; the latter being the unknown to be determined. (19)

$$\bar{\gamma}_s(s, r) = - \frac{\partial}{\partial r} \int_{s_L(r)}^s \bar{\gamma}_r(\sigma, r) d\sigma \quad (2.13)$$

The strength of the free vorticity shed by the blades into the race may be expressed as the product of a complex amplitude at the trailing edge and a sinusoidal time and distance variation along the helical surfaces in the streamwise direction. For both the radial and streamwise free vorticity components, this is of the form:

$$\gamma (s, r, k, t) = \bar{\gamma} (s_{\text{T}}(r)) e^{iN\Omega \left[t - R(s - s_{\text{T}})/U(r) \right]} e^{-iN\delta_k} \quad (2.14)$$

The complex strength of the radial shed vorticity at the trailing edge is determined by the requirement that the total circulation of the system of the bound plus shed vorticity remain zero at all times. (19)

$$\bar{\gamma}_r (s_{\text{T}}(r)) e^{iN\Omega t} = - \frac{1}{U(r)} \frac{\partial}{\partial t} \left[\bar{\Gamma}(r) e^{iN\Omega t} \right] = i \frac{N\Omega}{U} \bar{\Gamma} e^{iN\Omega t} \quad (2.15)$$

where the circulation at radius r is given by:

$$\bar{\Gamma}(r) = \int_{s_{\text{L}}(r)}^{s_{\text{T}}(r)} \bar{\gamma}_r (\sigma, r) d\sigma \quad (2.16)$$

Making use of the relations:

$$\begin{aligned} \Omega s / U(r) &= \theta \\ \Omega / U(r) &= 1/R \sqrt{\lambda^2 + r^2} \end{aligned} \quad (2.17)$$

the expression for the radial shed vorticity component becomes:

$$\gamma_r(s, r, k, t) = -i \frac{N\bar{\Gamma}(r)}{R\sqrt{\lambda^2 + r^2}} e^{iN\left[(\Omega t - \delta_k) - (\theta - \theta_T(r))\right]} \quad (2.18)$$

The complex strength of the streamwise shed vorticity component at the trailing edge is determined by (2.13) when the upper limit of integration is $s_T(r)$; using (2.16)*:

$$\bar{\gamma}_s(s_T(r)) = -\frac{1}{R} \frac{\partial}{\partial r} \bar{\Gamma}(r) \quad (2.19)$$

leading to the final expression:

$$\gamma_s(s, r, k, t) = -\frac{1}{R} \frac{\partial}{\partial r} \bar{\Gamma}(r) e^{iN\left[(\Omega t - \delta_k) - (\theta - \theta_T(r))\right]} \quad (2.20)$$

The Boundary Condition

The component of the induced velocity normal to the helical surface of the index blade at the point (s, r) is also a harmonic function of time:

$$w(s, r, t) = \bar{w}(s, r) e^{iN\Omega t} \quad (2.21)$$

In the above expressions the induced velocity, the vorticity and the circulation are dimensional quantities whereas the coordinates are dimensionless. It is convenient to make the induced velocity dimensionless on the basis of the mean streamwise inflow velocity relative to the blade at radius r , namely:

$$U(r) = R\Omega \sqrt{\lambda^2 + r^2} \quad (2.22)$$

* γ and Γ are not dimensionless as is r , hence R is introduced.

and the vorticity and circulation on the basis of the tangential propeller tip velocity. Denoting the dimensional quantities by primes, the dimensionless quantities are then:

$$\begin{aligned}\bar{w}(s, r) &= \bar{w}'(s, r)/U(r) \\ \bar{\gamma} &= \bar{\gamma}'/R\Omega \\ \bar{\Gamma} &= \bar{\Gamma}'/R^2\Omega\end{aligned}\tag{2.23}$$

Combining (2.9), (2.10), (2.11), (2.18) and (2.20), the complex amplitude of the dimensionless normal induced velocity is:

$$\begin{aligned}\bar{w}(s, r) \cdot 4\pi(\lambda^2 + r^2) &= \sum_{k=0}^{K-1} \left\{ \int_{\text{blades}} [\bar{\gamma}_r(\sigma, \rho) \cdot f_r(\sigma, \rho, s, r, k) \right. \\ &+ \bar{\gamma}_s(\sigma, \rho) \cdot \left. \frac{f_s(\sigma, \rho, s, r, k)}{\sqrt{\lambda^2 + \rho^2}} \right] e^{-iN\delta_k} d\sigma d\rho \\ &- \iint_{\text{race}} [iN\bar{\Gamma}(\rho) \cdot f_r(\sigma, \rho, s, r, k) \\ &+ \left. \frac{\partial}{\partial \rho} (\bar{\Gamma}(\rho)) \cdot f_s(\sigma, \rho, s, r, k) \right] \frac{e^{-iN[\varphi - \varphi_T(\rho) + \delta_k]}}{\sqrt{\lambda^2 + \rho^2}} d\sigma d\rho \left. \right\}\end{aligned}\tag{2.24}$$

The Cauchy principle^{al} value of the integrals need be taken only when integrating over the index blade, when $k = 0$.

If the complex amplitude of the normal component at the point (s, r) of the N th harmonic of the inflow velocity perturbation is denoted $\bar{w}'_N(s, r)$, the boundary condition to be satisfied at that point of the index blade on its helical surface is written:

$$\bar{w}'(s, r) + \bar{w}'_N(s, r) = U(r) \frac{\partial}{\partial s} h(s, r) \quad (2.25)$$

Where the velocities are relative to the blade and h denotes the offset of the blade section mean surface as measured from the helical surface in the normal direction. Dividing by $U(r)$ and solving for the induced velocity, there results:

$$\bar{w}(s, r) = \frac{\partial}{\partial s} h(s, r) - \bar{w}'_N(s, r) \quad (2.26)$$

Recalling equations (2.13) and (2.16) which relate the streamwise vorticity component and the circulation, respectively, to the radial vorticity, substitution of the integral relation for the induced velocity (2.24) into the expression for the boundary condition (2.26) results in the singular integral equation which must be solved for the unknown bound vorticity $\bar{\gamma}_r$. No attempt is made to solve this equation as it stands. In the following chapters a simplification is made wherein the blades of the propeller are reduced to line vortices as an approximation to the above and a method of solution outlined.

CHAPTER III

THE VORTEX LINE MODEL

Reduction to Vortex Lines

In order to simplify the governing equation (2.24) and to affect a useful engineering approximation to the solution the analysis proceeds on the basis of applying a correction to the simple two dimensional unsteady strip theory analysis to account for three dimensional effects. The dimensionless normal velocity of (2.24) is written in the form:

$$\bar{w}(s,r) = \bar{w}_{2D} + (\bar{w}_{3D} - \bar{w}_{2D}) \quad (3.1)$$

The quantity in parenthesis is hereafter denoted the "downwash difference". This is the correction to be determined.

The first term on the right above, the two dimensional induced velocity, is that which would obtain if the index propeller blade were of constant chord, of infinite span, plane instead of helical, and subject to inflow perturbations everywhere that are the same as along the chord line containing the point (s,r) , in the absence of other blades. This is presumed known from the well developed unsteady two dimensional thin airfoil theory (20), (21), (22).

The downwash difference is approximated in the following manner:

The difference between the normal induced velocity of the actual radial bound vorticity and that of the two dimensional bound vorticity over the index blade is neglected. The induced velocity

of the streamwise vorticity component over the index blade is either neglected or considered to be lumped in with the shed streamwise vorticity. Making these approximations, the downwash difference due to the vorticity on the index blade disappears.

The induced velocity of the bound vorticity of the other blades is approximated by concentrating that radial vorticity into a single radial vortex line on each blade with the same radial circulation distribution. For purposes of an easily visualized model this is done on the index blade also.

The shed vorticity systems in the race, both radial and streamwise components are then taken to be generated by the time varying circulation on the radial vortex lines and to be shed from these lines instead of from the trailing edges. The radial vortex lines may be taken to coincide with the reference line of the index blade and the corresponding lines of the other blades as illustrated in Fig. 3.1.

In order to further simplify the geometry of the problem a nominal value of the downwash difference is found along a single radial line on the index blade instead of at all points of the blade. This line is taken the same as the vortex line. Doing this does not violate the previous neglect of the downwash difference due to the bound vorticity of the index blade and the subsequent concentration of that vorticity in a vortex line because a straight vortex line induces no velocity upon itself.

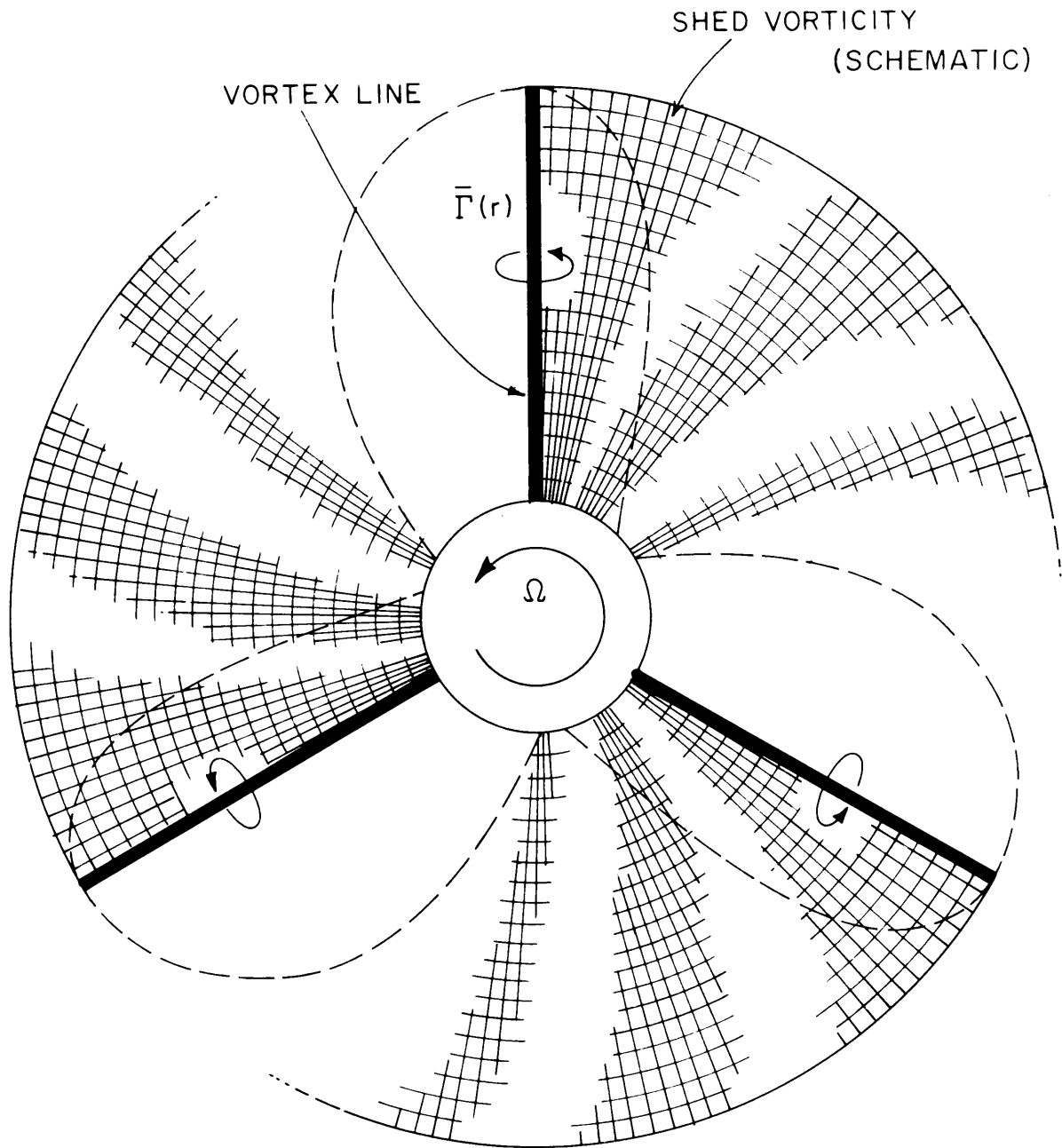


FIG. 3.1 VORTEX LINE MODEL FOR DOWNWASH DIFFERENCE

The kernel functions may now be simplified as follows:

On the radial vortex lines, where the downwash difference is found

$$\theta = s = 0 \quad (3.2)$$

and on the blades where the bound vorticity is concentrated into radial vortex lines:

$$f_r(\sigma, \rho, s, r, k) \rightarrow f_r(\rho, r, k) = \frac{r^2 \sin \delta_k}{(r^2 + \rho^2 - 2r\rho \cos \delta_k)^{3/2}} \quad (3.3)$$

and all the streamwise vorticity contribution is neglected.

In the propeller race:

$$f_r(\sigma, \rho, s, r, k) \rightarrow f_r(\sigma, \rho, r, k) = \frac{r^2 \sin(\varphi + \delta_k) + \lambda^2 \varphi \cos(\varphi + \delta_k)}{[\lambda^2 \varphi^2 + r^2 + \rho^2 - 2r\rho \cos(\varphi + \delta_k)]^{3/2}} \quad (3.4)$$

and:

$$f_s(\sigma, \rho, s, r, k) \rightarrow f_s(\sigma, \rho, r, k) = \frac{\rho(r^2 - \lambda^2) \cos(\varphi + \delta_k) - r(\rho^2 - \lambda^2) - \rho \lambda^2 \varphi \sin(\varphi + \delta_k)}{[\lambda^2 \varphi^2 + r^2 + \rho^2 - 2r\rho \cos(\varphi + \delta_k)]^{3/2}} \quad (3.5)$$

Now it is more convenient to work in the angular coordinate than the streamwise coordinate so use is made of the relation:

$$d\sigma = \sqrt{\lambda^2 + \rho^2} d\varphi \quad (3.6)$$

If further we denote:

$$\left. \begin{aligned} \rho/r &= \eta \\ \lambda/r &= \tan \beta(r) = p \end{aligned} \right\} \quad (3.7)$$

the integral expression (2.24) for the induced velocity becomes, for the approximate downwash difference at the vortex line of the index blade:

$$\begin{aligned} \bar{w}_{DD}(r) = & \frac{1}{4\pi r^2(p^2+1)} \sum_{k=0}^{K-1} \left\{ \sin \delta_k e^{-iN\delta_k} \int_{\eta_H}^{\eta_T} \frac{\bar{\Gamma}(\eta) d\eta}{(\eta^2 - 2\eta \cos \delta_k + 1)^{3/2}} \right. \\ & -iN \int_0^{\infty} \int_{\eta_H}^{\eta_T} \bar{\Gamma}(\eta) \frac{\sin(\varphi+\delta_k) + p^2 \varphi \cos(\varphi+\delta_k)}{[\eta^2 - 2\eta \cos(\varphi+\delta_k) + p^2 \varphi^2 + 1]^{3/2}} e^{-iN(\varphi+\delta_k)} d\eta d\varphi \\ & \int_0^{\infty} \int_{\eta_H}^{\eta_T} \frac{\partial}{\partial \eta} (\bar{\Gamma}(\eta)) \frac{\eta(1-p^2) \cos(\varphi+\delta_k) - \eta^2 + p^2 - \eta p^2 \varphi \sin(\varphi+\delta_k)}{[\eta^2 - 2\eta \cos(\varphi+\delta_k) + p^2 \varphi^2 + 1]^{3/2}} \\ & \left. \cdot e^{-iN(\varphi+\delta_k)} d\eta d\varphi \right\} - \bar{w}_{2D*} \quad (3.8) \end{aligned}$$

where the last term denotes the velocity induced by the shed vorticity in two-dimensional flow, having not yet been evaluated and subtracted from the expression for the downwash difference.

The first term above represents the contribution to the induced velocity at the index vortex line due to the circulation of the vortex lines representing the other blades. The second term represents the contribution of the radial vorticity component in the race which is being shed by all of the blades due to their time varying circulation. The third term represents the contribution of the streamwise vorticity component on the trailing helices which is being shed by all of the blades due to their radially varying circulation. The vortex line approximation for the downwash difference is illustrated in Fig. 3.1.

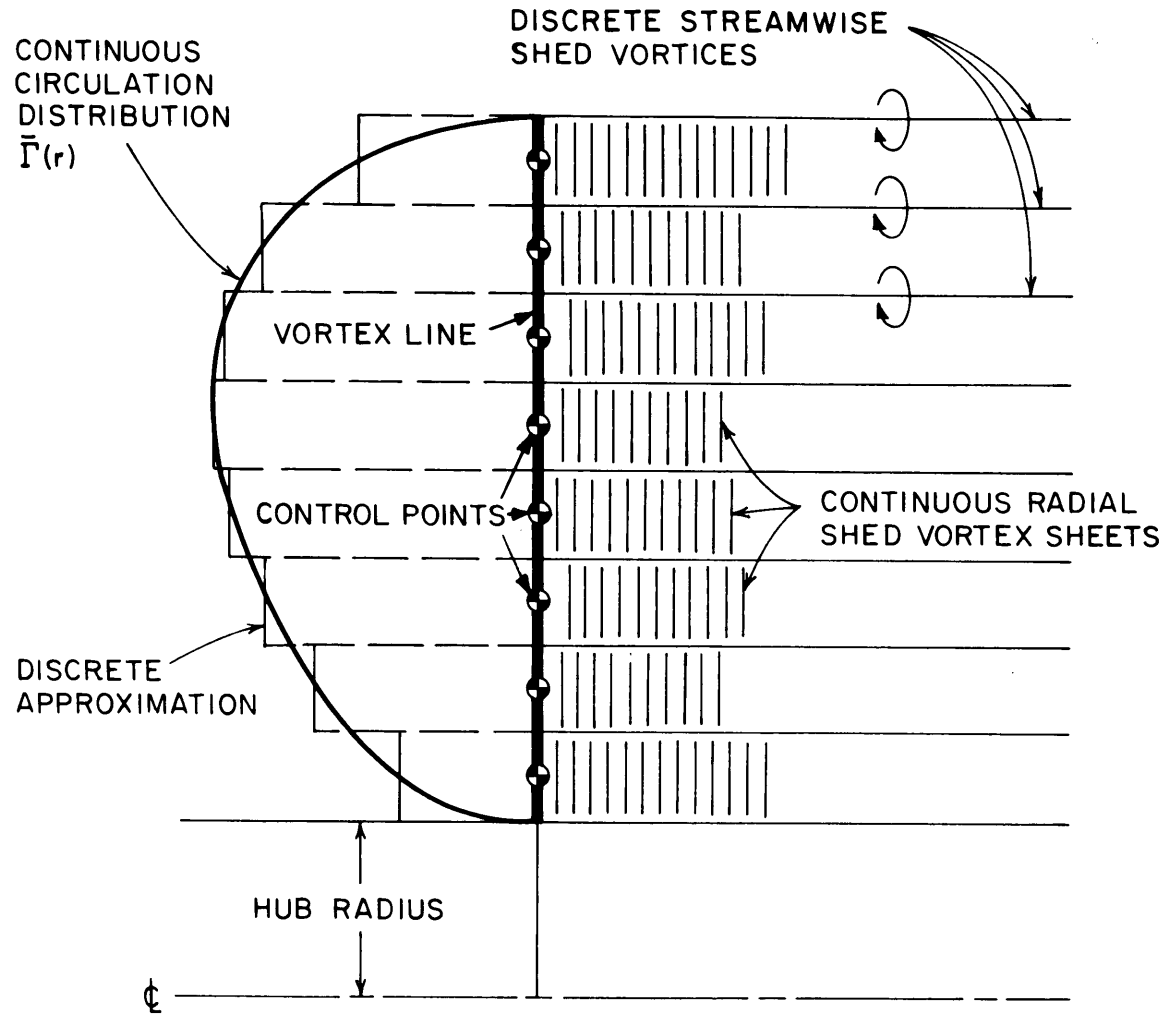


FIG. 3.2 DISCRETE APPROXIMATION OF CONTINUOUS RADIAL CIRCULATION DISTRIBUTION (SCHEMATIC)

Discretion

It may be noted that in the first and second η integrals of (3.8) the only function of η in the numerators of the integrands is the circulation $\bar{\Gamma}(\eta)$. For computational purposes the continuous circulation distribution on the radial vortex lines is approximated by a set of radial segments of constant circulation as illustrated in Fig. 3.2. With the circulation no longer a function of radius, the η integrations in the first two terms may be easily carried out over each segment. With $\bar{\Gamma}(\eta)$ a constant in the interval (η_1, η_2) the first integral becomes:

$$\int_{\eta_1}^{\eta_2} \frac{\bar{\Gamma}(\eta) d\eta}{(\eta^2 - 2\eta \cos \delta_k + 1)^{3/2}} = \frac{\bar{\Gamma}(\eta)}{\sin^2 \delta_k} \left[\frac{\eta - \cos \delta_k}{(\eta^2 - 2\eta \cos \delta_k + 1)^{1/2}} \right]_{\eta_1}^{\eta_2} \quad (3.9)$$

The cases where $\cos^2 \delta_k = 1$ are excluded; that is the index vortex line and one removed by 180° , but this is no restriction since neither can induce a velocity along the index line.

Again with $\bar{\Gamma}(\eta)$ a constant in (η_1, η_2) the second integral becomes:

$$\int_{\eta_1}^{\eta_2} \frac{\bar{\Gamma}(\eta) d\eta}{[\eta^2 - 2\eta \cos(\varphi + \delta_k) + p^2 \varphi^2 + 1]^{3/2}} = \frac{\bar{\Gamma}(\eta)}{\sin^2(\varphi + \delta_k) + p^2 \varphi^2} \cdot \left[\frac{\eta - \cos(\varphi + \delta_k)}{\sqrt{\eta^2 - 2\eta \cos(\varphi + \delta_k) + p^2 \varphi^2 + 1}} \right]_{\eta_1}^{\eta_2} \quad (3.10)$$

In the discrete model the streamwise directed shed vorticity becomes a set of discrete trailing vortices emanating from the ends of the segments of constant circulation on the vortex lines. The expression for the contribution to the downwash difference due to these vortices from the segment (η_1, η_2) on the kth vortex line is:

$$+\bar{\Gamma}(\eta) \int_0^{\infty} \left[\frac{\eta(1-p^2)\cos(\varphi+\delta_k) - \eta^2+p^2 - \eta p^2 \varphi \sin(\varphi+\delta_k)}{(\eta^2-2\eta \cos(\varphi+\delta_k) + p^2 \varphi^2 + 1)^{3/2}} \right]_{\eta_1}^{\eta_2} e^{-iN(\varphi+\delta_k)} d\varphi \quad (3.11)$$

The discrete approximation to the continuous radial circulation distribution on the vortex lines leads to the useful concept of vorticity panels. The vorticity system of the vortex line model may be considered to be the sum of the elementary vorticity systems which comprise these panels. Each panel consists of a segment of radial vortex line of constant strength but varying with time in a sinusoidal manner, which sheds a band of radial vorticity of the same radial width, bounded by a pair of trailing vortices shed from the ends of the segment. The radial sheet and the bounding trailers vary in strength sinusoidally according to the frequency of the circulation variation of the vortex line segment, and these strengths are as required for the conservation of vorticity. Each panel is then a self-contained system containing all the effects of the vortex line segment which is its origin. In particular, the velocity induced at the index vortex line by the set of panels emanating from corresponding segments of k blades is expressible in terms of (3.9), (3.10) and (3.11).

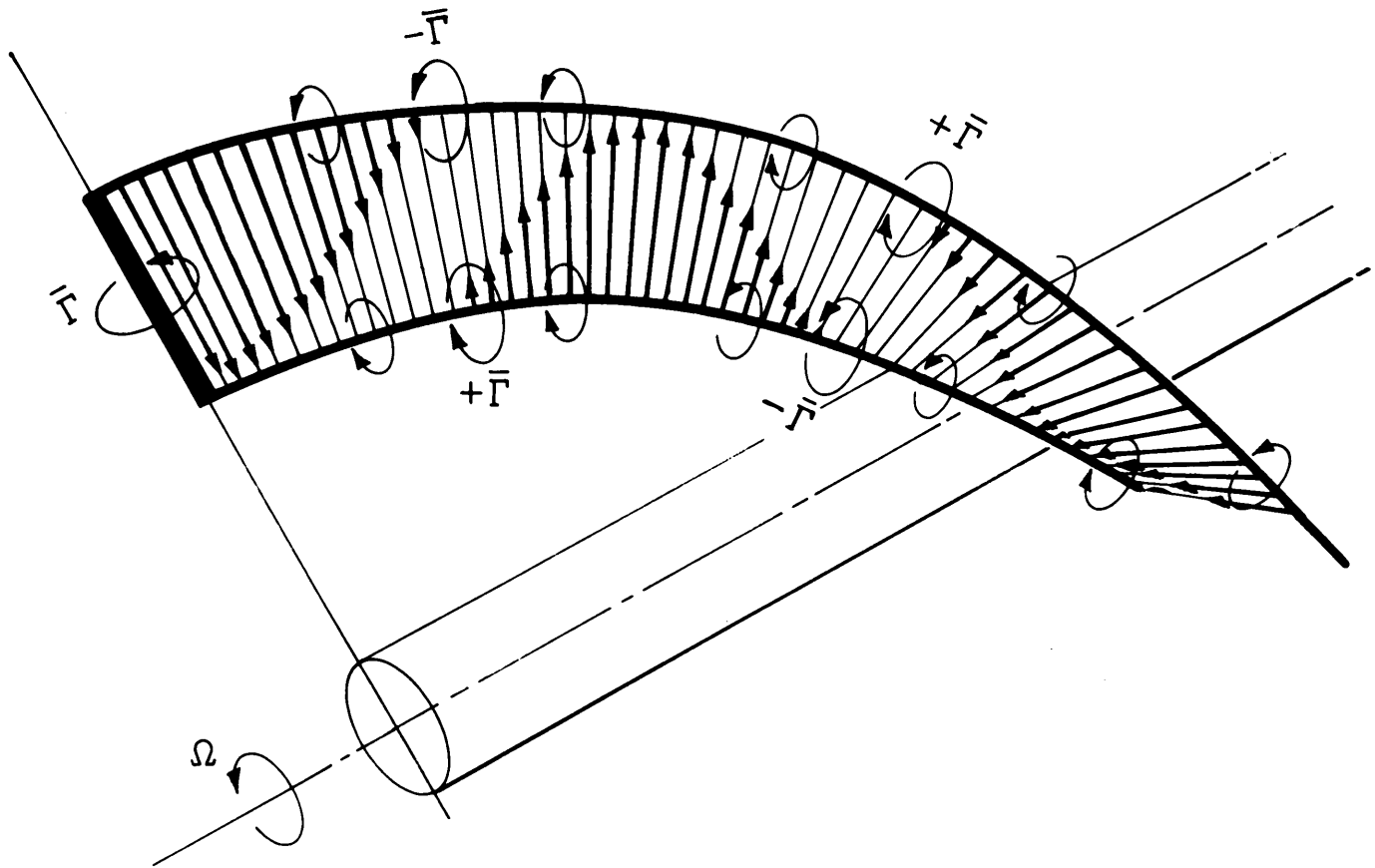


FIG. 33 VORTICITY PANEL (SCHEMATIC)

The vorticity of a panel trails back along the helical surface swept out by a vortex line as shown in Fig. 3.3. The vorticity panel can be considered the logical extension to unsteady periodic flow of the steady flow "horseshoe" vortex system. It will be seen that when the harmonic number is zero, the vorticity panel reduces to the steady helical flow horseshoe vortex system.

The Downwash Difference

Developing further the downwash difference on the basis of vorticity panels the integrand (3.10) is seen to be singular in the φ integration at $\varphi = 0$ and $\eta = 1$ with $\delta_k = 0$. In order to avoid this singular behavior, it will be convenient to subtract the integrand of the two dimensional shed vorticity at this point. It is presumed that the two dimensional shed vorticity can be considered shed from the vortex line rather than the trailing edge as with the three dimensional shed vortex systems.

Using the present notation, the normal induced velocity at the vortex line due to the shed vorticity in two dimensional flow is:

$$w'_{2D*}(r, \sigma, t) = \frac{1}{2\pi} \int_0^{\infty} \frac{\gamma'(r, \sigma, t)}{\sigma} d\sigma \quad (3.12)$$

Referring again to expressions (2.14), (2.15) and (2.17) this may be written:

$$\bar{w}'_{2D*}(r) = - \frac{iN\bar{\Gamma}(r)}{2\pi R \sqrt{\lambda^2 + r^2}} \int_0^{\infty} \frac{e^{-iN\sigma\varphi}}{\sigma} d\sigma \quad (3.13)$$

Again making $\bar{w}(r)$ dimensionless on the basis of $U(r)$ and $\bar{\Gamma}(r)$ on the basis of $R^2\Omega$; and noting that $d\sigma/\sigma = d\varphi/\varphi$, there results finally at $\eta = 1$:

$$\bar{w}_{2D^*}(r) = - \frac{iN}{2\pi r^2(p^2+1)} \bar{\Gamma}(r) \int_0^\infty \frac{e^{-iN\varphi}}{\varphi} d\varphi \quad (3.14)$$

Subtracting this integrand we have then for the downwash difference contributed by the panel $\eta_1 < 1 < \eta_2$ with $\delta_k = 0$:

$$-iN\bar{\Gamma}(\eta) \int_0^\infty \left\{ \frac{\sin \varphi + p^2 \varphi \cos \varphi}{\sin^2 \varphi + p^2 \varphi^2} \left[\frac{\eta - \cos \varphi}{(\eta^2 - 2\eta \cos \varphi + p^2 \varphi^2 + 1)^{1/2}} \right]_{\eta_1}^{\eta_2} - \frac{2}{\varphi} \right\} e^{-iN\varphi} d\varphi \quad (3.15)$$

It can be shown that the expression in the $\left\{ \right\}$ tends to zero as $\varphi \rightarrow 0$ (see Appendix B) since the singularities at $\varphi = 0$ in both the three and two dimensional cases are of the same order.

It may be noted from expressions (3.9), (3.11) and (3.15) that the downwash difference induced by a vorticity panel is linear in the complex circulation $\bar{\Gamma}(\eta)$ of the panel vortex segment. Therefore define a new dimensionless complex velocity $\bar{w}(r, \rho)$ which is the downwash difference at radius r of the index reference line due to the vorticity panels centered on radius ρ whose vortex segments have unit complex circulation.

$$\bar{w}(r, \rho) = \bar{w}_{DD}(r) / \bar{\Gamma}(\rho) \quad (3.16)$$

The final expression for this downwash difference is

then:

$$\begin{aligned}
 \bar{w}(r, \rho) \cdot 4\pi r^2 (p^2 + 1) &= \sum_{k=1}^{K-1} \frac{e^{-iN\delta_k}}{\sin \delta_k} \left[\frac{\eta - \cos \delta_k}{\sqrt{\eta^2 - 2\eta \cos \delta_k + 1}} \right]_{\eta_1}^{\eta_2} \\
 &- iN \sum_{k=0}^{K-1} \int_0^{\infty} \frac{\sin(\varphi + \delta_k) + p^2 \varphi \cos(\varphi + \delta_k)}{\sin^2(\varphi + \delta_k) + p^2 \varphi^2} \left[\frac{\eta - \cos(\varphi + \delta_k)}{\sqrt{\eta^2 - 2\eta \cos(\varphi + \delta_k) + p^2 \varphi^2 + 1}} \right]_{\eta_1}^{\eta_2} e^{-iN(\varphi + \delta_k)} d\varphi \\
 &- iN \int_0^{\infty} \left\{ \frac{\sin \varphi + p^2 \varphi \cos \varphi}{\sin^2 \varphi + p^2 \varphi^2} \left[\frac{\eta - \cos \varphi}{\sqrt{\eta^2 - 2\eta \cos \varphi + p^2 \varphi^2 + 1}} \right]_{\eta_1}^{\eta_2} - \frac{2}{\varphi} \right\} e^{-iN\varphi} d\varphi \\
 &+ \sum_{k=0}^{K-1} \int_0^{\infty} \left[\frac{\eta(1-p^2)\cos(\varphi + \delta_k) + p^2 - \eta^2 - \eta p^2 \varphi \sin(\varphi + \delta_k)}{(\eta^2 - 2\eta \cos(\varphi + \delta_k) + p^2 \varphi^2 + 1)^{3/2}} \right]_{\eta_1}^{\eta_2} e^{-iN(\varphi + \delta_k)} d\varphi
 \end{aligned}
 \tag{3.17}$$

In the first term we exclude from the sum values for $k/K = 0, 1/2$ since these contribute nothing. Also, if the harmonic number N is equal to or an integral multiple of the number of blades the sum is zero as can be seen from the symmetrical arrangement of the uniformly spaced blades.

In the second term we exclude the case of $k = 0$ when $\eta_1 < 1 < \eta_2$ and use the third term instead. There are no restrictions on the last term.

It may be noted that when $N = 0$ the circumferential variations vanish so that the problem is reduced to the steady case. All terms but the last dropout, and this becomes the steady flow lifting line model of the propeller with a system of discrete trailing vortices of constant strength in the streamwise direction.

(23) (24)

Discussion of the Model

In approximating the downwash difference, the neglect of the difference between the effects of the two and three dimensional bound vorticity will be most in error where the bound vorticity distribution or the shape of the blade is changing rapidly with radius. Hence, the most error may be expected from this source on low aspect ratio blades and in the tip region of high aspect ratio blades. The same may be said for the neglect of the streamwise vorticity component on the blade.

The streamwise shed vortices are, of course, absent in two dimensional flow so that they add directly to the downwash difference. These spring from the trailing edge with the final strength of the streamwise vorticity on the blade and are thus probably stronger than the chordwise average of the latter. Computing the velocity induced by the trailers at the vortex line from which they are shed is equivalent to finding the velocity they induce at the trailing edge, if it were straight, of the real blade. The control point is thus closer to the shed vortices in the vortex line model than the average chordwise position is in

the real case. The downwash difference due to the trailers that is computed from this model is thus probably somewhat overestimated, but this may be made up to some extent by the neglect of the streamwise vorticity on the blade.

The radial component of shed vorticity does not enter directly into the determination of the downwash difference so the effects of the vortex line model are difficult to see. The radial vorticity would induce a very strong velocity at the trailing edge but this is all but annihilated by the subtraction of the velocity induced by the two dimensional shed vorticity, since both have the same behavior near the trailing edge. Transfer of this system to the vortex line from the trailing edge thus probably causes less error than for the trailers because these effects are due to more far field effects.

The approximation to the downwash difference carried out here is analogous to that of the Reissner "lifting strip" analysis for the case of the oscillating plane wing. (25) Reissner simplifies the integral expression for the induced velocity in this manner in order to achieve a form which can be inverted by standard means, thereby obtaining an integral expression for the bound vorticity in terms of the known downwash of the wing oscillation. This is not attempted here because of the much more complex kernel functions involved due to the helical field and the desire to keep a physical picture of the proceedings.

The presented vortex line model is, of course, different from the Reissner model in that it attempts to describe the flow field of a multi-blade propeller rather than a plane wing. The helical nature of the flow, at least for the geometry of the multiple sheets of shed vorticity, is accurately taken account of. The vortex line representation of blades other than the index blade is expected to be adequate because of the fact that their influence on the index blade is rather small due to their distance, except near the hub. Generally speaking, low aspect ratio blades are found on propellers with few blades where the interblade distances are large. For many bladed propellers, where the interblade spacing is small, the aspect ratio of the blades tends to be higher, thus the vortex line model tends to give a more accurate representation when it counts.

Experimental results of Laidlaw (26) and others show that the Reissner theory, although a high aspect ratio approximation, predicts the lift magnitude and phase of oscillating wings of rectangular planform with aspect ratios down to two without serious error. Although the inflow perturbation in the present case is not of the form produced by a rigid body oscillation and the reduced frequencies encountered may be considerably larger than those obtained in the experiments above, it is reasonable to expect similar accuracy.*

*As the reduced frequency approaches zero, the Reissner analysis approaches the lifting line, while it approaches strip theory for high reduced frequency. The form of the perturbation does not affect this behavior.

The segmentation of the radial vortex lines and the resultant replacement of the streamwise shed vorticity sheet by a set of discrete vortices has been shown to be an accurate approximation to the continuous distribution for the steady flow propeller case by Kerwin (24). The induced velocities must be evaluated only at the midpoints of the radial vortex segments in order to maintain the validity of this model. The discrete model may be expected to remain accurate in unsteady flow so long as the panel width is kept small with respect to the wave length of the disturbance.

CHAPTER IV

METHOD OF SOLUTION

Simultaneous Equations for the Circulation

We wish to determine the magnitude and radial distribution of the complex circulation and lift on the index blade. On the other blades these quantities are obtained by applying the appropriate phase shifts to the results for the index blade. It is first necessary to solve for the circulation; thus determining the strengths of the various vorticity systems and the induced velocities.

The circulation distribution on the index blade is expressed in the form of a series of functions in the radial direction.

$$\bar{\Gamma}(r) = \sum_n \bar{A}_n f_n(r) \tag{4.1}$$

The series will be taken to have a finite number of terms and the complex coefficients \bar{A}_n are to be determined.

A convenient set of functions is given by part of the Birnbaum or Glauert series commonly utilized in thin airfoil and lifting line theory: (27) (28)

$$f_n(r) = \sin n \psi \tag{4.2}$$

where the radial variable ψ is determined by the transformation:

$$\cos \psi = \frac{1 + r_H - 2r}{1 - r_H} \tag{4.3}$$

This series insures that the circulation goes to zero at the blade tip as desired, but it also does so at the radius of the hub, r_H . We thus have free ends at the inner radii of the blades a situation which is not representative of the actual case but which is ignored due to the relatively weak influence of the inner radii on the final result.

The boundary condition on the blade, determining the induced velocity, as expressed in equation (2.26) may be simplified by neglecting the streamwise derivative of the blade surface offsets in comparison with the inflow and induced velocities. This is equivalent to replacing the blade sections by flat plate foils in two dimensional flow. Consideration of the effect of camber and angle of attack on unsteady lift and circulation are refinements that need not be considered at this stage of development. The induced velocity and the inflow are presumed evaluated at points of the reference line rather than at a general point in accord with the simplifications of the vortex line model. The induced velocity is then written according to (2.26) and (3.1):

$$\bar{w} = \bar{w}_{2D} + \bar{w}_{DD} = -\bar{w}_N \quad (4.4)$$

or:

$$\bar{w}_{2D} = -(\bar{w}_N + \bar{w}_{DD}) \quad (4.5)$$

For a flat plate foil, the induced velocity must equal the negative of the normal inflow velocity perturbation, in two dimensions as well as three. This inflow, as experienced by a

section considered two dimensional, at the radius in question is given then by $+(\bar{w}_N + \bar{w}_{DD})$. The inflow is therefore considered corrected by the downwash difference if the section is considered two dimensional.

If we denote by \bar{W}_{ij} the downwash difference of (3.17) due to the vorticity panels of unit circulation on the i th vortex segments, centered on radius r , as evaluated at radius r in the center of the j th segment of the index vortex line, then the total downwash difference at that point is given by:

$$\bar{w}_{DDj} = \sum_i \bar{\Gamma}_i \bar{W}_{ij} \quad (4.6)$$

The \bar{W}_{ij} thus form a set of "influence coefficients" relating the downwash difference distribution to the circulation distribution.

Writing the circulation in the form of (4.1) for the i th and j th panels, we have:

$$\bar{\Gamma}_i = \sum_n \bar{A}_n f_{ni} \quad (4.7)$$

$$\bar{\Gamma}_j = \sum_n \bar{A}_n f_{nj}$$

and the circulation of the j th panel can also be written:

$$\bar{\Gamma}_j = \bar{w}_{2Dj} \bar{G}_j \quad (4.8)$$

where \bar{G}_j is the complex transfer function between circulation and normal velocity from two-dimensional unsteady airfoil theory. The apparent normal inflow velocity to the section at the j th panel, considered two dimensional is given, as mentioned, by the sum of the inflow and downwash difference at that position. Using (4.6):

$$\bar{w}_{2Dj} = \bar{w}_{Nj} + \sum_i \bar{\Gamma}_i \bar{W}_{ij} \quad (4.9)$$

Equating the two expressions (4.8) and (4.7), there results:

$$\sum_n \bar{A}_n f_{nj} = (\bar{w}_{Nj} + \sum_i \sum_n \bar{A}_n f_{ni} \bar{W}_{ij}) \bar{G}_j \quad (4.10)$$

which leads to the following set of simultaneous linear algebraic equations to be solved for the unknown set of complex circulation series coefficients \bar{A}_n :

$$\sum_n \bar{A}_n \left[f_{nj} / \bar{G}_j - \sum_i f_{ni} \bar{W}_{ij} \right] = \bar{w}_{Nj} \quad (4.11)$$

The integral equation of Chapter II is thus approximated by the set of simultaneous equations above and inverting the integral equation is equivalent to inverting the coefficient matrix of the approximating set. The expression in [] is that matrix of complex coefficients. It may be noted that if the downwash difference matrix \bar{W}_{ij} is made zero, there results the purely two dimensional strip theory solution. The term containing \bar{W}_{ij} is thus a correction

to the two-dimensional strip theory analysis to take account of the three-dimensional nature of the flow field and the influence of the other blades, as was intended.

By choosing the number of terms in the circulation series equal to the number of panels and then writing one equation for each panel, there results a square set of equations which can be solved immediately by any one of a number of well known numerical methods. This may lead to a large set, however, for a large number of panels, in which case the accuracy of the results may become questionable, especially for the higher terms in the series. By writing an equation for each of a large number of panels but with a smaller number of series terms and then solving the resulting non square set in a least squares sense, this difficulty may be avoided.

For the general analysis of a propeller in non-uniform flow, the following may be of use. The normal inflow perturbation is expressed in a polynomial in the radius of the form:

$$\bar{w}_{Nj} = \sum_{m=0}^M \bar{a}_m r_j^m \quad (4.12)$$

The right-hand side of the set of equations (4.11) may then be replaced by $1, r_j, r_j^2, \dots, r_j^M$ and the equations solved for each, yielding a set \bar{A}_{nm} . The resulting circulation series coefficients for any inflow field expressible in the form (4.12) can then be obtained by a linear combination of these elementary solutions.

$$\bar{A}_n = \sum_m \bar{a}_m \bar{A}_{nm} \quad (4.13)$$

After solving for the circulation, the complex lift coefficient at the various sections may be obtained.

$$\bar{C}_{Lj} = \bar{w}_{2Dj} \bar{F}_j = (\bar{w}_{Nj} + \sum_n \sum_i \bar{A}_{n ni} \bar{w}_{ij}) \bar{F}_j \quad (4.14)$$

where \bar{F}_j is the complex transfer function between lift and normal velocity from two-dimensional unsteady airfoil theory.

The six components of propeller force and moment are then obtained by the appropriate radial integrations of the lift coefficient and complex summations over the blades.

The Circulation and Lift Functions

The circulation and lift functions used in (4.8) and (4.14) above require special discussion.

It must first be noted that both \bar{G} and \bar{F} are functions of the reduced frequency, k^* , where:

$$k^* = \frac{\omega b'}{U} \quad (4.15)$$

in general, where ω is the frequency of the motion or perturbation involved, b' is the semichord of the foil section and U the stream velocity. In the case of the propeller blade section at radius r , this can be written:

$$k^* = \frac{Nb}{\sqrt{\lambda^2 + r^2}} = \frac{N}{2} (\theta_T - \theta_L) \quad (4.16)$$

where b is here expressed as a fraction of the propeller radius. The reduced frequency is a measure of the degree of unsteadiness of the flow. Equation (4.15) can also be put in a form to show that the reduced frequency is a measure of the wave length, ℓ , of a periodic disturbance relative to the chord length.

$$k^* = 2\pi b/\ell \tag{4.17}$$

The value of k^* is seen to depend strongly on the harmonic number and the chord length, and to vary strongly with radius on a given blade.

Most important, \bar{G} and \bar{F} are functions of the form or distribution of the normal velocity over the entire chord length of the section. That is, \bar{G} and \bar{F} have different forms and yield different results for different normal perturbation velocity distribution. Thus, for example, the circulation resulting from a sinusoidal gust is different in amplitude and phase, generally from that resulting from a rigid body heaving motion of the foil although the reduced frequency and amplitude and phase of the maximum normal velocity be made the same in both cases. (21)

In the lifting line analyses of the wing or the propeller in steady flow the downwash, or equivalently the downwash difference, is found at the chordwise position of the lifting line and in the simple form of analysis this velocity is presumed to be constant over the chord at a given spanwise position. It is left to the

more complex lifting surface analyses to compute the variation of the downwash along the chord and hence the so called "curved flow" corrections to the lift. (24)

Here in this vortex line model of the propeller in circumferentially non-uniform flow, the downwash due to the three dimensional nature of the flow field is approximated at one point of the chord at each radius also. The downwash difference is not presumed constant over the chord, however, and it remains to determine the chordwise distribution in order that the appropriate form of \bar{G} and \bar{F} be used.

Considering first the inflow perturbation, the component normal to the blade is obviously sinusoidally distributed along the chord for any harmonic of the flow field. A blade section may thus be considered to be under the influence of sinusoidal gusts the wave length of which are determined by the harmonic number N and the pitch angle of the helix at the radius in question.

In the Reissner analysis of the plane wing in periodic unsteady flow the downwash difference is shown also to be sinusoidally distributed over the chord. (25) The wave length of this distribution is a function of the reduced frequency as expressed in (4.17). The downwash difference in the Reissner approximation is due primarily to the near field effects of the shed vorticity. In the analagous vortex line propeller model it is reasonable to expect that the difference between the effects of the helical geometry of the vortex sheet and the plane configuration are small compared to the latter when the near field is considered.

The downwash difference contributed by the shed vortex sheets of the index vortex line is thus also assumed to have a sinusoidal chordwise distribution.

Considering the shed vorticity of the other blades it can be seen that these helical sheets pass again and again behind the index blade; the first few turns at least being in fairly close proximity to that blade. The strength of the vorticity on these sheets is sinusoidal in the angular coordinate, and at any particular angular position the strength of the vorticity on all the turns of all the sheets is in phase at a given radius. Thus it may be expected that the helical shed vortex sheets will induce a normal velocity on the index blade which is of the nature of a sinusoidal gust system.

The velocities induced by the bound vorticity of the other blades, here represented by the vortex lines, may perhaps be more uniform over the chord. Again this is presumed small in comparison with the other induced velocities due to the usually large distance between blades.

Thus both the downwash difference and the inflow perturbation are considered to be predominantly of the same chordwise distribution, namely sinusoidal. Further, the wavelengths of both are the same at any radius but they are not, in general, in phase with one another. The sum of the inflow perturbation and the downwash difference is considered, as mentioned previously, the inflow normal velocity perturbation that a two dimensional chordwise strip of blade must experience. The sum of the two sinusoids is a third sinusoid whose complex amplitude at the

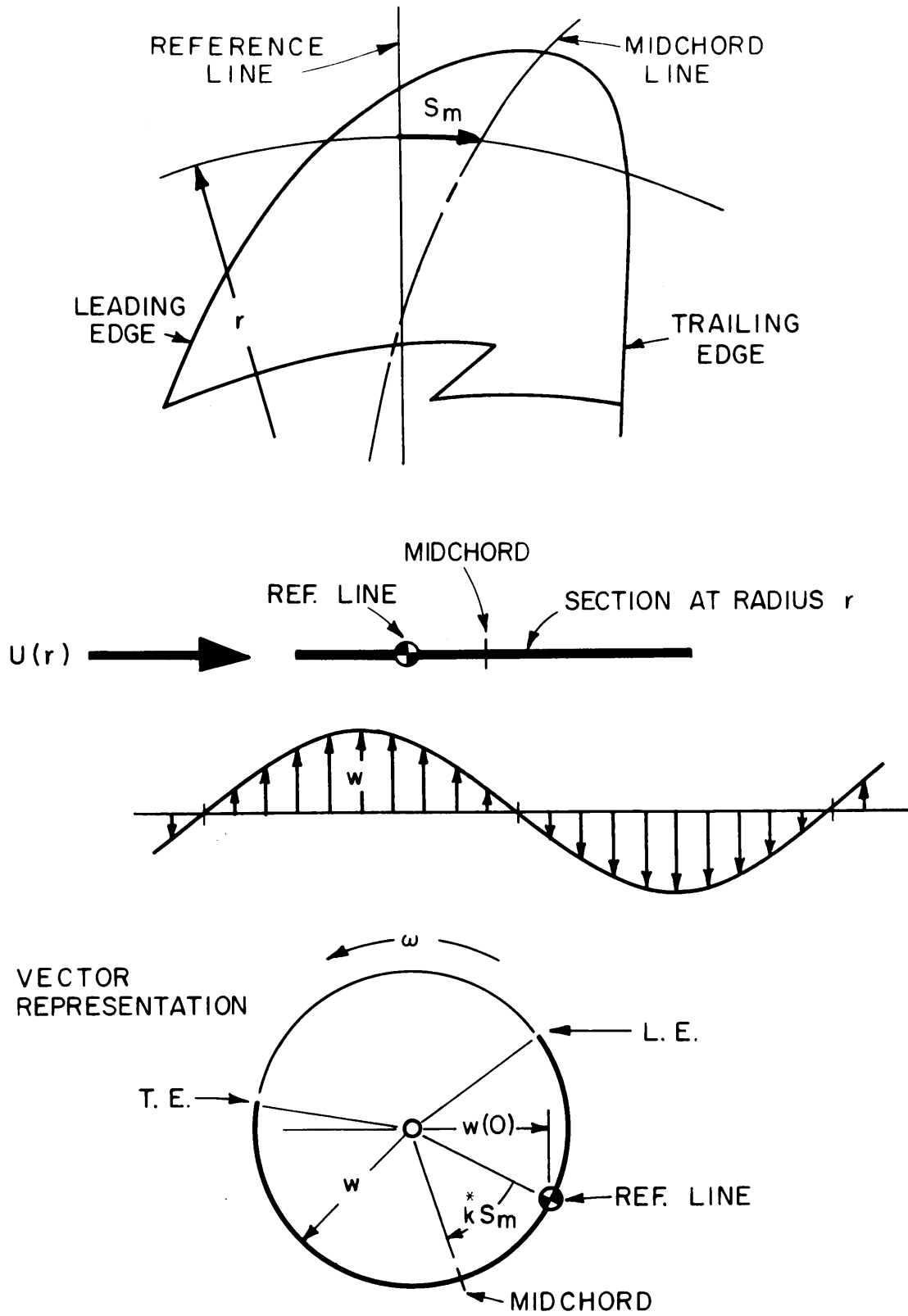


FIG. 4.1 PHASE SHIFT DUE TO BLADE SKEW

at the vortex line is the sum of the two complex velocities evaluated there. The amplitude of the resultant at any chordwise position is given by a linear phase shift from this point. The use of the same lift and circulation functions for the inflow and induced flow in (4.10) and (4.14) is thus justified.

Equally as important as the distribution of inflow perturbation and downwash difference are the phase shifts due to blade skew, resulting in phase shifts of the total downwash, circulation and lift. Referring to figure (4.1) the complex normal velocity at a particular instant of time, at the section midchord is given in terms of the velocity at the reference line and the coordinate of the midchord:

$$\bar{w}(s_m) = \bar{w}(0)e^{iks_m^*} \quad (4.18)$$

where the distance s_m is considered positive in the direction downstream of the reference line and is dimensionless on the basis of the section semichord at the radius in question.

The complex lift function used is the Sears function for the lift coefficient of a flat plate two dimensional airfoil subject to sinusoidal gusts, as modified by (4.18): (21)

$$\bar{F} = -2\pi \frac{ie^{-iks_m^*}}{k [K_0(ik^*) + K_1(ik^*)]} \quad (4.19)$$

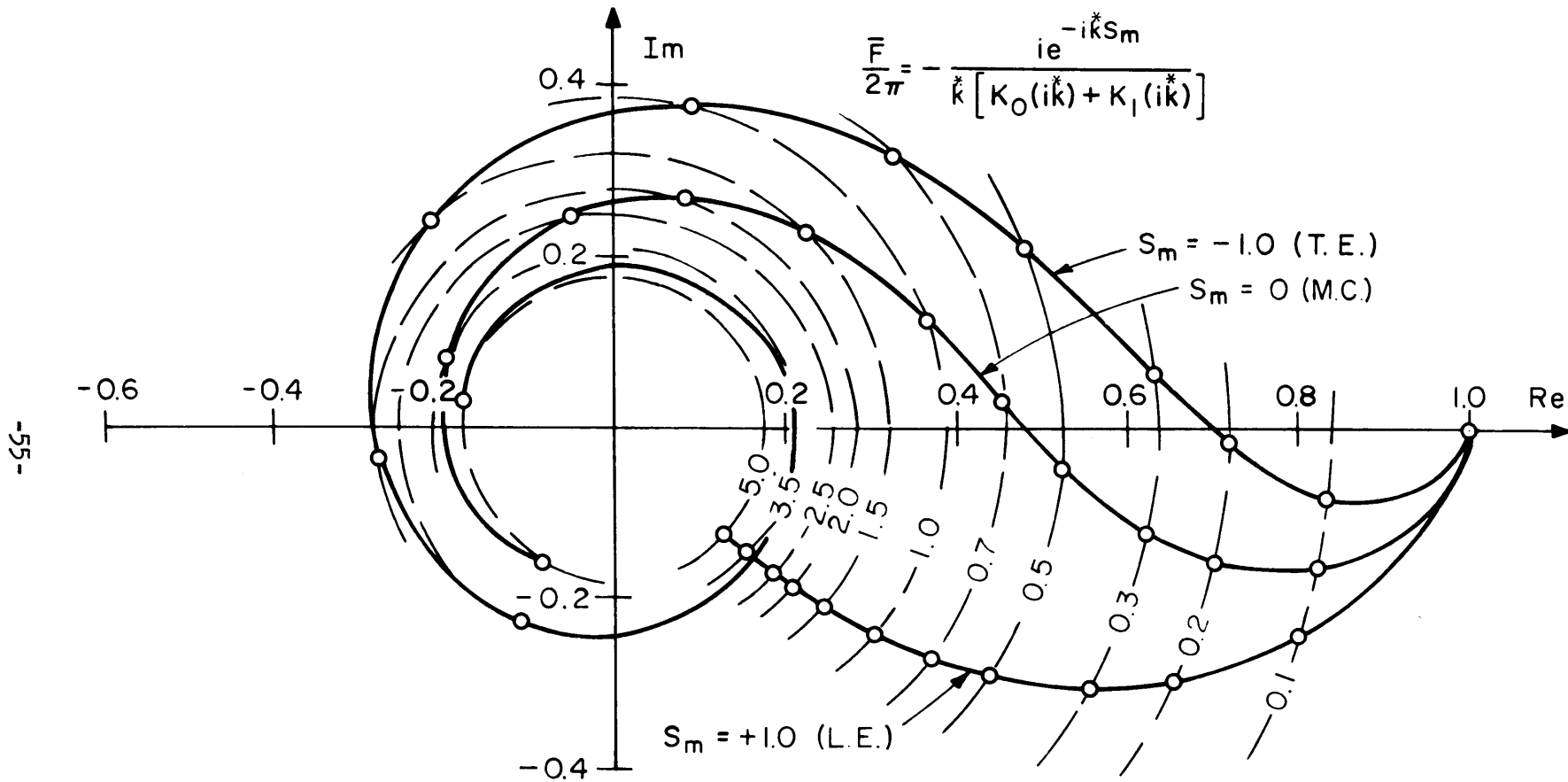


FIG. 4.2 LIFT COEFFICIENT-FLAT PLATE 2-D AIRFOIL IN SINUSOIDAL GUSTS
 FIGURES ON CROSS CURVES ARE VALUES OF THE REDUCED FREQUENCY, \bar{k}

The complex circulation for the sinusoidal gust can be deduced from Sears work (21), or can be gotten from the quasi-steady circulation (see Appendix A) by a formula of Kemp. (22). Modified according to (4.18) this is:

$$\frac{\bar{G}}{b\sqrt{\lambda^2 + r^2}} = -2\pi \frac{i \left[J_0(k^*) - i J_1(k^*) \right] e^{-ik^*(1 + s_m)}}{k^* \left[K_0(ik^*) + K_1(ik^*) \right]} \quad (4.20)$$

These functions are shown in Figures 4.2 and 4.3 respectively for reference positions at the leading edge, $s_m = +1$; midchord, $s_m = 0$; and the trailing edge, $s_m = -1$. It may be noted that for a given value of k^* only the phase changes with the position of the reference point, the amplitude is naturally unchanged.

The case considered here has been that of a propeller rotating uniformly in a non-uniform stream where the inflow is gust-like. If the case, for instance, of a propeller oscillating axially or torsionally in uniform flow is considered then the functions \bar{G} and \bar{F} in (4.10) and (4.14) must be replaced by those pertinent to, in this case, solid body heaving motion of the section, but only for the inflow; the functions to be multiplied by the downwash difference presumably remain as above due to its sinusoidal chordwise distribution.

If it is found necessary to do so, the circulation and lift due to the induced velocities of the bound vortices of the other blades may be treated by special functions tailored to the distribution of these velocities.

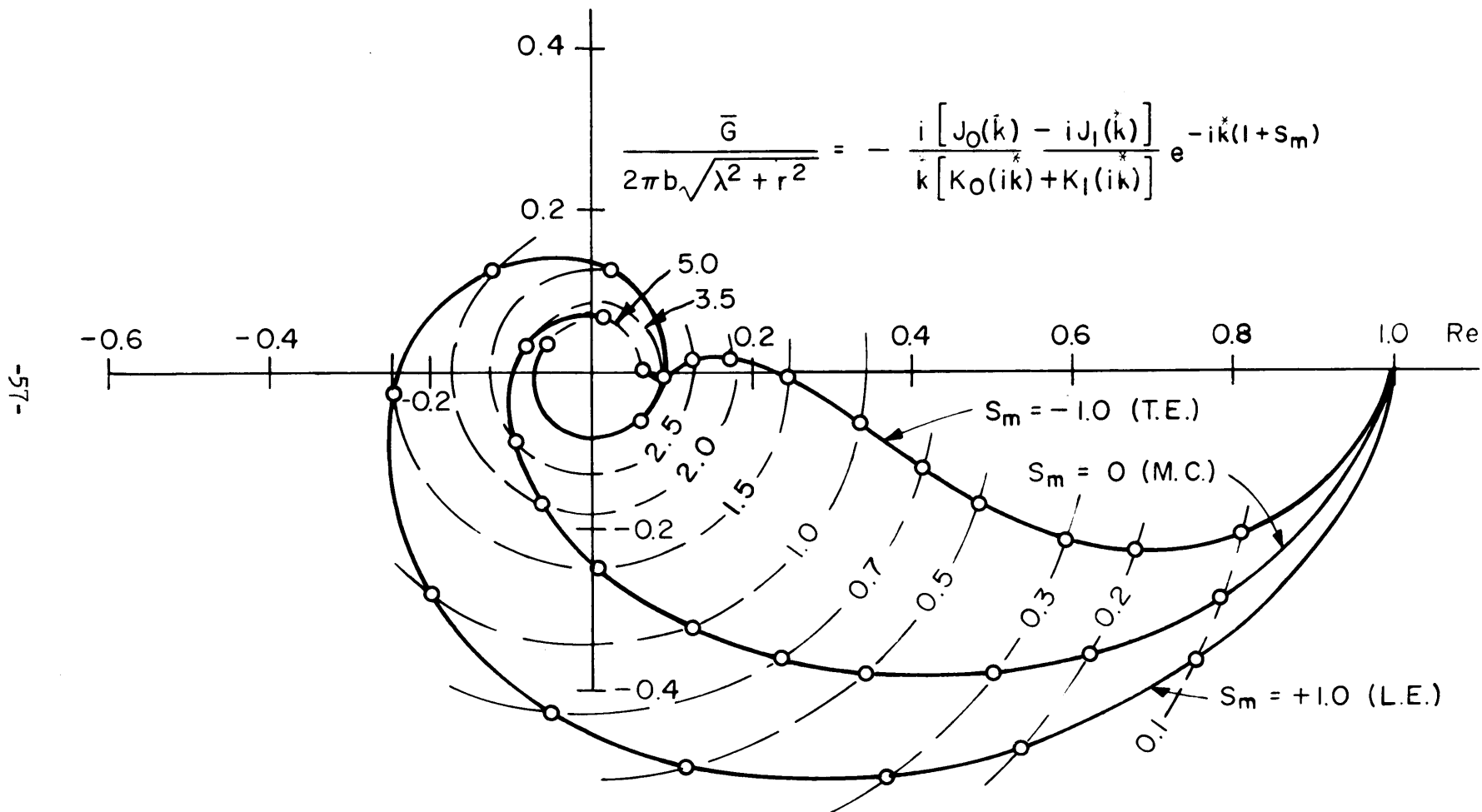


FIG. 4.3 CIRCULATION - FLAT PLATE 2-D AIRFOIL IN SINUSOIDAL GUSTS
 FIGURES ON CROSS CURVES ARE VALUES OF THE REDUCED FREQUENCY, k

CHAPTER V

COMPUTATION OF THE DOWNWASH DIFFERENCE MATRIX

Summation Before Integration

In order to evaluate the elements of the downwash difference matrix, \bar{W}_{ij} , the integrations of equation (3.17) must be carried out. Analytic integration seems out of the question, so some numerical scheme must be used. The most straightforward method is to employ a powerful integration formula such as the five point Gauss rule over a number of intervals up to some large value of the coordinate ϕ . The remainder of the integrals from this point to infinity may be approximated by analytical integration when the integrand is simplified for large ϕ . These latter integrations result in sine and cosine integral functions. The entire process must be carried out separately for each harmonic number N being considered.

A more interesting way to evaluate these integrals is available, however. We may take advantage of the assumed lightly loaded condition of the screw which eliminates distortion of the helical surfaces swept out by the blades. Then, note that at a given angle relative to the reference line the vorticity strengths on all the turns of all the helices are in phase at a given radius. This may be deduced by inspection of (3.17).

The infinite integrations in the angular coordinate can then be replaced by angular integrations over one revolution of products of sines and cosines with infinite summations taken at constant angle. The terms in the summed series are the values of the geometrical parts of the original integrands as evaluated on successive turns of the helical vortex sheets at constant angle. The points of evaluation of the integrands are illustrated in Fig. 5.1.

To put this in mathematical form the change of variable:

$$\phi = \varphi + \delta_k \quad (5.1)$$

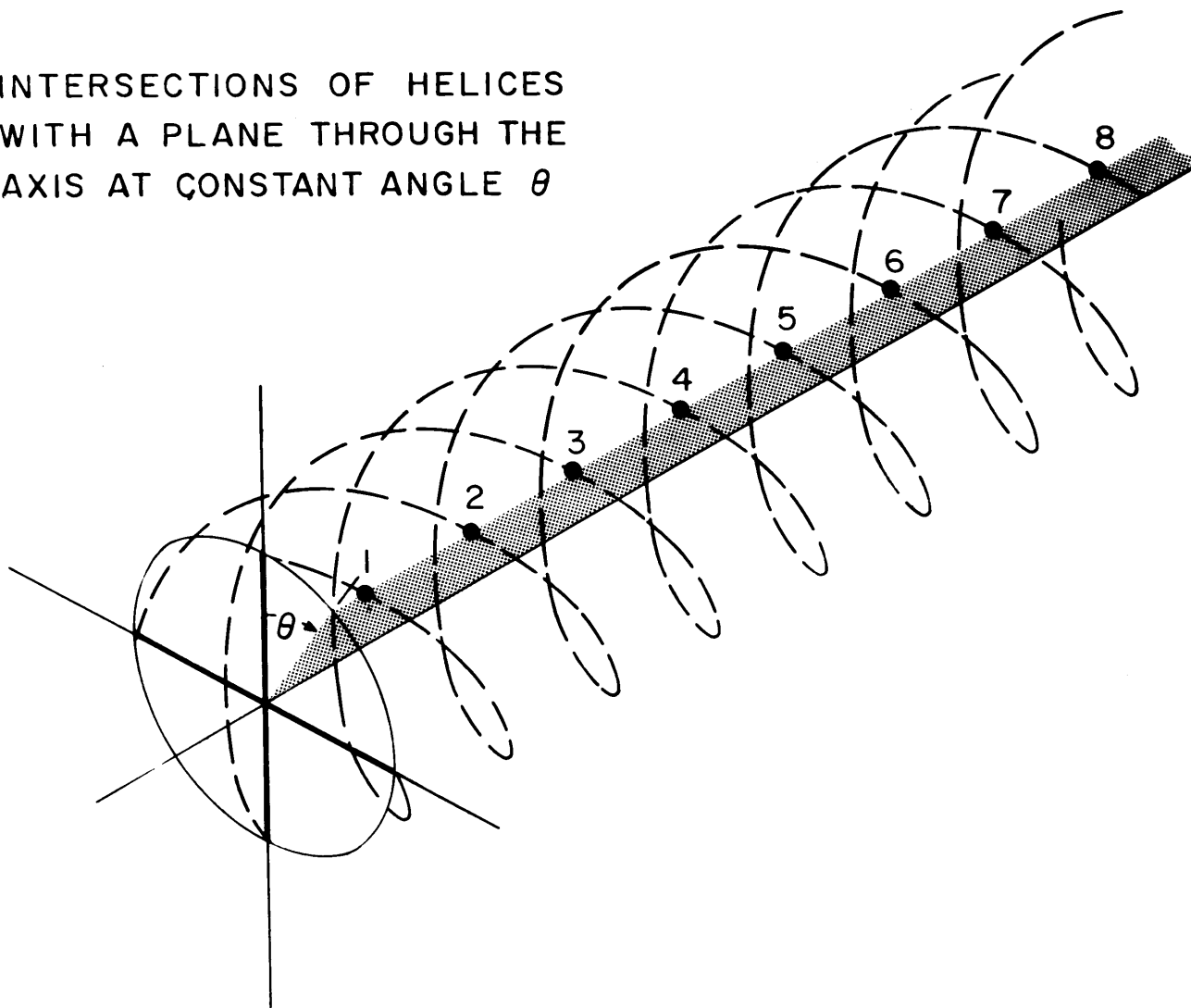
is made. The coordinate ϕ is thus the angular coordinate measured from the index blade, independent of the helices. Considering first the integral for the streamwise trailing vortices of a panel, this may be written:

$$\bar{I}_s = \sum_{k=0}^{K-1} \int_{\delta_k}^{\infty} \left[\frac{\eta(1-p^2) \cos \phi + p^2 - \eta^2 - \eta p^2 (\phi - \delta_k) \sin \phi}{(\eta^2 - 2\eta \cos \phi + p^2 (\phi - \delta_k)^2 + 1)^{3/2}} \right]_{\eta_1}^{\eta_2} e^{-iN\phi} d\phi \quad (5.2)$$

Now the harmonic functions of ϕ are not disturbed if the argument is replaced by $\phi + 2n\pi$ where n is an integer. Doing so, and summing over all positive n the infinite integral is replaced by an infinite sum of integrals over the interval $(\delta_k, \delta_k + 2\pi)$. Now the angle between the index blade and the k th blade is:

$$\delta_k = k \frac{2\pi}{K} \quad (5.3)$$

INTERSECTIONS OF HELICES
WITH A PLANE THROUGH THE
AXIS AT CONSTANT ANGLE θ



- 60 -

FIG. 5.1

so that in the terms containing it we can write:

$$\bar{\phi} + 2m\pi - k \frac{2\pi}{K} = \bar{\phi} + \frac{2\pi}{K} m \quad (5.4)$$

Combining the sums over n and k , and interchanging the order of integration and summation, there results:

$$\bar{I}_s = \int_0^{2\pi} \sum_{m=0}^{\infty} \left[\frac{\eta(1-p^2)\cos\bar{\phi} + p^2 - \eta^2 - \eta p^2 (\varphi_0 + m \frac{2\pi}{K}) \sin\bar{\phi}}{(\eta^2 - 2\eta \cos\bar{\phi} + p^2 (\varphi_0 + m \frac{2\pi}{K})^2 + 1)^{3/2}} \right]_{\eta_1}^{\eta_2} e^{-iN\bar{\phi}} d\bar{\phi} \quad (5.5)$$

where φ_0 is the smallest positive value taken on by the quantity $(\bar{\phi} - \delta_k)$, that is, φ_0 is a function of $\bar{\phi}$ and has values in the range $0 \leq \varphi_0 < \frac{2\pi}{K}$.

Following the same procedure, the integral for the radial shed vorticity in the general case ($\eta \neq 1$) can be written:

$$\bar{I}_n = \int_0^{2\pi} \sum_{m=0}^{\infty} \left\{ \frac{\sin\bar{\phi} + p^2 (\varphi_0 + m \frac{2\pi}{K}) \cos\bar{\phi}}{\sin^2\bar{\phi} + p^2 (\varphi_0 + m \frac{2\pi}{K})^2} \right\} \left[\frac{\eta - \cos\bar{\phi}}{(\eta^2 - 2\eta \cos\bar{\phi} + p^2 (\varphi_0 + m \frac{2\pi}{K})^2 + 1)^{1/2}} \right]_{\eta_1}^{\eta_2} e^{-iN\bar{\phi}} d\bar{\phi} \quad (5.6)$$

The special integrand for $\eta = 1$ and $k = 0$ will be treated later.

The Sum Functions

Given the set of parameters defining the panels i and j namely, η_1 , η_2 , and p, the sums in (5.5) and (5.6) above are functions of ϕ only. Denoting the former $S_S(\phi)$ and the latter $S_r(\phi)$, the downwash difference of (3.17), ignoring for the moment the special case at $\eta=1$, may be written:

$$\bar{w}(r, \rho) \cdot 4\pi r^2(p^2+1) = \sum_{k=1}^{K-1} \frac{e^{-iNk}}{\sin \delta_k} \left[\frac{\eta - \cos \delta_k}{\sqrt{\eta^2 - 2\eta \cos \delta_k + 1}} \right]_{\eta_1}^{\eta_2} - iN \int_0^{2\pi} S_r(\phi) e^{-iN\phi} d\phi + \int_0^{2\pi} S_s(\phi) e^{-iN\phi} d\phi \quad (5.7)$$

The major part of the downwash difference can thus be simply computed for any harmonic number N whatever by harmonic analyses of the sum functions. In particular for N=0 the first and second terms drop out and the steady induced velocity of a set of streamwise trailing vortices of constant strength is given by the integral of S_s over $(0, 2\pi)$, or 2π times its average value. For any N which is an integral multiple of K the first term above is zero because it is odd in δ_k .

The sum functions for a typical panel set and control point radius are shown in Fig. 5.2. The discontinuities at $\phi = 0, \pi/2, \pi,$ and $3\pi/2$ in these curves are due to the starts of new vortex sheets at the vortex lines and the consequent steplike

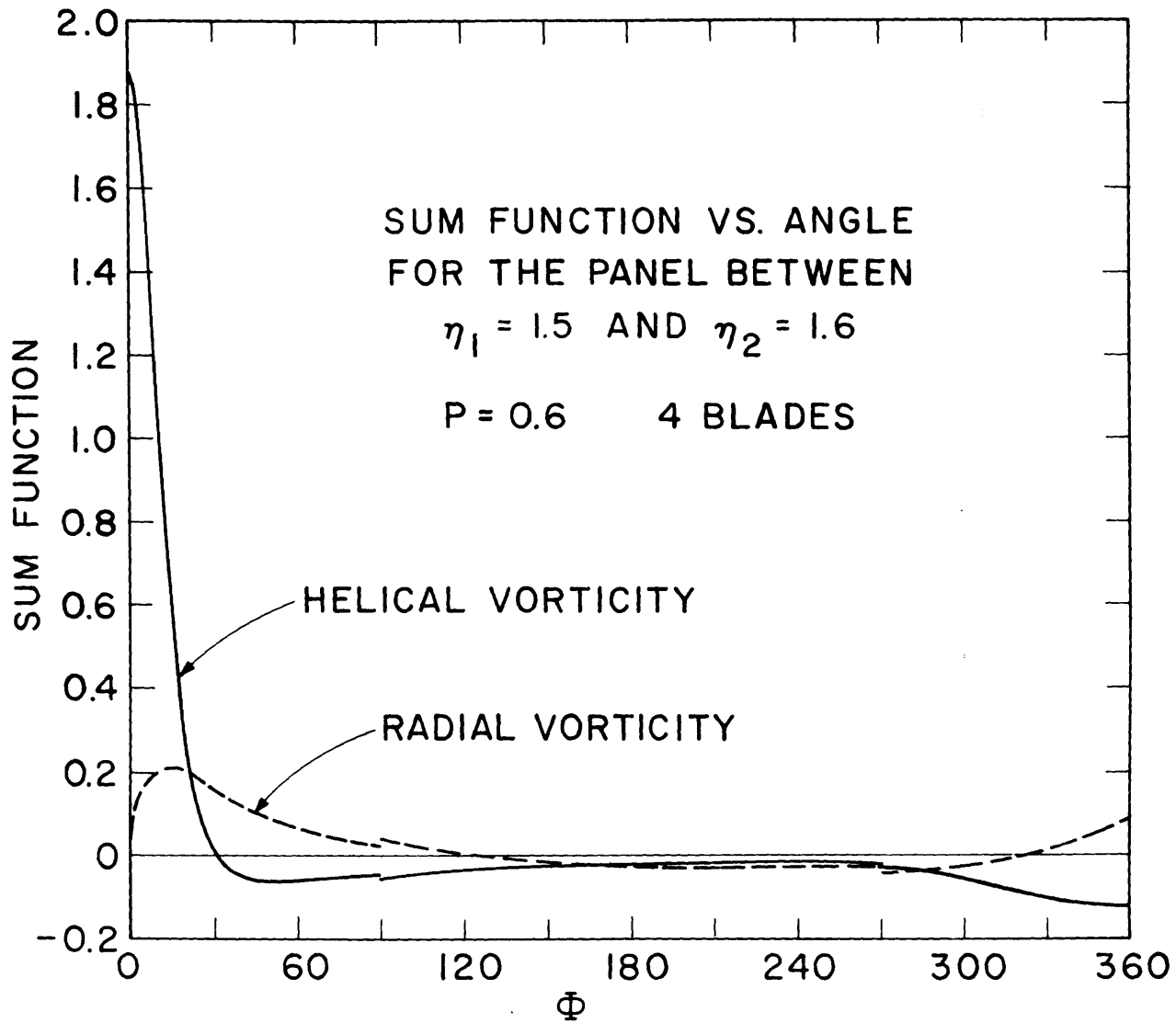


FIG. 5.2

increase in the contribution to the induced velocity. These are thus a consequence of the simplified model employed.

Carrying out the Summations

The sum functions represent infinite summations which if carried out directly are no more attractive than the original infinite integrations. The infinite sums may be approximated, however, by the use of the Euler-Maclaurin sum formula, which in its truncated form may be written: (29)

$$\sum_{n=0}^{\infty} f(\alpha + nh) \approx \frac{1}{h} \int_{\alpha}^{\infty} f(x)dx + \frac{1}{2} f(\alpha) - \frac{h}{12} f'(\alpha) + \frac{h^3}{720} f'''(\alpha) - \dots \quad (5.8)$$

The infinite sum is thus approximated by an infinite integral plus a series of correction terms involving derivatives of the function evaluated at the initial value.

In the case of both the radial and streamwise vorticity the integral can be easily evaluated since it is in the variable φ_0 and not ϕ . Also the derivatives are taken with respect to φ_0 . The correction series is in practice restricted to the first few terms.

Now the accuracy of this approximation behaves peculiarly in that the error can be reduced by retaining additional correction series terms, but only up to a certain extent. If too many terms are retained the value oscillates wildly with each additional term; the correction series diverges. The number of terms to be

retained to give the best result turns out to be roughly proportional to the initial value α . (29)

Use of the formula for small values of α are thus doomed to failure since the best result is obtained with an insufficient number of correction terms. This situation is remedied by actually summing a few terms of the original series and then entering the formula with a larger initial value. Carrying out the integration and the differentiations up to the third derivative for the streamwise vorticity, the sum function becomes:

$$\begin{aligned}
 S_s(\Phi) = & \sum_{m=0}^M \frac{A + B \left(\varphi_0 + m \frac{2\pi}{K}\right)}{\left[C + D \left(\varphi_0 + m \frac{2\pi}{K}\right)^2 \right]^{3/2}} \\
 & + \frac{K}{2\pi} \left[\frac{A}{C\sqrt{D}} - \left(\frac{A}{C} \varphi_m - \frac{B}{D} \right) (C + D\varphi_m^2)^{-\frac{1}{2}} \right] + \frac{A + B\varphi_m}{2(C + D\varphi_m^2)^{3/2}} \\
 & - \frac{\pi}{6K (C + D\varphi_m^2)^{3/2}} \left[B - 3D\varphi_m \left(\frac{A + B\varphi_m}{C + D\varphi_m^2} \right) \right]
 \end{aligned} \tag{5.9}$$

Where:

$$\begin{aligned}
 \varphi_m &= \varphi_0 + M \frac{2\pi}{K} \\
 A &= \eta(1-p^2) \cos \Phi + p^2 - \eta^2 \\
 B &= -\eta p^2 \sin \Phi \\
 C &= \eta^2 - 2\eta \cos \Phi + 1 \\
 D &= p^2
 \end{aligned}$$

with the whole evaluated between the limits (η_1, η_2) . The sum function for the radial vorticity is not presented here due to its complexity. The above will suffice for the present discussion.

The question now arises as to how many basic series terms or helix turns need actually be summed with a given number of correction series terms in order to insure stabilization of the result. Secondly, how many correction series terms need be included in order to insure convergence to the true result?

This has been investigated for (5.9) in a typical case. Sum functions at various angles were computed by the formula while retaining correction terms through both the first and third derivatives for values of M from zero to twenty. Convergence to the correct result was proved by the agreement between the stabilized results of the two and three term correction series cases. Further the mean value of the sum function so determined yielded a steady induced velocity which was in good agreement with one computed from the induction factors of Lerbs. (23)

The same procedure was followed with the formulation for the radial vorticity. One and two correction terms were retained in this case; the third derivative being too unwieldly to consider. Again convergence was proved by the final agreement between the values given by the one and two correction term cases. Direct numerical integration as described in the first paragraph of this chapter was performed for the zeroth harmonic, resulting in a

4 BLADES, $\eta = 1.6$, $\lambda/r = 0.6$

3 TERM CORRECTION SERIES ○ 6 DIGITS BEYOND DECIMAL STABILIZED
 □ 5 DIGITS BEYOND DECIMAL STABILIZED
 2 TERM CORRECTION SERIES ● 6 DIGITS BEYOND DECIMAL STABILIZED
 ■ 5 DIGITS BEYOND DECIMAL STABILIZED

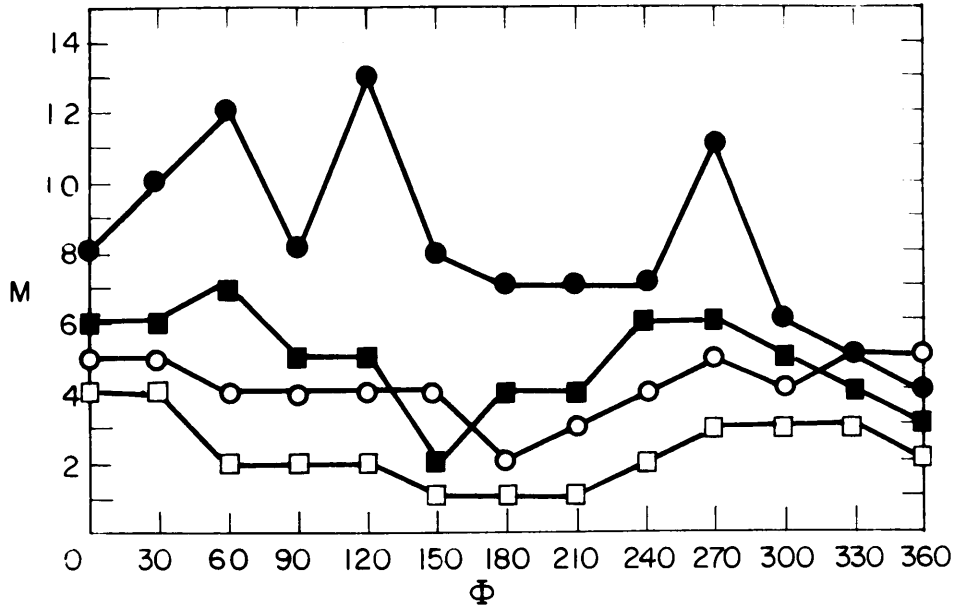


FIG. 5.3 NUMBER OF TURNS SUMMED - STREAMWISE VORTEX LINES

4 BLADES, $\eta_1 = 1.5$, $\eta_2 = 1.6$, $\lambda/r = 0.6$

2 TERM CORRECTION SERIES ○ 6 DIGITS BEYOND DECIMAL STABILIZED
 □ 5 DIGITS BEYOND DECIMAL STABILIZED
 1 TERM CORRECTION SERIES ■ 5 DIGITS BEYOND DECIMAL STABILIZED

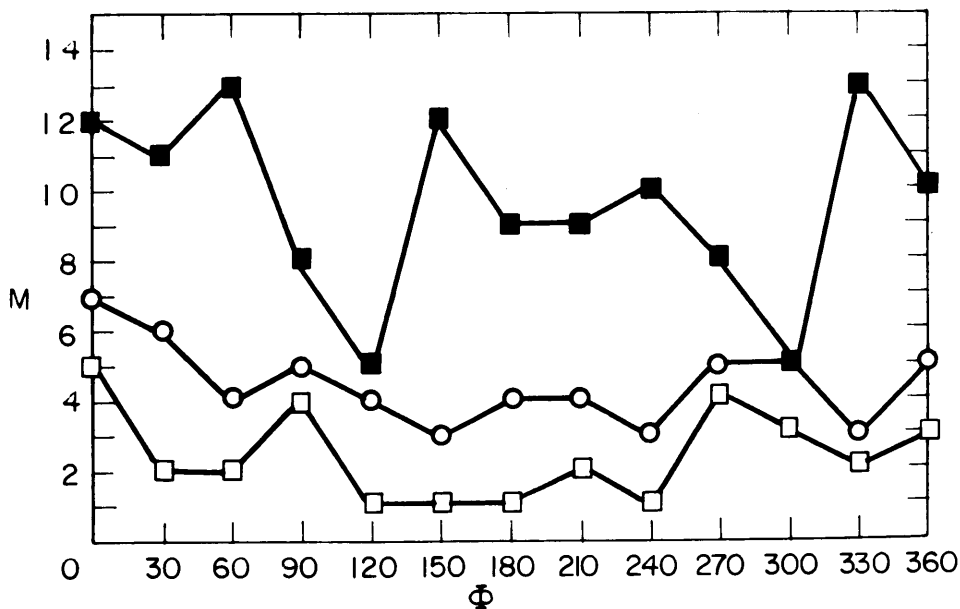


FIG. 5.4 NUMBER OF TURNS SUMMED - RADIAL VORTICITY

satisfactory check on the mean value of the sum function; although this has no physical significance for the radial vorticity.

The number of helix turns summed, M , in order to stabilize five and six digits beyond the decimal is shown in Figures 5.3 and 5.4 for the case considered. It appears that the following values of M are sufficient for nearly all ϕ :

| | M, for | |
|-----------------------------|----------|----------|
| | 6 digits | 5 digits |
| A. Streamwise vortex lines | | |
| 1. 3 term correction series | 5 | 4 |
| 2. 2 term correction series | 10 | 6 |
| B. Radial Vorticity | | |
| 1. 2 term correction series | 5 | 4 |
| 2. 1 term correction series | -- | 12 |

The one term correction series for the radial vorticity requires over 20 turns for 6 digit stabilization. This extremely truncated series is considered inadequate. For a three term series for the streamwise vortices and a two term series for the radial vorticity it is thus seen that it is required that summation of the integrand be carried out over an axial distance of the order of one pitch of the screw before the approximation for the sum to infinity may be applied.

It can be seen in Fig. 5.2 or by examination of expression (5.5) that the magnitude of the streamwise vorticity sum function, where it is not small, is composed for the most part by the

contribution of the first turn summed. The near field effects are the most influential, as would be expected. In this respect the Euler-Maclaurin sum formula provides a generally small correction to the values obtained by summing a few helix turns. Judging from the magnitude of the streamwise sum function at its greatest, which in the case depicted in Fig. 5.4 is of the order 1, the requirement of accuracy of order 10^{-5} or 10^{-6} in this correction is seen to be very stringent and probably unnecessarily conservative in view of the final result, even though this accuracy is easily attained. This accuracy is less conservative for the radial vorticity sum function which is seen to have a magnitude of 10^{-1} here.

Difficulties arise in determining the radial vorticity sum function at $\eta = 1$ due to the presence of the term $2/\phi$. This term appears only for the vorticity shed by the index blade and must therefore be subtracted but once per revolution instead of K times or once for each helix as with the other terms. Further, the sum $\sum_{n=0}^{\infty} 2/(\phi + 2n\pi)$ does not converge. The harmonic analysis of

this non-existent sum for $N \neq 0$, however, is well defined.

In order to avoid these difficulties the term $2/\phi$ is subtracted only from the first term actually summed. The rest of the sum and the Euler-Maclaurin evaluation to infinity are then carried out exactly as for any other panel. The remainder of

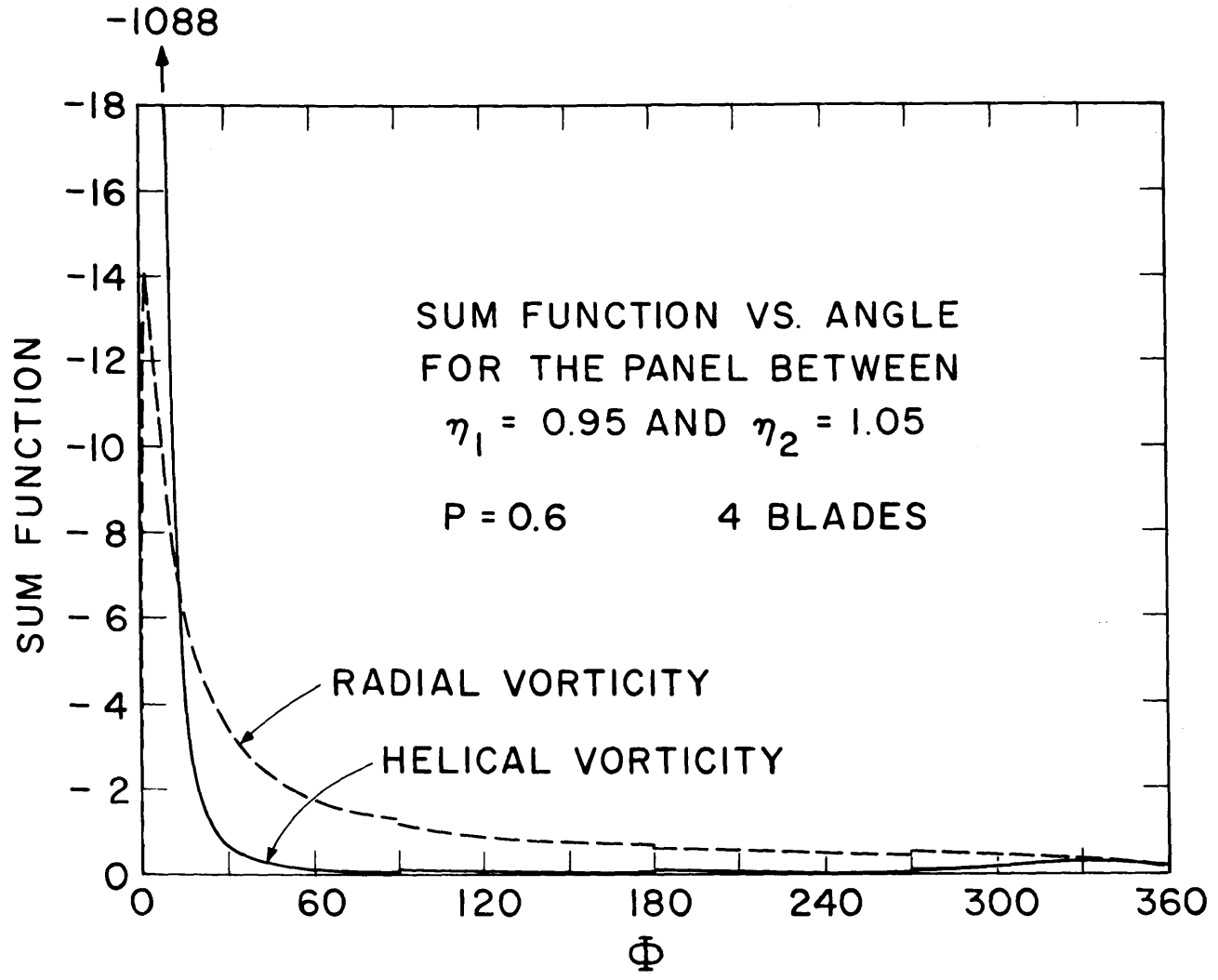


FIG. 5.5

this term on the other turns of the index blade helix is then removed by subtracting the following integrals from the harmonic analysis of the sum function:

$$2 \int_{2\pi}^{\infty} \frac{e^{-iN\phi}}{\phi} d\phi = -2 \left[\text{CI}(2\pi N) + i \frac{\pi}{2} - i \text{SI}(2\pi N) \right] \quad (5.10)$$

The CI and the SI are the cosine and sine integral functions, respectively, which are tabulated or computable by standard means. (30)

The sum functions for a set of panels at $\eta = 1$ in a typical case are shown in Fig. 5.5. Here the radial vorticity function has had the term $2/\phi$ subtracted only in the first revolution of the helix as described above.

CHAPTER VI

AN APPROXIMATION FOR LOW HARMONIC NUMBERS

Nature of the Harmonic Analysis of the Sum Function

Inspection of Figures 5.2 and 5.5 reveals that the streamwise vorticity sum function is very sharply peaked in the neighborhood of $\phi = 0$. So marked is this characteristic that there is a strong resemblance to the impulse function. The spectrum of the impulse function is a constant; the harmonic analysis of the similar $S_S(\phi)$ function, therefore, may be expected to vary but slowly with N .

It may further be noted that the streamwise sum function is much larger in magnitude than the radial, there being an order of magnitude between the peak values of the two functions in Fig. 5.2 and two orders of magnitude for the case $\eta = 1$ in Fig. 5.5. The signs of the sum functions for $\eta = 1$ are opposite those for $\eta \neq 1$, however, so that in effect the induced velocities at the location of a particular panel are reduced by the induction of the neighboring panels. Both the radial and streamwise sum functions are affected in this way and it remains to be seen whether the streamwise sum function retains its characteristic shape and magnitude compared with the radial function when the influences of all the vorticity panels along the radius are included.

In order to investigate this we may form the set of sums over the propeller radius of the sum functions weighted by the set of radial circulation series functions defined in (4.2). Denoting the sum function for the velocity at the j th panel due to vorticity of the i th by S_{ij} , these are:

$$S_{nj}(\phi) = \sum_i f_{ni} S_{ij}(\phi) \quad (6.1)$$

for either the radial or streamwise vorticity.

In the course of developing a computational scheme for the downwash difference matrix a set of these functions has been evaluated for the first five values of n at various radii r_j . These computations have been made for a typical case of a four blade propeller, with hub radius of $0.2R$ and a pitch of $\lambda = 0.3$. Suffice it to state that the resulting total sum functions do retain the particular and relative characteristics displayed by the individual panels but to a less marked degree.

The harmonic analysis of the set of functions for the radius $r_j = 0.675$ was carried out through $N = 4$ and the results combined according to equation (5.7) to form the real and imaginary parts of the downwash difference matrix. This downwash difference matrix is represented by the bar spectra of Figure 6.1. Here it may be noted that the amplitude of the downwash difference does not generally vary strongly with N from the value at $N = 0$ within each set. This is less true for the set $n = 1$ at this

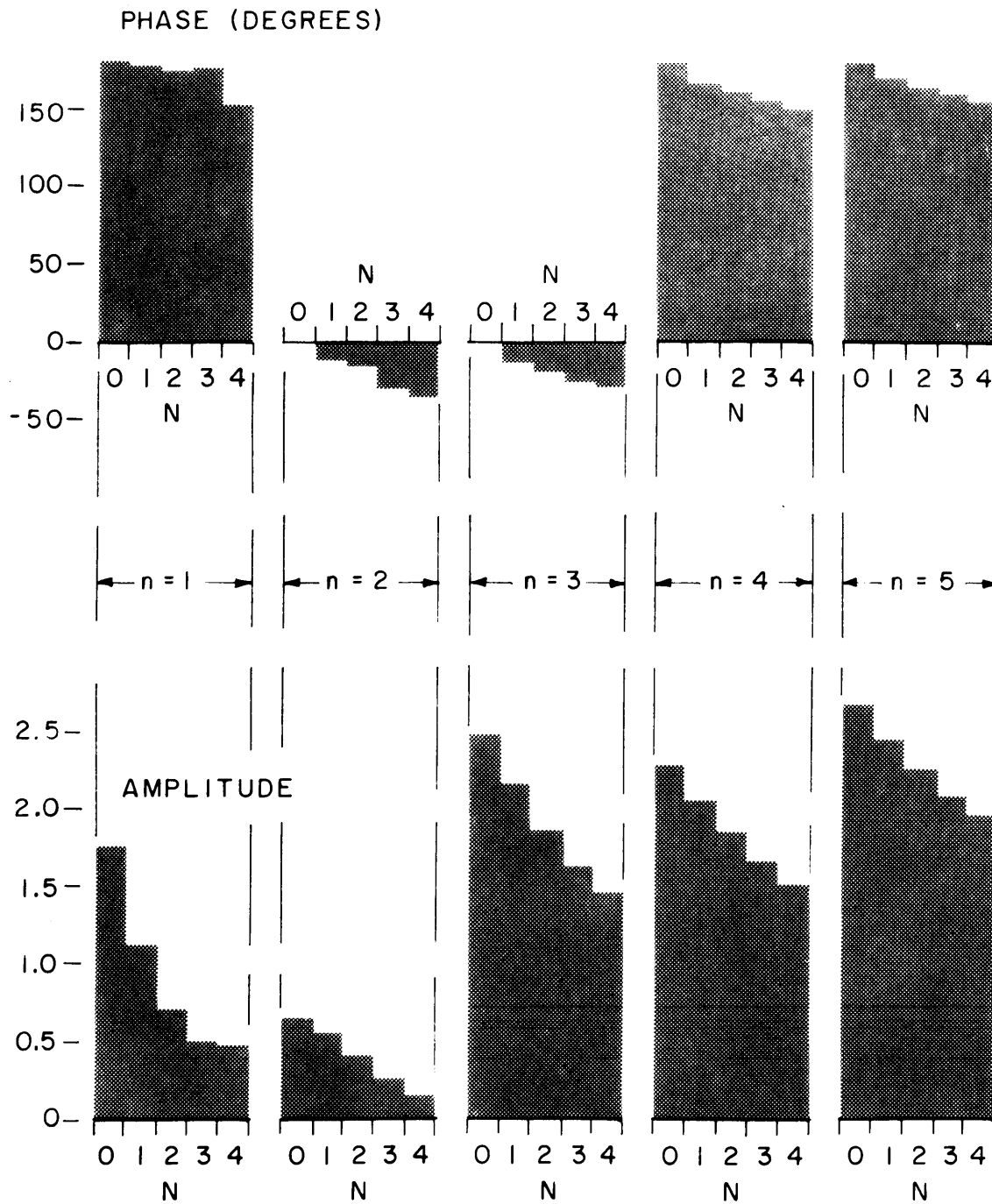


FIG. 6.1 HARMONIC ANALYSIS OF THE DOWNWASH DIFFERENCE
 $\lambda = 0.3, r = 0.675$

particular radius. The phase angles also do not change rapidly as N increases from zero. This behavior is as expected from the impulse-like nature of the streamwise vorticity sum function and the relatively lesser importance of the radial sum function. It must be noted that this behavior is influenced by the radial location r_j considered, but this case is considered typical.

The purpose of the above considerations is to demonstrate the reasonable validity of, and the thought process leading to the approximation to the downwash difference matrix for small values of N by the matrix for $N = 0$. The zero harmonic number downwash difference is the induced velocity in steady flow.

Physically the possible applicability of the steady induced velocity may be appreciated when it is remembered that the induced velocity even in unsteady flow is due primarily to the effects of the nearby vorticity; a fact which is reflected in the nature of the sum functions. So long as the wave length of the disturbance is large compared to the extent of the influential near field, the induced velocity is approximately equal to that for infinite wave length. Long wave length of course requires low harmonic number.

The propeller forces for small harmonic numbers are usually of interest for propellers with a small number of blades, that is two, three and perhaps four. In these cases, the inter-blade distances are large and the velocities induced by the vortex

lines representing the blades may be expected to be small.

Neglecting the contribution of the blades, the approximation to the downwash difference from (5.7) is written:

$$\bar{W} \cdot 4\pi r^2 (p^2 + 1) \approx \int_0^{2\pi} S_s(\phi) d\phi \quad (6.2)$$

or in matrix notation:

$$\bar{W}_{ijN} \approx W_{ijo} \quad (6.3)$$

The steady state induced velocity may be computed by use of Lerbs' induction factors (23) or may even be approximated by the local application of the Goldstein functions (31).

However, for machine computation, routines are available for the rapid calculation of steady flow induced velocities based on the exact potential of a set of helical vortex lines or approximations thereof.

This zeroth harmonic approximation must in no way be confused with a quasi steady analysis or model. The complex simultaneous equations (4.11) must still be solved for the complex circulation distribution with the use of the unsteady circulation function \bar{G} . Only the correction to the unsteady strip theory, namely the downwash difference, is approximated by a steady model.

CHAPTER VII

MEASUREMENT OF BLADE FREQUENCY THRUST AND TORQUE IN THE PROPELLER TUNNEL

Testing in the Propeller Tunnel

Experimental results are needed to evaluate the several existing and proposed methods of calculating the periodic propeller forces in circumferentially non-uniform flow. For valid comparison, the experimental conditions must simulate as closely as possible the important conditions assumed in the mathematical models. These are primarily a known inflow velocity field and an absence of nearby boundaries in the flow.

A water tunnel with a velocity distribution control device provides a fixed and easily measured flow field that can presumably be readily altered to simulate different inflow conditions. The devices used in this connection to date have been either screens in geometric patterns (10) or an array of valve controlled nozzles (32), both producing only axial velocity variations which are sufficient. In either case, the screw must be positioned distant enough from the device to insure that the pressure field due to screw loading has a negligible influence on the velocity distribution produced. A sufficient axial distance, one to two screw diameters, is easily attained, and the velocity field measured in the absence of the screw is reasonably assumed the same that exists with the screw working.

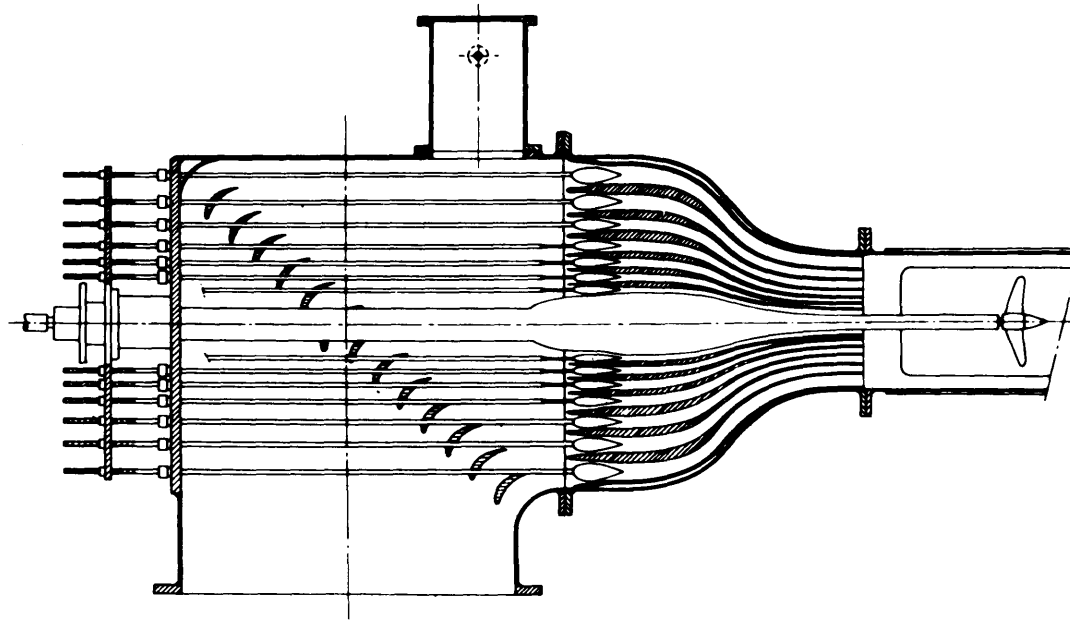


FIG. 7.1 FLOW REGULATOR-DELFT TUNNEL
from: W. P. A. van Lammeren, ref. (32)

In a tunnel there need be no extraneous boundaries in the vicinity of the screw, the diameter of a closed jet test section generally being at least twice the screw diameter, and that of an open jet section being much greater.

Further, a water tunnel allows continuous operation which simplifies measurement, and the screw loading is easily varied by control of the mean water velocity. Operation at high speed is possible, if the frequency response of the mechanical and electrical systems allows it, providing high Reynolds number in the flow and sufficiently large forces which ease the sensitivity problem. Finally, if the mechanical system is designed for it, the screw may be operated with the tunnel pressure reduced and periodic forces measured under cavitating conditions. Present unsteady propeller theory does not cover this condition, but it can be assumed that this will soon be investigated.

Recognizing the need for applicable experimental studies and the advantages of tunnel testing, the author has designed and developed a propeller dynamometer system for direct dynamic measurements of blade frequency thrust and torque for a small water tunnel with field control. This experimental work was carried out at the Technological University of Delft, The Netherlands, by the author as a Fulbright Scholar in that country during the academic year 1962-63.

The converging nozzle before the test section of this tunnel is divided into 146 separate nozzles, the flow through each of which is controlled by a valve at its inlet end as illustrated in Fig. 7.1. The circumferential distribution of the axial velocity in the test section is adjustable over a wide range by the

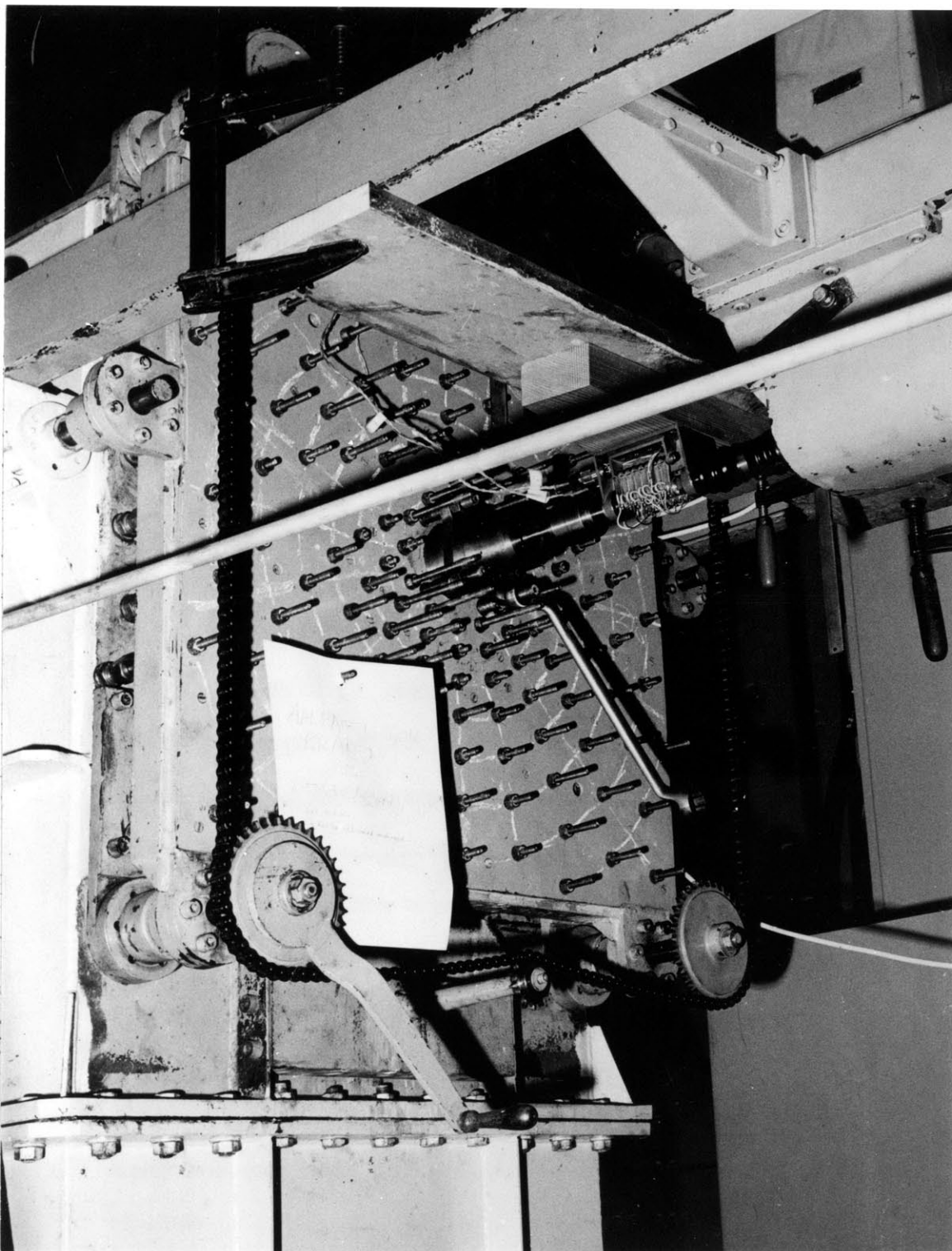


FIG. 7.2 UPSTREAM END OF TUNNEL SHOWING VELOCITY CONTROL VALVE STEMS AND SLIP RINGS

longitudinal settings of the valves. The upstream end of the tunnel with the protruding ends of the valve stems is shown in Figure 7.2. The test section used for propeller work is square in section, with dimensions 30 x 30 cm.

The existing propeller shaft system for steady measurements is enclosed within a bronze tube that passed from the motor-dynamometer through a gland at the upstream end of the tunnel and through the center of the velocity control nozzle group into the test section.

Requirements for the Design

Several general requirements for the measuring system were set up as guidelines for the design. First, the new shafting system was to fit into the tunnel without modification of the existing structure. Modification of the tunnel, especially the velocity control section, could be expected to be complicated, time consuming and expensive, and any possible future disruption of the normal tunnel functions was to be avoided. The dynamic shaft system was thus required to take the same form as the existing shaft system, namely a self-contained unit within a tube that could be easily inserted and removed.

All electrical measurements were to be performed by "off the shelf" electronic components. Neither the time nor money was available for the design and development of special electronic equipment. In general, it was desired to keep the mechanical equipment as simple as possible so that it could be built within the limited time available and at a reasonable cost.

In particular, the device was to be capable of measuring both thrust and torque variations at blade frequency with approximately the same sensitivity and accuracy. The phases of both thrust and torque were to be measured with respect to some fixed reference position of the propeller, this being considered as important as the amplitude measurements.

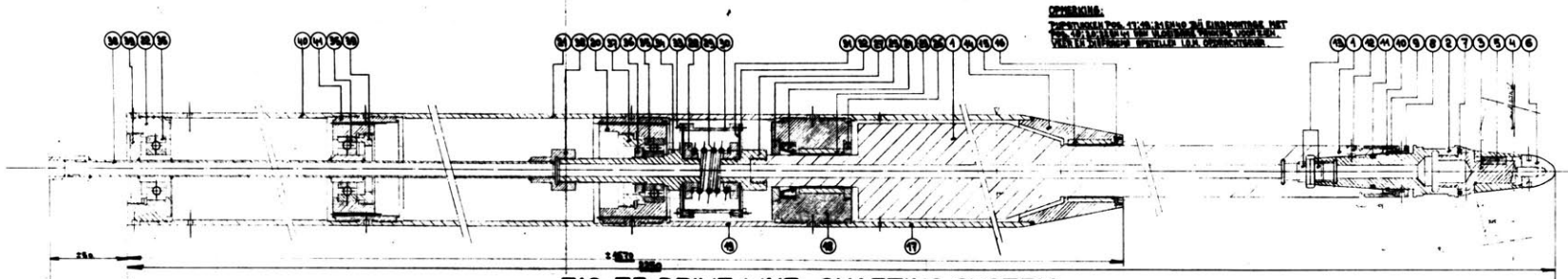
Most important, the system was to be capable of static calibration. This was required in order to avoid the complication and uncertainty associated with dynamic calibration. For static calibration to be valid the natural frequencies of vibration in both torsional and axial modes must be much greater than the measuring frequency. Dynamic calibration, necessary if the natural frequencies were of the same order as the measuring frequencies, would have to be carried out on the system when running submerged with the propeller attached. The difficulties in measuring the amplitude and phase response under these conditions are obviously very great.

Finally, it was desired to operate the propeller at the greatest possible RPM in order to attain high Reynolds number in the flow and to provide the largest possible forces, since these vary with the square of the speed.

Description of the Shaft System

The drive line of the system as built is illustrated in Fig. 7.3. A length of large diameter shaft provides a body of large mass and moment of inertia to which the propeller is

Fig. 73
Drive line-shafting system



OPMERKING:
TOEGEPAST OP: STABILISERING VAN DE RIJBAAN MET
EEN VERBODEN TOEGANG TOT DE RIJBAAN. VOOR DE
VRIJLEZING VAN DE RIJBAAN. VOOR DE
VRIJLEZING VAN DE RIJBAAN. VOOR DE
VRIJLEZING VAN DE RIJBAAN. VOOR DE

FIG. 73 DRIVE LINE-SHAFTING SYSTEM

attached by a stiff shaft. It was early found impossible to attain the necessary natural frequencies with a normal shaft system between the propeller and the motor because of its necessarily great length. The massive shaft is rotated by the motor through a long slender tube of small stiffness and is restrained in the axial direction against a ball thrust bearing by a soft spring made up of two diaphragms in series. Driven and restrained by these soft springs the shaft becomes, in effect, a free system in the torsional and axial modes at high frequencies.

Several conflicting requirements must be compromised in order to select the shaft lengths and the spring stiffnesses. High natural frequencies of the free system demand that the shafts be as short as possible and of large diameter for stiffness. It is desirable to have the propeller mass and moment of inertia, including entrained water, a small fraction of the mass of the free system in order to reduce the relative importance of the inertial reaction of the screw at the measuring frequency when the free system oscillates as a rigid body. The maximum diameter, however, is limited by the tube surrounding and supporting the shaft system, which must pass through the gland of the tunnel. Choosing the maximum possible diameter of the massive shaft, any increase in mass requires increased length at the cost of frequency.

The torsional drive and axial restraint spring must be stiff in order to limit the deflection and shaft motion under the steady propeller thrust and torque loadings. With increased spring stiffness, increased mass is required to maintain the low natural frequencies of oscillation of the shaft against the motor and the thrust bearing.

The final compromise arrived at provides the following computed natural frequencies:

| | Torsional | Axial |
|-------------------------|-----------|-------|
| Low Frequency, cps: | 10 | 10 |
| High Frequency, cps: | 870 | 1750 |
| Propeller mass, % total | 3.7 | 3.0 |

The measuring frequency chosen was 100 cps maximum, providing roughly an order of magnitude to the nearest natural frequencies in both directions. The choice of this measuring frequency was also influenced by certain characteristics of the electronic instrumentation. The mass and moment of inertia of the entrained water of the screw were estimated from data given by Lewis (33) and Visser (34). The screw considered was unfortunately rather heavy, being made of bronze.

The natural frequencies of the shaft and propeller were carefully investigated. Computations were based on the solution of the differential equation for the vibration of uniform shafts applied piecewise according to a scheme of F. M. Lewis. These were carried out in detail for many design variations and are

believed to be accurate. Unfortunately no experimental verification of the natural frequencies was made.

The length of the smaller diameter shaft section is minimized by locating the propeller at a distance of two diameters from the plane of the nozzle outlets, the location of the inboard end of the large shaft being fixed by the convergence of the nozzles. The diameter of this section is made as large as possible while maintaining a radial clearance through the center of the nozzle group. This shaft section runs uncovered and without support, being essentially a cantilevered extension of the large shaft.

The diaphragm arrangement, which is stiff in torsion and soft axially, in conjunction with a torque tube beyond the thrust bearing, was chosen instead of a simple coil spring in order to prevent any possible coupling between axial and torsional motion. The separate arrangement also allowed freedom in choosing the stiffnesses in the two directions. Because of the restricted diameter, two diaphragms in series were needed in order to get sufficiently low stiffness with a reasonable thickness and stress in the diaphragm material. Stresses at full propeller load were kept to acceptable levels by the introduction of an internal compression spring between the diaphragms that applied an outward preload approximately equal to half the expected compressive load.

The shaft runs submerged in its tube, supported by two water lubricated plastic bearings at the ends of the large diameter section. Water is excluded from the outer end of the shaft tube by a rubber seal on the shaft journal just outboard of the bearing. This seal is very soft and provides no appreciable axial restraint.

Outside the tunnel, between the end of the shaft tube and the drive motor, a set of eight slip rings is interposed in the shaft line. Wires running to and from the dynamometer at the opposite end pass through the shaft which is bored for that purpose. This sets another restriction on the length of the shaft.

The Dynamometer

The dynamometer is situated directly adjacent to the propeller. It consists of a short self-contained, removable, piece of shafting instrumented with strain gages. The interior is bored out leaving a stressed element in the form of an annulus with a thickness nominally of 0.3 mm on a diameter of 26.0 mm. The strain gages are cemented on the outer surface with their sensitive elements directly over the thinned section. The axial length of the stressed section is but 6 mm, just sufficient to enclose the lengths of the strain gage elements. With this very short length, even though thin, the dynamometer has very great stiffness, both axially and torsionally, and its effect on the natural frequencies is very small. This is in contrast to the usual sensitivity *vrs.* natural frequency contest that appears in dynamic instrumentation problems.

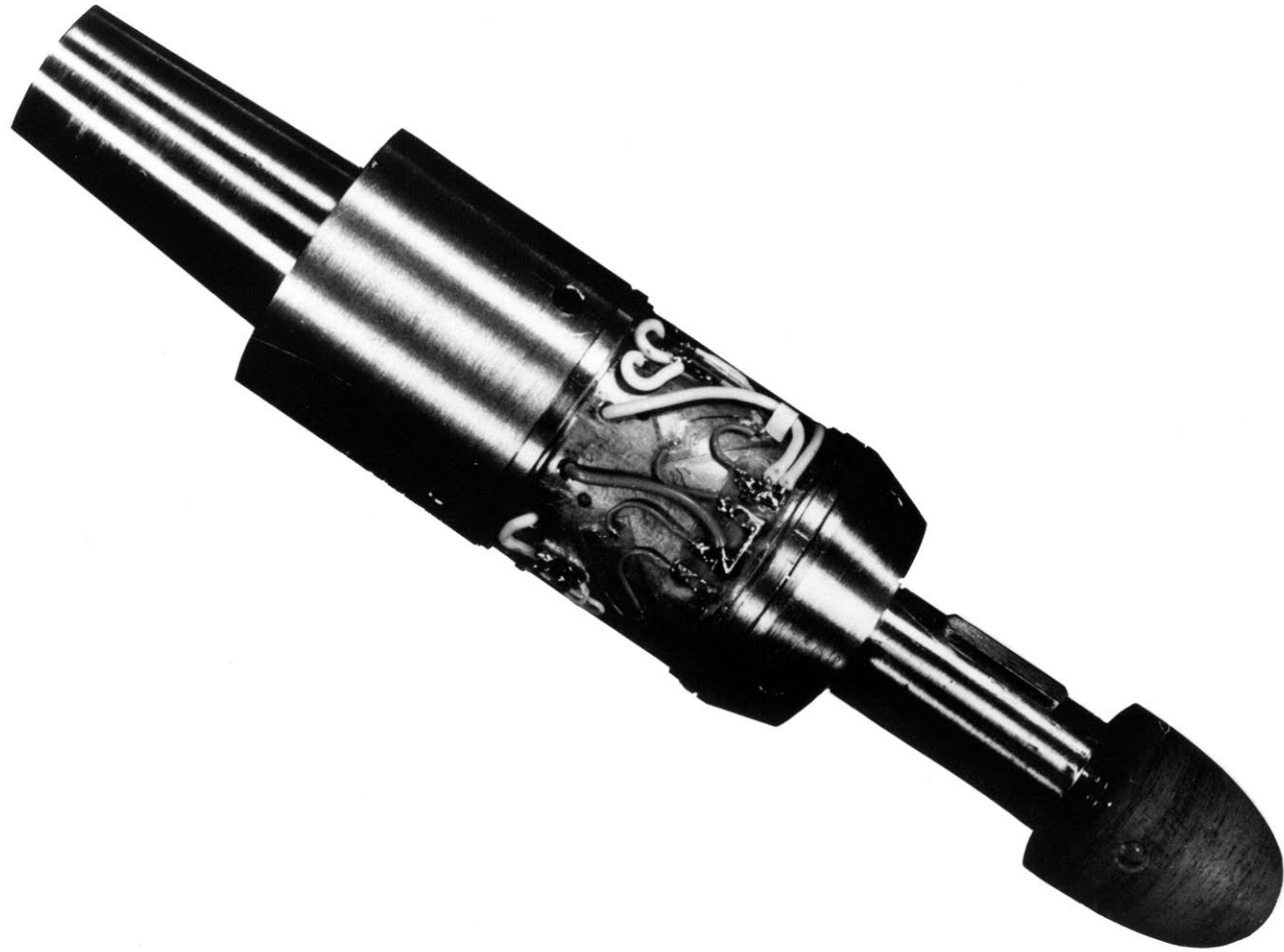


FIG. 7.4 DYNAMOMETER

The gages used are of the piezoresistive type with gage factors of 125. Four gages are installed at 45° to the axis forming a full bridge for torque measurement. For the thrust measurement double gages, each containing one element with a positive gage factor and one with a negative factor are employed. Only two of these gages are needed and these are placed parallel to the axis and on opposite sides of the piece. The positive and negative elements are wired in a full bridge arrangement with four active legs. With these arrangements, the torque and thrust bridges are compensated for temperature effects, to which these gages are particularly sensitive, and are arranged to cancel effects of bending and side force..

The dynamometer with the gages installed is shown in Fig. 7.4. The gages and external leads are waterproofed by the careful application of a soft rubber-like compound. The dynamometer is fitted to the shaft by a taper and drawn tight by a threaded collar. An eight pin plug at the end of the taper mates with a receptacle in the shaft for the electrical connections. The plug is aligned by a pin sliding in a keyway in the taper and the connections are sealed watertight by an "O" ring.

Electronics Instrumentation

The primary electronic instruments used are a pair of Peekel strain indicators, one each for thrust and torque. These are self-contained units which supply a regulated carrier at 1000 cps and 4 volts and contain amplifiers and demodulators which deliver an output signal of nominally 0.5V for full scale on any of 4 scale ranges.

The frequency response of these components as specified by the manufacturer shows an amplitude characteristic which is perfectly flat to 100 cps with a very rapid fall off thereafter. Because of this characteristic, the maximum measuring frequency was chosen to be 100 cps. The instrument characteristic is taken advantage of to produce, in effect, a low pass filter which bars high frequency noise and the effects of high harmonics of the flow field which might be amplified by the dynamics of the shaft system.

The phase response of the strain indicators was not specified. This was determined by measuring the time lag between the output of two strain gages mounted on a flexure being bent by a vibrator at 100 cps. One strain gage was excited and detected by the strain indicator under test while the other was excited with direct current. The outputs of both were displayed simultaneously on a dual beam oscilloscope and the time lag read directly. The time lag is assumed constant for frequencies in the neighborhood of 100 cps and the phase angles determined according to the actual measuring frequency. The following gives the pertinent data for the sensitivities and time delays of the combined strain gages and electronics:

| | Channel #1 | Channel #2 |
|---|--------------------------|-----------------------|
| | Torque | Thrust |
| Time delay @ 100 cps, sec. | 3.0×10^{-3} | 2.7×10^{-3} |
| Equivalent phase angle @ 100 cps, deg. | -108 | -97 |
| Strain indicator output, V/ $\mu\epsilon$ | 0.52×10^{-3} | 0.53×10^{-3} |
| Apparent dynamometer sensitivity | | |
| (based on gage factor of 2) | 420 $\mu\epsilon$ /kg-cm | 420 $\mu\epsilon$ /kg |
| Overall sensitivity | 0.219 V/kg-cm | 0.219 V/kg |

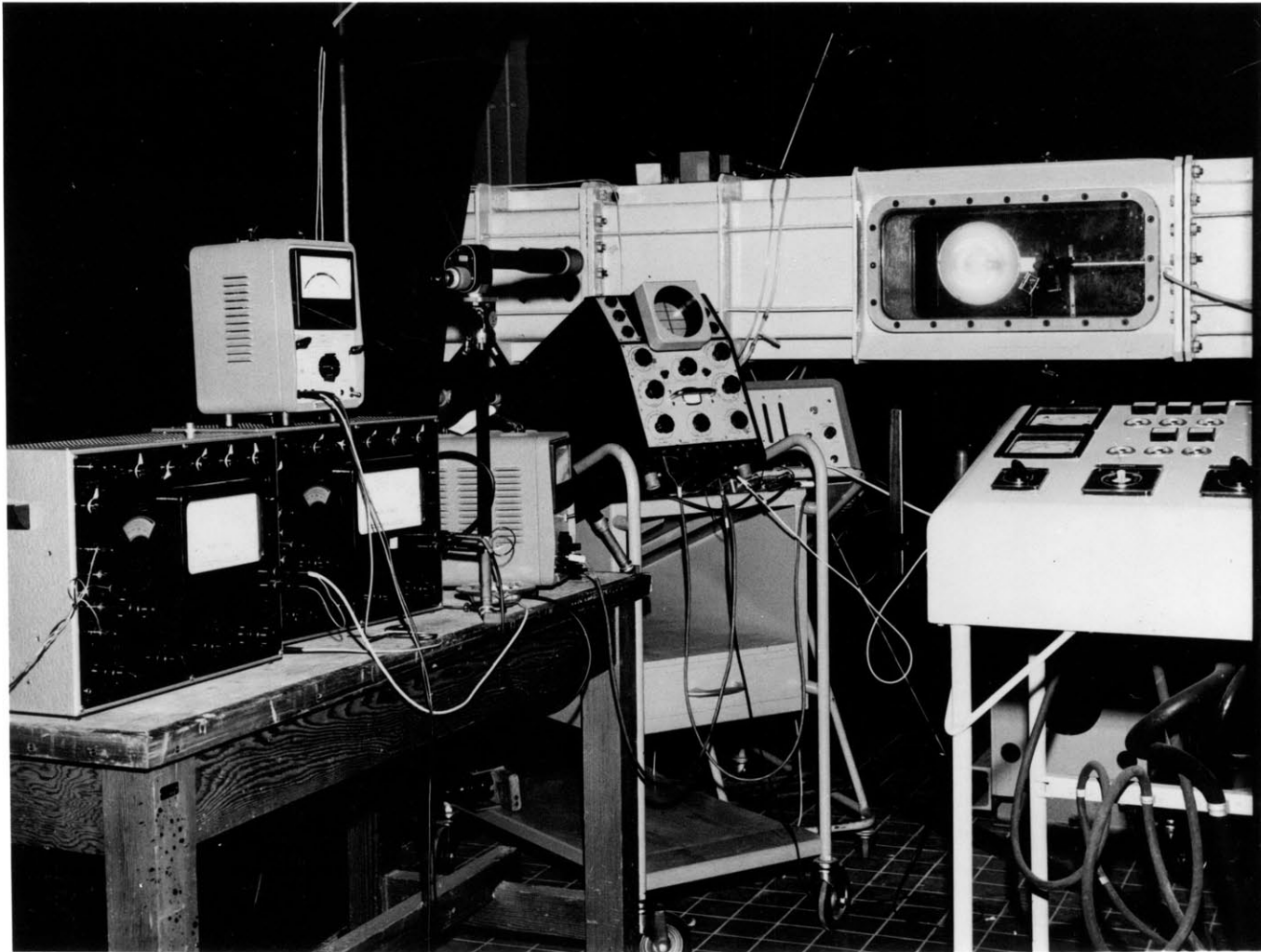


FIG. 7.5 GENERAL VIEW OF INSTRUMENTATION

The dynamometer sensitivities are the averages of the results of all the calibrations carried out during the period of the experiments. The variations were less than 10 in these numbers. Though it was desired to make the thrust and torque sensitivities nearly equal by proper sizing of the sensitive element, the exact equality seen above is coincidental.

The output signals of the strain indicators are displayed on an oscilloscope one at a time and the RMS amplitudes measured by a parallel connected alternating current vacuum tube voltmeter. A direct current VTVM is used to calibrate the strain indicators, determining the output voltage per micro-strain. An electronic counter is used to display the propeller speed in revolutions per second. Figure 7.5 shows the general view of the instrumentation.

Measurement of Phase

Phase angle measurement is accomplished by intensity modulation marking of the oscilloscope trace. The intensity modulation is controlled by pulses from a pair of photocells which are activated by light beams passed through a small hole in a rotating disk. This disk is geared to the drive motor with a step up ratio equal to the number of propeller blades. The disk thus rotates at "blade rate". The photocells and their light sources are carried by a wheel concentric with the disk axis which is rotated by hand through a flexible cable and gear until the bright spots caused by the photocell pulses are located symmetrically about the positive peaks of the sine waves of the thrust or torque

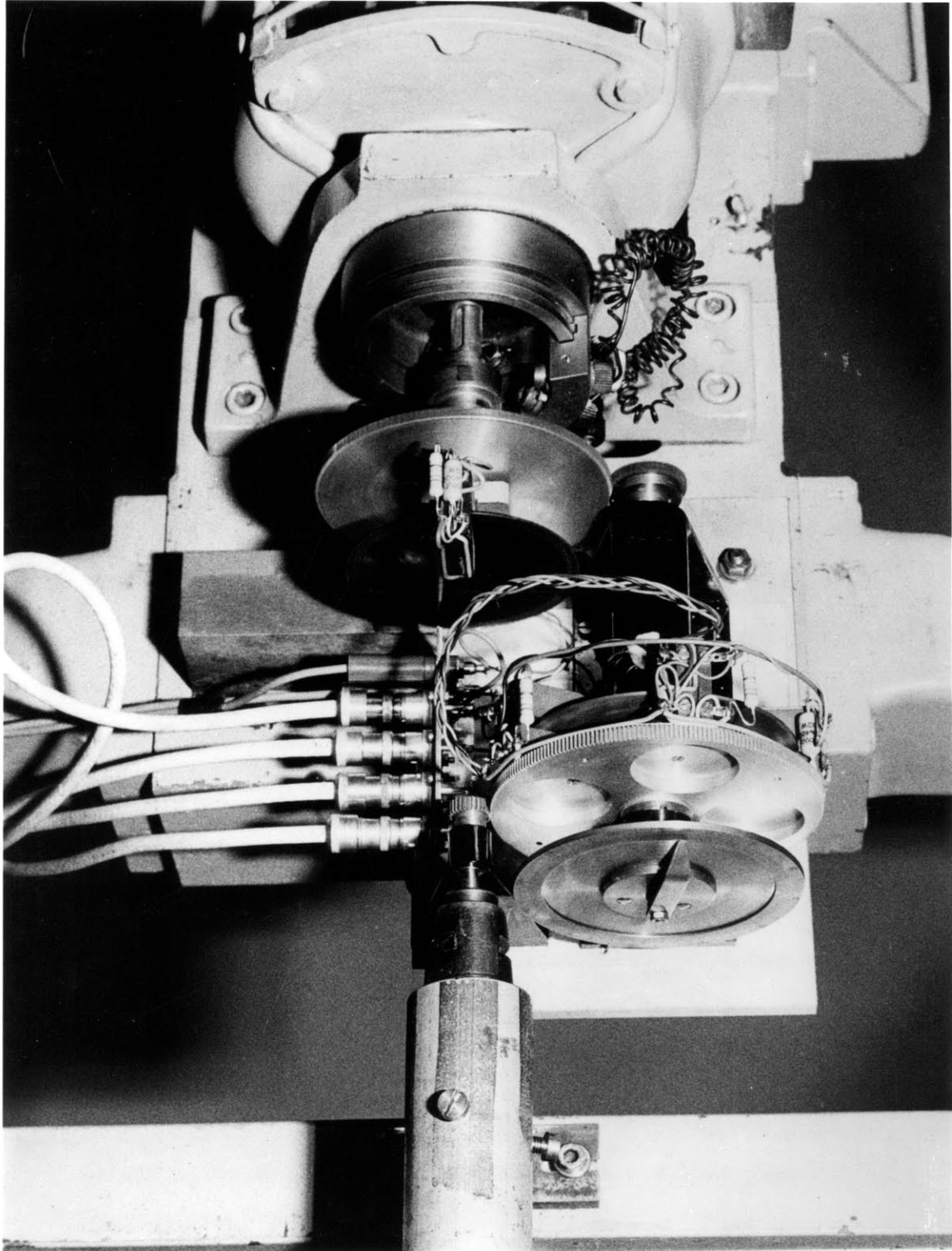


FIG. 7.6 INTENSITY MODULATION CONTROL
DEVICE FOR PHASE ANGLE MEASUREMENT

signal on the oscilloscope. The photocells are placed 150 degrees apart on the wheel so that the observer can distinguish the positive from the negative peaks. The procedure is easily implemented by bringing the bright spots into a single horizontal line on the scope. Due to the 150 degree spacing of the spots they appear along a line located above the mean when in phase with the positive signal.

The angle of the photocell carrier wheel is then read off an angular scale. Since the disk is rotating at blade rate, the scale provides 360° per blade space. The scale can be easily read to one degree, making quite precise phase angle measurements possible. The device described above is shown in Fig. 7.6.

The measured angles must be related to angular propeller position relative to some fixed reference in the tunnel. The zero reference is taken arbitrarily as a horizontal plane including the shaft axis. The plane is located by scratch marks on the side windows of the tunnel test section. The blades of the propeller model were marked near their tips with engraved lines at ninety degree intervals measured from a prescribed reference on one blade; in this case a radial line through the midchord at the 0.7 radius.

The zero angle is then established optically by illuminating the rotating propeller with a strobe light while observing the marks on the blade tips through a telescope. The strobe light is tripped by a third photocell on the carrier wheel

positioned to bisect the angle between the other two. The telescope is set up so that a hairline in the eyepiece coincides with the reference marks on both the front and back windows of the test section. Peering through the telescope the photocell wheel is rotated until the blade tip marks coincides with the hairline and then the angle scale is slid round till the pointer indicates zero. The telescope and strobe light can be seen in Fig. 7.5.

It is necessary to carry out this zeroing procedure for each propeller operating condition because of the changes in the twist of the shaft drive tube with changes in load. The procedure provides a reasonably accurate zero angle, since non-alignment of the tip marks of ± 0.5 mm can be easily detected, resulting, for a propeller diameter of 150 mm, in a blade space zero angle error of only ± 1.5 degrees.

Velocity Field

It was desired to create an axial velocity field consisting of a uniform stream plus a blade order harmonic perturbation. Ideally, the perturbation was to be constant with radius in both amplitude and phase. Harmonic content of numbers other than the blade number, in this case four, was to be minimized in order to avoid transverse and bending loads on the propeller and higher harmonics of the blade frequency thrust and torque.

In developing the flow field, the velocities were measured with a pitot tube rake connected to a bank of manometers. The rake enters the test section from the downstream end of the tunnel and is turned by hand about an axis concentric with that of the shaft. The angle of the rake is measured in degrees on a scale at the outboard end. There are pitot static tubes arrayed along the arms of the rake at radii corresponding to the middle and edges of the annularly arranged flow nozzles.

The rake was calibrated by towing it submerged in the Towing Tank at known velocity with the manometer board riding the carriage. The resulting calibration showed a large variation between tubes of the velocity constant, presumably due to the interference of the thick arms of the rake.

Because of the large non-uniformity in the calibration constants of the tubes, they were employed in the tunnel as impact or true pitot tubes. A static reference pressure common to all tubes was taken from four parallel connected static taps in the tunnel windows at the plane of measurement. The static pressures measured by the pitot tubes were disregarded. This provided a large reduction in the amount of labor and time required to read the manometers and reduce the data. A subsequent check comparing the velocity field measured with the original and final arrangements showed good agreement except at the innermost radius, presumably due to the presence of potential flow about the dummy propeller hub and shaft end.

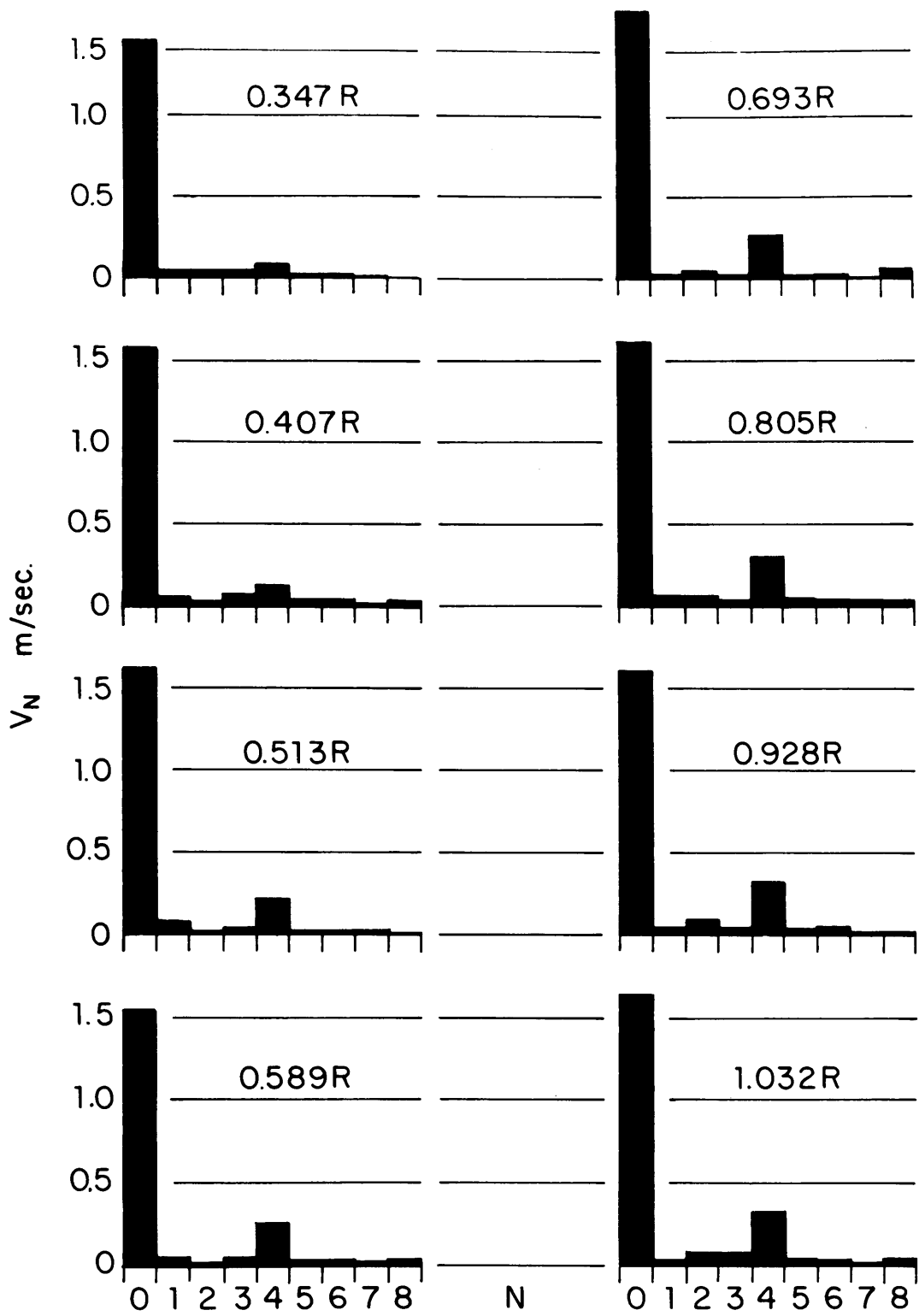


FIG. 7.7 AXIAL VELOCITY FIELD- HARMONIC COMPONENTS.
 IMPELLER RPM: 420

When a satisfactory velocity distribution had been attained, the complete field was measured at all radii at ten degree intervals for five different impeller speeds; and the pressure drop across the nozzles recorded as a measure of the corresponding mean velocities. Finally, the zero angles for the individual pitot tubes were obtained by sighting the impact hole of each with the telescope aligned in the reference plane.

The velocity field data recorded were subjected to harmonic analysis. The amplitude and phase of the velocity distribution at each measuring radius were obtained for harmonic numbers from zero to eight. These were computed by application of trapezoidal rule integration with the ten degree spacing of the data. The analysis was carried out for each of the five basic speeds.

The in phase and out of phase components of each harmonic were each expressed in a fifth order polynomial in the radius by least square fitting. The polynomials were used to interpolate for the values at evenly spaced radii for use in computations for the propeller. The harmonic analysis of the field at the measuring radii for an impeller speed of 420 RPM is shown in Figure 7.7. Note that the fourth harmonic remains roughly constant over the outer radii at approximately twenty percent of the mean velocity.

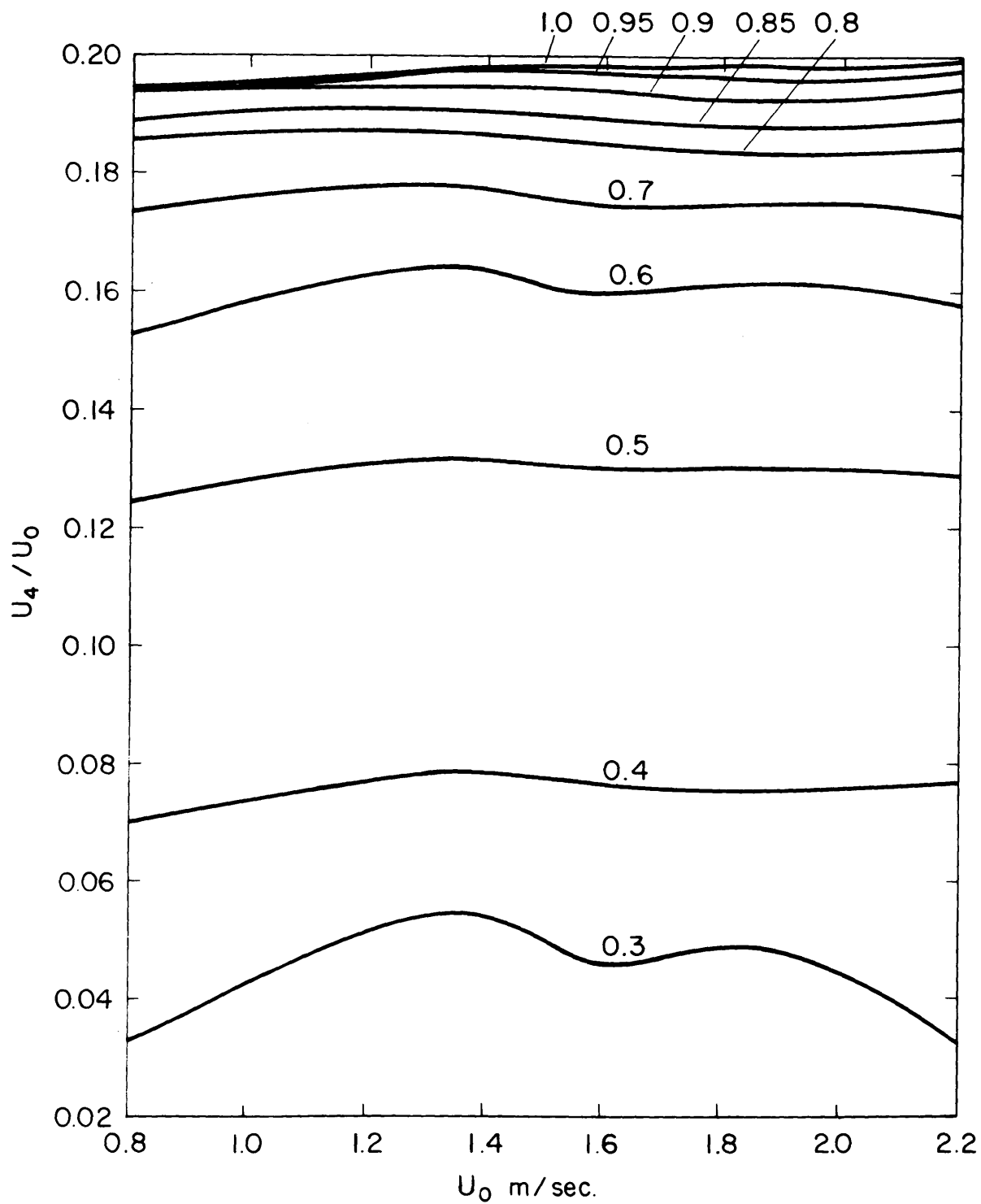


FIG. 7.8 AXIAL VELOCITY FIELD FOURTH HARMONIC AMPLITUDE.
 FIGURES ON CURVES ARE FRACTIONS OF PROPELLER
 RADIUS

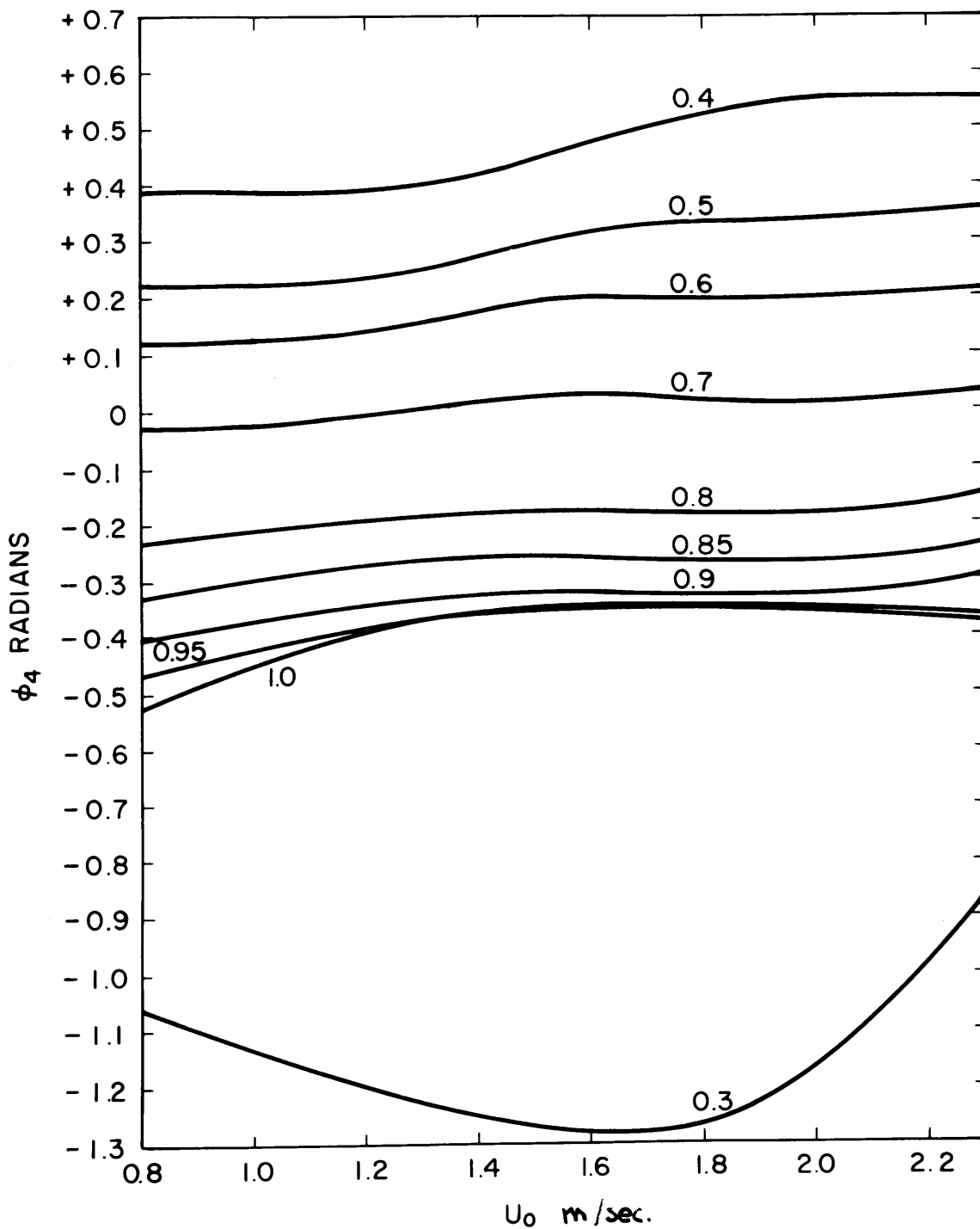


FIG. 7.9 AXIAL VELOCITY FIELD FOURTH HARMONIC PHASE ANGLE
 VRS. MEAN VELOCITY. FIGURES ON CURVES ARE FRACTIONS
 OF PROPELLER RADIUS

The mean velocity corresponding to each impeller speed case was taken as the volume mean of the zero order velocity as determined by appropriate integration of the polynomial between 30% and 110% of the propeller radius. The fourth harmonic velocity at each radius was then expressed as a fraction of this mean free stream velocity. This amplitude fraction and the associated phase angle for the various fractions of the propeller radius are shown plotted in Figures 7.8 and 7.9 **vrs.** the mean velocity. The mean velocities were finally correlated with the observed pressure drop across the flow nozzles according to the square law.

Conduct of the Experiments and Results

The propeller used in the experiments is shown in Fig. 7.10. This is essentially a constant pitch four blade B series propeller with the following characteristics:

| | |
|--------------------------|--------|
| Expanded Area Ratio, EAR | 0.59 |
| Pitch Ratio, P/D | 0.612 |
| Diameter | 150 mm |

The dynamometer was calibrated in place both before and after each run by applying known axial and torsional loads to the propeller spindle. This was done with the dynamometer submerged and the water temperature noted. Although there was considerable zero drift apparent during calibration, the sensitivity was found to vary little with temperature. The strain indicators were also calibrated for output voltage after warmup and after the runs, but before dynamometer calibration.

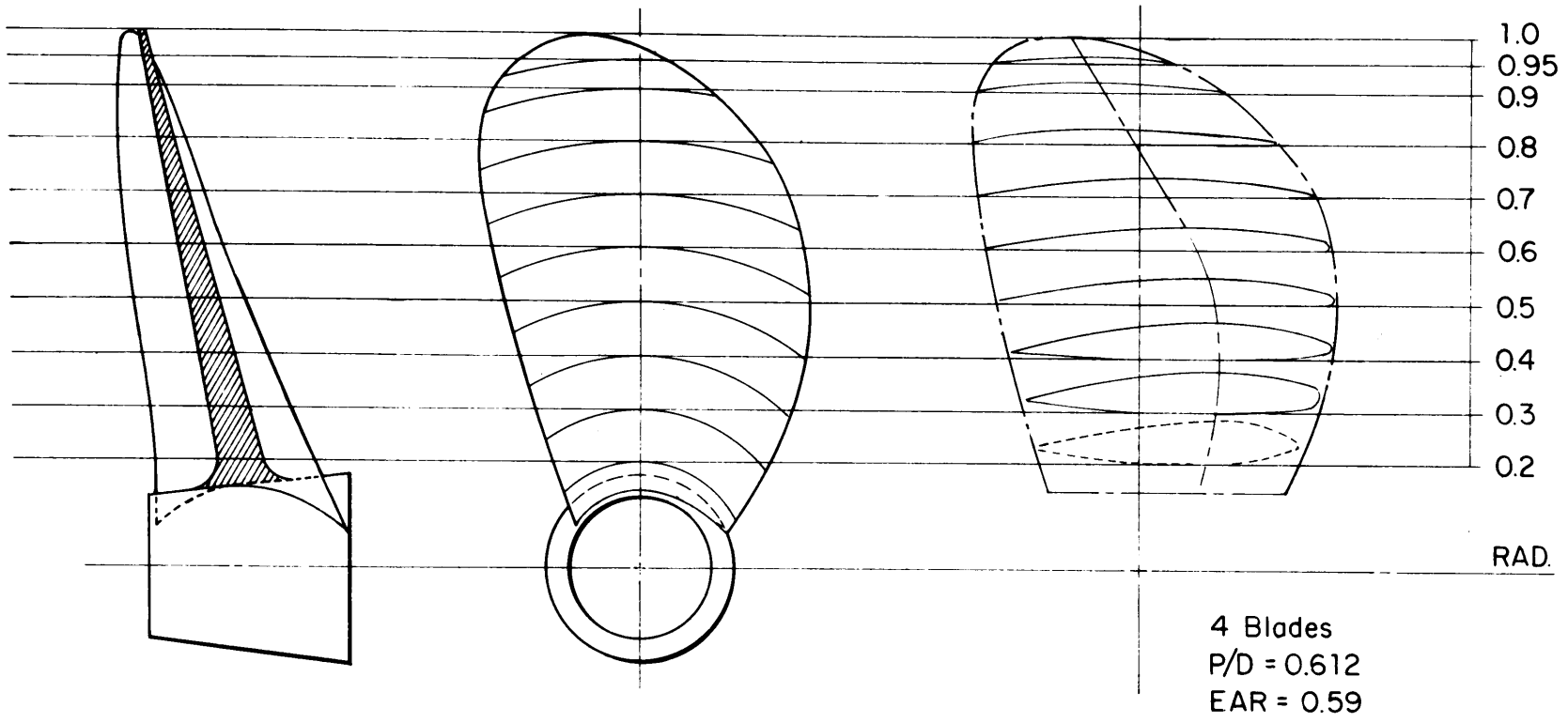


FIG. 7.10 B-SERIES TYPE SCREW

The quantities recorded during the runs were the thrust and torque RMS voltages and phase angles as described, the pressure drop across the nozzles, the water temperature, and the screw RPM.

Unfortunately, time allowed but one propeller to be tested, but runs were made at 100 and 90 cps measuring frequency corresponding to 1500 and 1350 RPM in order to verify the form of the dimensionless thrust and torque coefficient used. In each case, the propeller RPM was held constant while data was taken at different water velocities corresponding to variations in advance coefficient and hence steady propeller loading.

The reduced results of the experiments are shown in Figure 7.11. No significant systematic differences between the results at the two RPM's are apparent. In general, the thrust and torque signals displayed on the oscilloscope had the appearance of quite pure sinusoids without high frequency noise. This is presumably attributable to the low pass characteristic of the strain indicators and the mechanical isolation of the shaft from the tunnel structure at high frequencies.

Several minor difficulties were encountered, however. Setting the zero for the phase angles proved inconvenient due to difficulty in distinguishing the blade tip marks through the telescope. This can easily be remedied with a telescope more suited to the task; the one used was of the ordinary terrestrial type fitted with an extension tube to permit closer focusing.

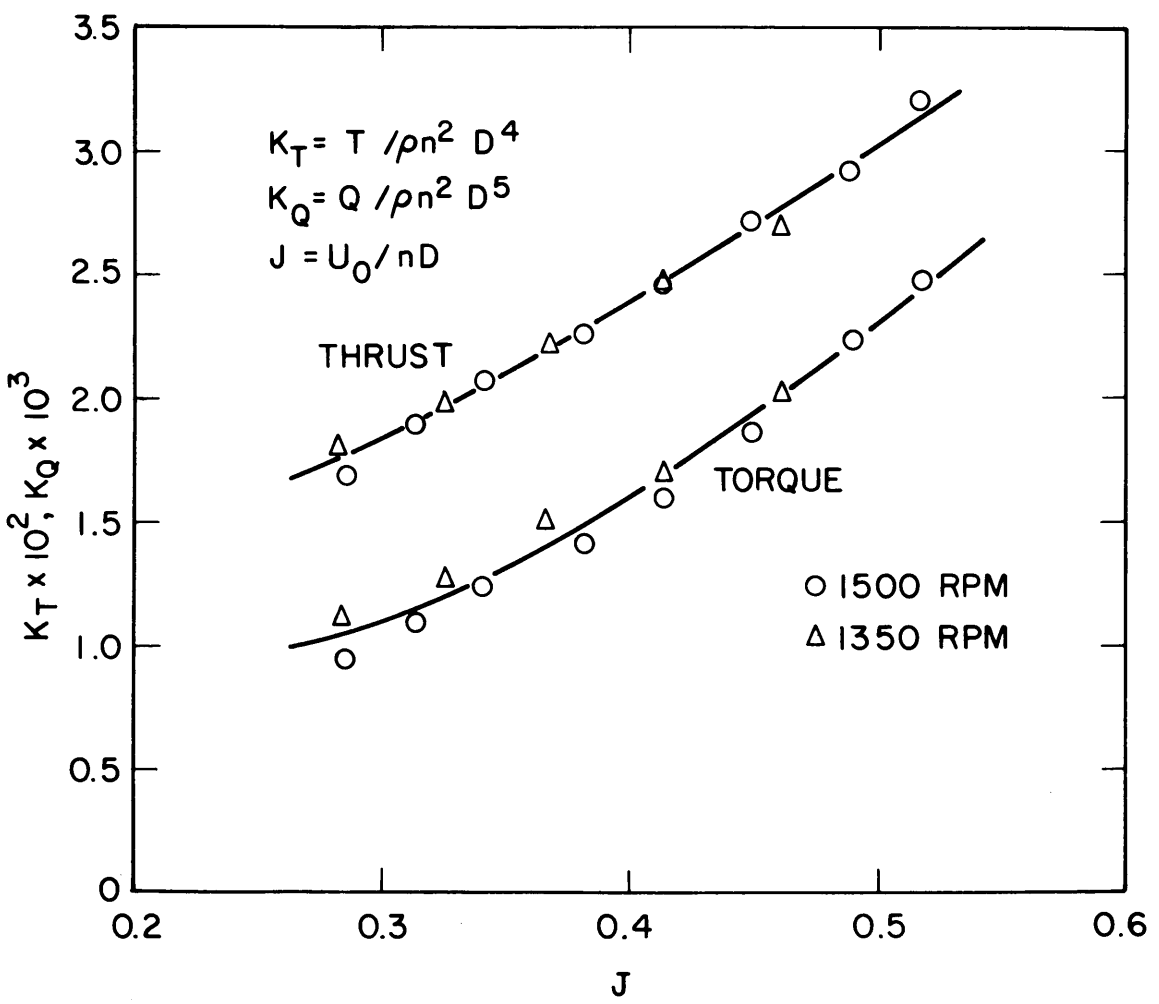
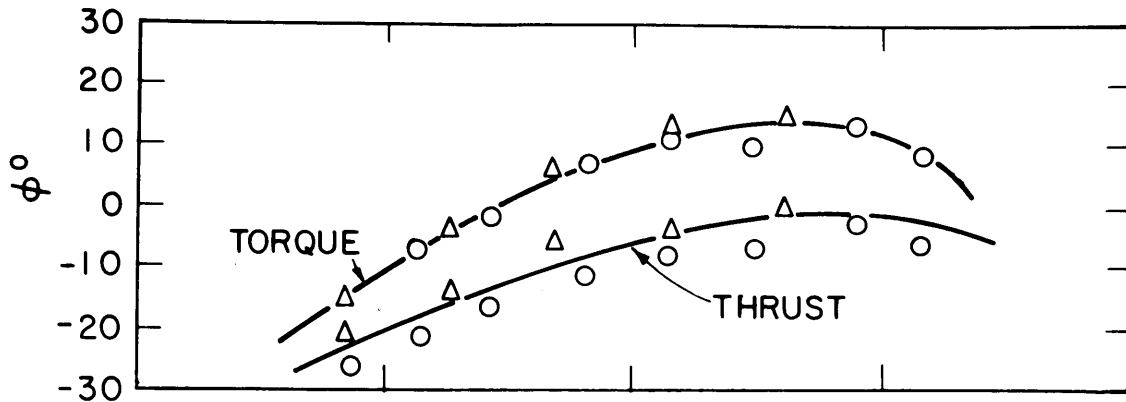


FIG. 7.II EXPERIMENTAL RESULTS - BLADE FREQUENCY THRUST AND TORQUE

At times, a low frequency irregular disturbance was added to both the thrust and torque signals. This was not a modulation of the signals and was definitely proved to be other than a once per revolution effect, but its frequency could not be further identified. It has been suggested that this disturbance is caused by periodic tunnel pressure variations. This occasionally caused difficulty in setting up the phase indication due to the dancing of the signals and also caused the needle of the VTVM giving the amplitudes to swing over an arc.

With low water velocity and advance coefficient and thus high thrust, a distortion of the signals became apparent due to the presence of higher harmonics. This was presumed due to the bottoming of the axial coil spring between the diaphragms with large thrust load and the consequent lowering of the axial natural frequency.

CHAPTER VIII

RESULTS AND CONCLUSIONS

Computational Arrangements

The proposed analysis has been programmed for electronic digital computation. The programs have been written in a general manner which allows either the unsteady strip theory or the low harmonic number analysis to be used in any particular case as well as the three dimensional model.

For the latter case, the harmonic analysis of the sum functions is necessary and the scheme used may be of interest. The Gauss five point integration rule (29) is used with a basic arrangement of two five point intervals in the angle between adjacent blades. In order to deal accurately with the sum functions where they are sharply peaked at or near $\psi = 0$ the first basic interval is subdivided geometrically. This interval is successively halved according to the following schedule:

| No. of blades, K | No. times 1st interval halved |
|------------------|-------------------------------|
| 1 to 3 | 5 |
| 4 to 7 | 4 |
| 8 to 15 | 3 |

The last interval is also halved once. Typically, for a four-bladed propeller this scheme yields thirteen intervals or sixty-five points available for the harmonic analysis. The sum functions must be evaluated at each of these points.

In all the computations in this chapter a five term Birnbaum series for the radial circulation distribution has been used. The effect of variations in the number of terms used has not been investigated. The contribution to the downwash difference of the bound radial vortex lines is neglected for simplicity since it is expected to be small for the four bladed propeller considered. In computations using the three-dimensional analysis, the sum functions are evaluated in all cases by summing five terms in the series before entering the Euler-Maclaurin formulas.

The computer programs allow a maximum of twenty panels over the propeller radius, but sixteen have been used in most cases in the interest of saving computer time, since that increases roughly with the square of the number of panels. The effect of the number of panels used or the panel size has been investigated by computing the same propeller and inflow case with both sixteen and eight panels. The overall results have been found essentially the same except at high harmonic numbers where the results of the eight panel model behave erratically. It is supposed that this coarse spacing results in an inaccurate representation because the panel widths are no longer sufficiently small in comparison to the disturbance wavelength for large N .

For the zeroth harmonic approximation to the downwash difference the steady flow induced velocities are computed by a proven standard formulation of Wrench (35). The steady propeller thrust and radial circulation distribution so computed are in

close agreement with the results of the three-dimensional unsteady analysis at $N = 0$. Since the radial circulation distribution in both these methods is represented in the same way, namely by a five term series, the coefficients of which are determined by least square solution of equations (4.11), some independent check is desirable. The circulation distribution has, therefore, been calculated approximately by the application of the zero hub Goldstein functions for the optimum propeller (31). Comparison of the circulation distributions shows no important differences.

A Modification of the Model

In the process of numerically testing the analysis, it became apparent that the results were somewhat sensitive to the angular position of the reference line relative to the blade. This was aside from the obvious phase shifts introduced. This behavior was considered unacceptable and the following modification has been made to insure the independence of the result from the reference line position.

The phase of the induced velocity at any radius is adjusted to take account of the angular shift between the trailing edge at that radius and the position of the reference line. In the modified arrangement, the induced velocity is evaluated on the radial vortex line as if it passed through the trailing edge at the radius in question. This insures that at that radius the vorticity shed

from the trailing edge is in the proper phase relationship to the circulation. This is only approximately true for the sections at other radii because of the generally non-radial trailing edge shape. If the reference line is now moved off the trailing edge, we must insure that the induced velocity at the trailing edge remains unchanged, because in reality it has nothing to do with the position of the arbitrary reference line.

If the reference line is moved forward on the blade, the induced velocity on it must lead that at the trailing edge by the angle $k^* s_{\Gamma}$, still assuming the induced velocity is sinusoidally distributed chordwise. This may be written:

$$\bar{w}(0) = \bar{w}(s_{\Gamma}) e^{i k^* s_{\Gamma}} \quad (8.1)$$

where $\bar{w}(0)$ is the induced velocity at the reference line, wherever it may be, and $\bar{w}(s_{\Gamma})$ is the induced velocity as it has been computed before this modification. The coordinate of the trailing edge s_{Γ} is dimensionless on the basis of the semichord length at the radius in question and is given simply by:

$$s_{\Gamma} = 1 + s_m \quad (8.2)$$

in terms of the midchord coordinate used in the skew correction (4.18). This phase shift is applied at each radius where the downwash difference is evaluated.

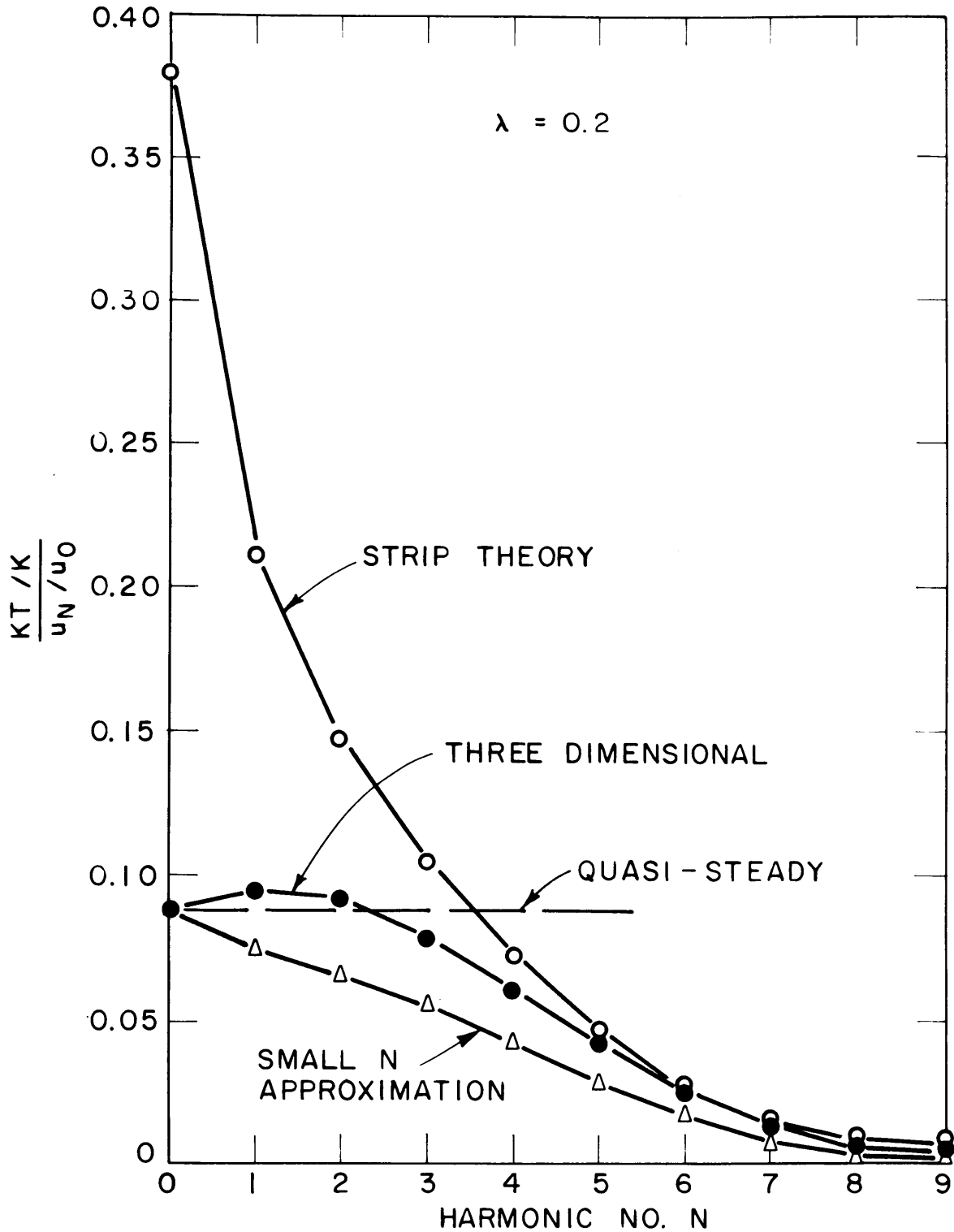


FIG. 8.1 COMPUTED BLADE THRUST AMPLITUDE FOR PROPELLER WITH 0.59 EXPANDED AREA RATIO

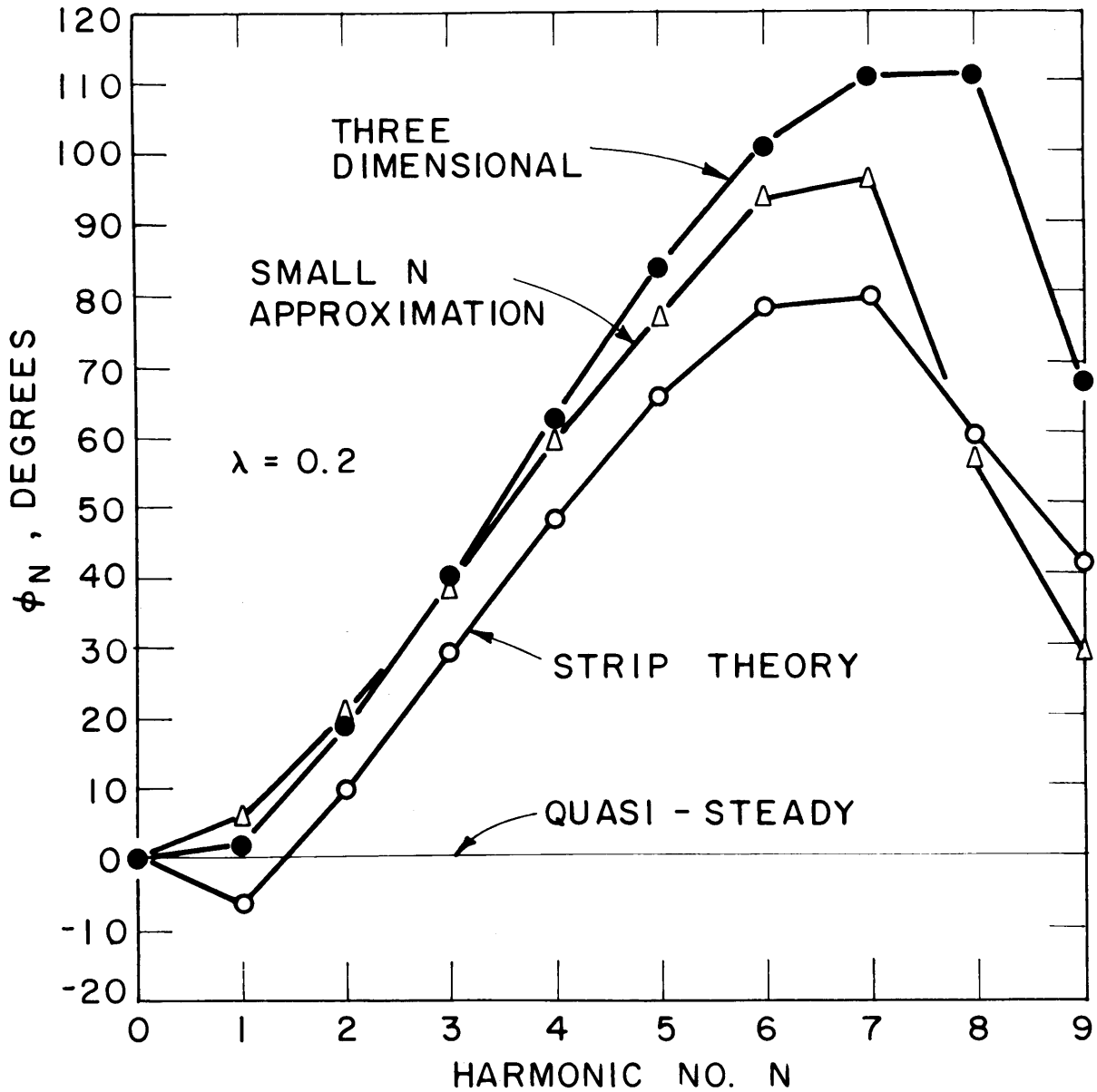


FIG. 8.2 COMPUTED BLADE THRUST PHASE FOR PROPELLER WITH 0.59 EXPANDED AREA RATIO

Analysis of Some Results

A set of calculations has been made for the purpose of comparing the predictions of the strip theory, low harmonic number approximation and the proposed three-dimensional analysis. The propeller used in the experiments of Chapter VII, shown in Fig. 7.10, has been used in these calculations. Axial inflow perturbations with constant amplitudes and zero phase over the radius and of various harmonic numbers are used in all cases. All results are linear with the amplitude of these perturbations.

The strip theory results are those obtained by requiring the downwash difference matrix of (4.11) to be zero. The radial circulation distributions obtained by this means are not purely stripwise since they are fitted in a least square sense to a series by the solution of the simultaneous equations. The radial lift distribution, however, is determined independently of the circulation in a stripwise manner.

The thrust per blade and its phase angle as computed by the three methods are shown in Figures 8.1 and 8.2 for various harmonic numbers. It is immediately obvious that the strip theory is very much in error for $N = 0$. Here the three dimensional analysis and the low harmonic number approximation agree and both represent the steady flow lifting line model.

With increase in the harmonic number, the strip theory result decreases rapidly while the three dimensional thrust first increases slightly from its initially lower value and then decreases.

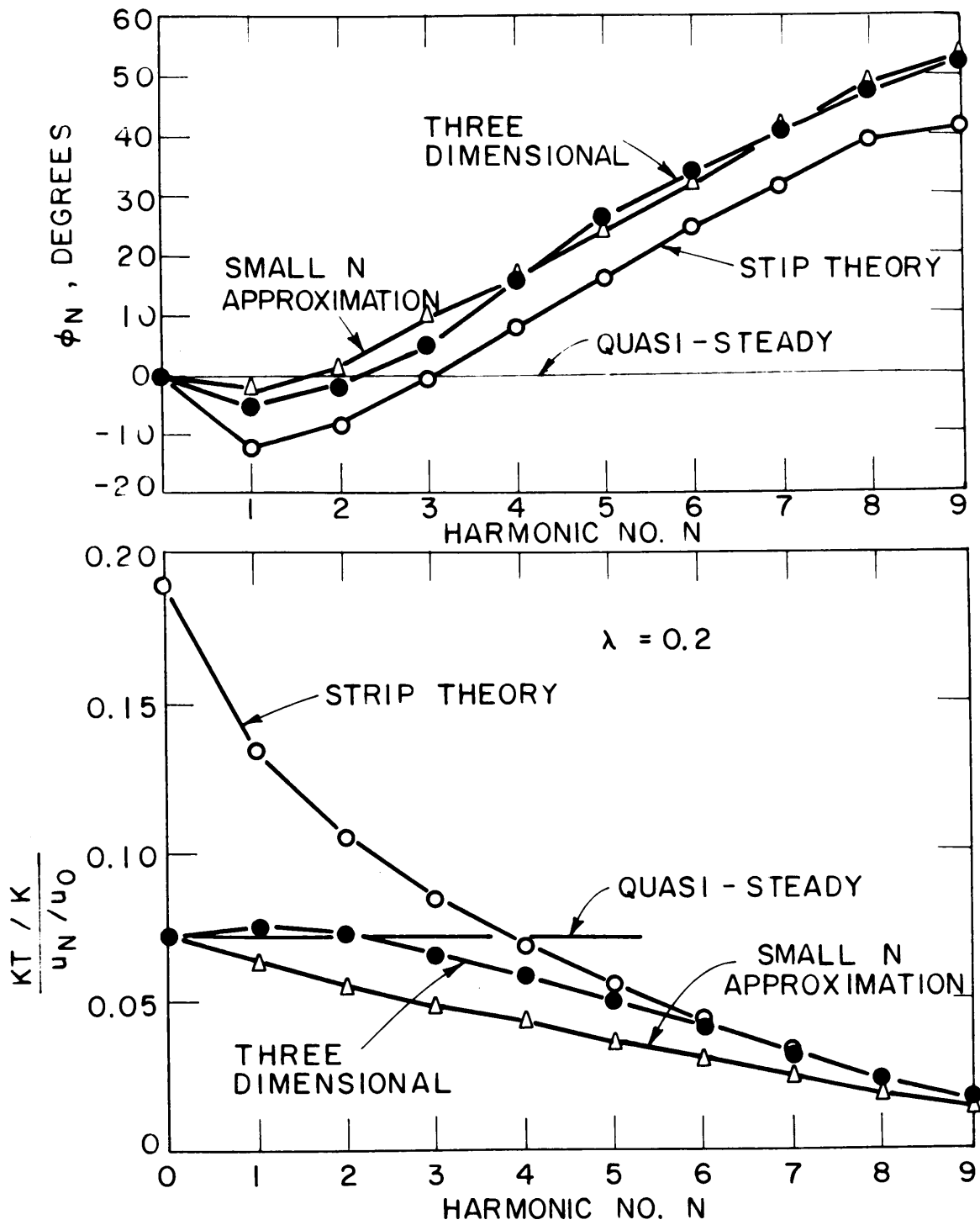


FIG. 8.3 COMPUTED BLADE THRUST FOR PROPELLER WITH 0.295 EXPANDED AREA RATIO

The $N = 0$ approximation results in a steadily decreasing thrust with increase in N .

For high harmonic numbers, the strip theory and three-dimensional analysis tend to converge in amplitude, but maintain a nearly linearly increasing phase difference. The $N = 0$ approximation is in closer phase agreement with the 3D analysis, but the amplitude, though converging, remains low over the entire range of N .

The convergent behavior of the strip theory and the three-dimensional analyses is seen to be reasonable in light of the variation of the circulation with the reduced frequency. Inspection of Figure 4.3 shows that the circulation amplitude decreases sharply with frequency. Regarding equation (4.11), it is seen that the strip theory term, represented by f_{nj}/\bar{G}_j , then increases in magnitude with N , thereby rendering the downwash difference relatively unimportant. The same can be said for the $N = 0$ approximation, but since the downwash difference is overestimated by the zero order approximation, the resulting thrust value is further lowered. The thrust values predicted by the strip and 3D analyses are in good agreement in amplitude for $N = 5$ or greater.

The radial variation of the reduced frequency of this propeller is shown in Figure 8.3 for the λ value used.

In order to demonstrate the behavior with blade area or aspect ratio, another set of calculations have been made for this propeller with the chord lengths halved. The skew line is kept the same.

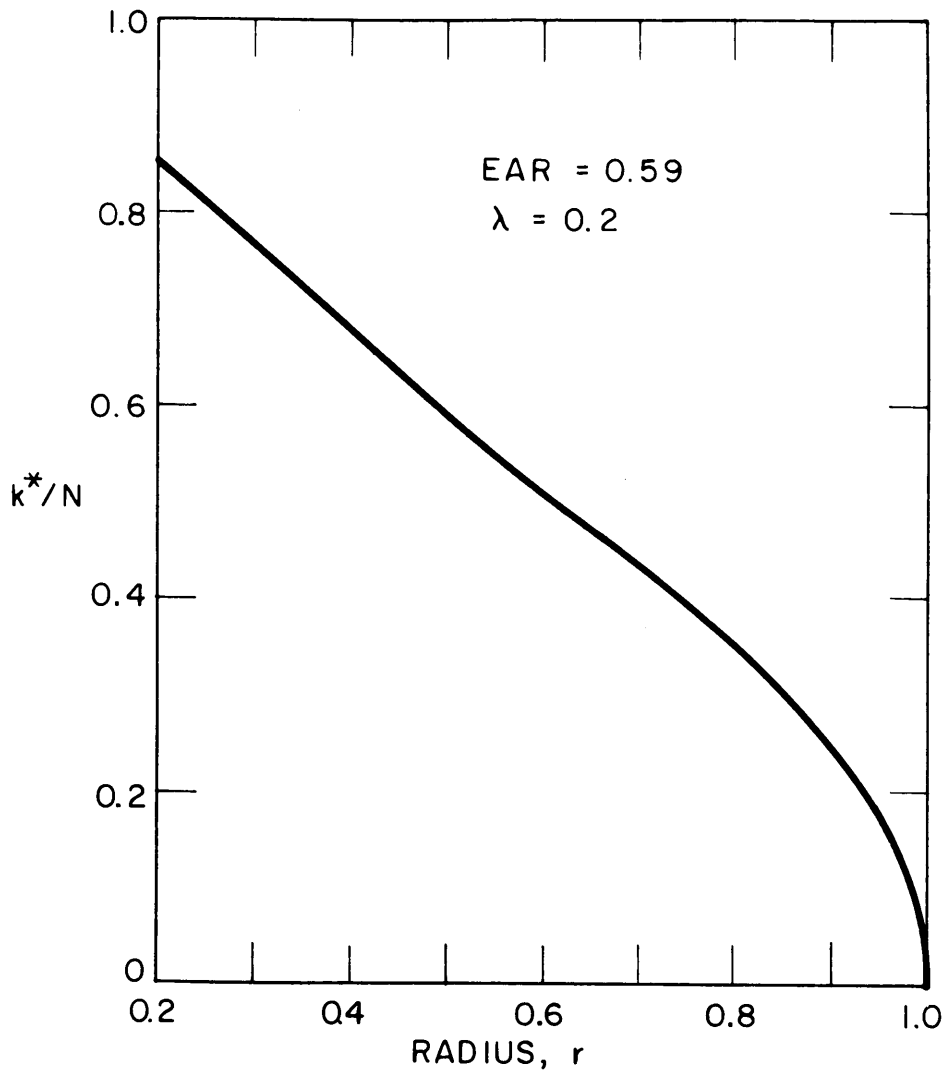


FIG. 8.4 REDUCED FREQUENCY DISTRIBUTION

The resulting amplitudes and phases according to the three different analyses are shown in Figure 8.4. The general behavior of the three results is the same as for the full width blade. The phase angle, however, does not reach a maximum within the range of harmonic numbers considered.

Of greater interest, perhaps, are the comparisons between the three and two dimensional analyses for both screws. The ratio of the thrust predicted by the 3-D analyses to that of the strip theory is plotted in Fig. 8.5 for both screws. Assuming that the 3-D analysis is correct, these give a measure of the accuracy of the strip theory. At $N = 5$ it can be seen that the strip theory predicts a thrust only ten percent greater than the 3-D analysis. The effect of aspect ratio on the 3-D/2-D thrust factor is seen to be largest at zero frequency and to become less important as the harmonic number increases. The erratic behavior of the curve for the original propeller beyond $N = 7$ is considered an indication that the geometrical approximations made in the three-dimensional analysis are inadequate for these high frequencies and corresponding short wavelengths. Though the deviation is less marked for the higher aspect ratio case, it does not seem likely that in reality the lift would be greater than predicted by strip theory. The portion of the curve for the half area propeller at and beyond $N = 7$ is thus also considered of dubious value. The phase angle differences between the three and two dimensional analyses for the two different blade areas are also shown in Figure 8.5, and are seen to reflect the behavior indicated above.

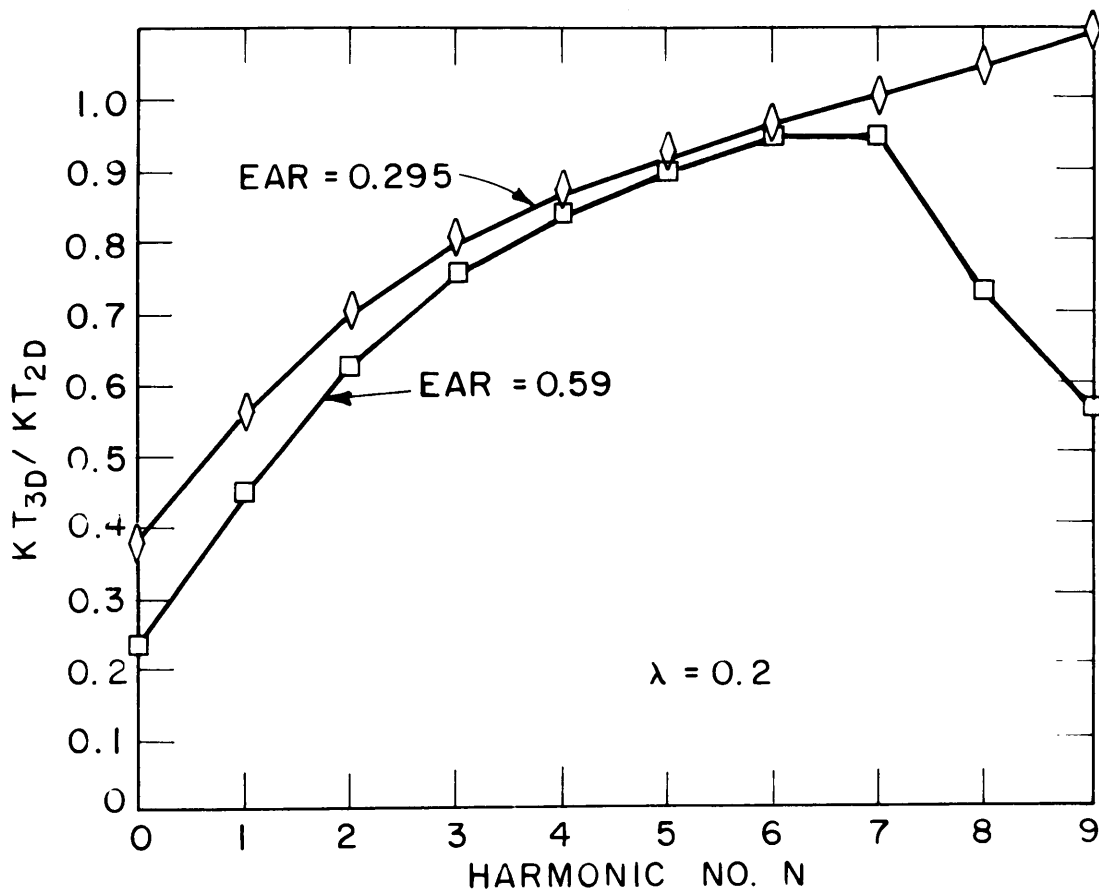
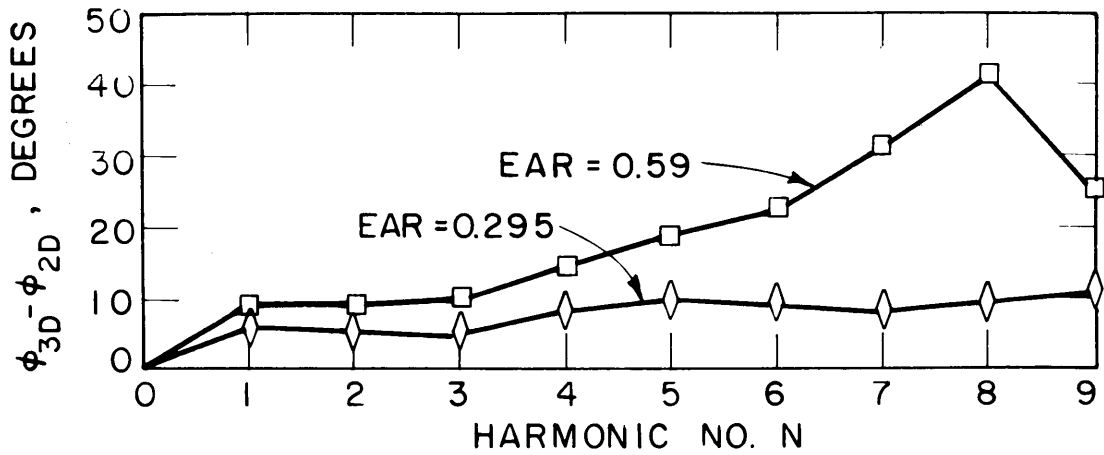


FIG. 8.5 COMPARISON OF BLADE THRUST PREDICTED BY 3-D AND 2-D ANALYSES

Comparison of these curves with similar ones given by Shioiri and Tsakonas (17) show less dependence on aspect ratio than the latter and considerably less correction for three-dimensional effects. Definite conclusions cannot be drawn, however, until comparative computations are made for identical blade shapes and pitch ratios.

An interesting observation may be made by superimposing the amplitude results of Figure 8.4 on those of Figure 8.1. The amplitudes predicted by all three methods are seen to be lower for the narrow bladed propeller at low frequencies, but the reverse is true at high frequencies, the crossover point being in the vicinity of $N = 4$ to 5.

Though predicting phase angles in good agreement with the three-dimensional analysis, the zeroth harmonic approximation is inferior to a quasi-steady analysis for amplitude prediction with low harmonic numbers.

Comparison with Experiment

The blade frequency propeller thrust and torque have been computed by the three-dimensional and strip theory methods for comparison with the experimental results of Chapter VII. The fourth harmonic velocity fields described have been used over a range of values of the advance coefficient covering the experimental range. The experimental and computed results are shown in Figure 8.6.

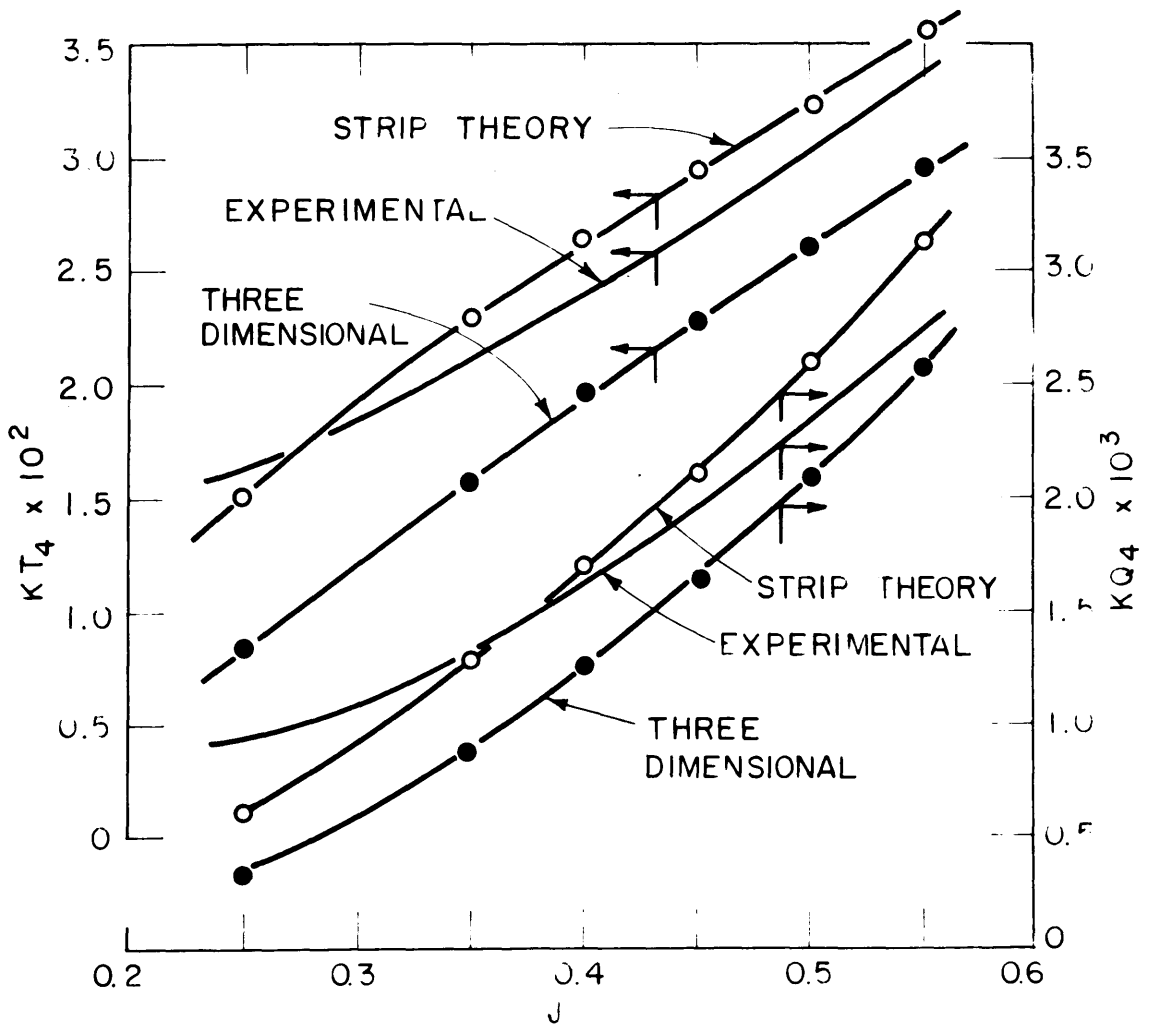
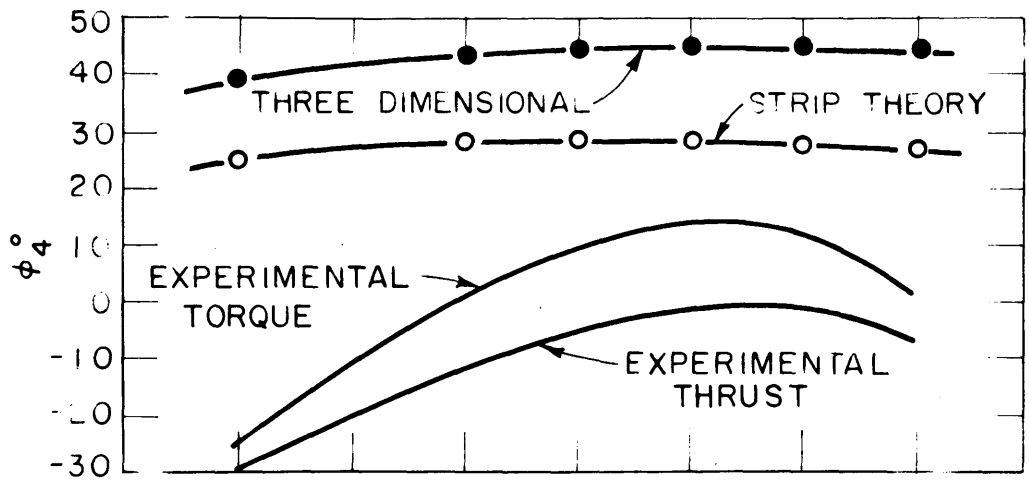


FIG. 8.6 COMPARISON OF COMPUTED AND EXPERIMENTAL RESULTS

The behavior with the advance coefficient of both the computed and experimental results are seen to be generally the same. This propeller has a pitch ratio of 0.612 so that, unfortunately, the experimental results for the most part cover a range of advance coefficients in which the propeller is heavily loaded. For comparisons to be valid under the lightly loaded assumptions of the theory attention must be restricted to the results in the region of the highest values of J .

Regarding the amplitudes, it is seen that the strip theory overestimates both the thrust and torque while the three-dimensional analysis underestimates them. The strip theory is closer to the experimental thrust than the three-dimensional analysis, while the reverse is true for the torque. At $J = 0.55$, the 3-D thrust is in error by 13%, while the torque is in error by 6%.

Regarding the phase angles, the three-dimensional values are seen to lead the experimental by roughly 45° while the strip theory prediction leads by roughly 25° at $J = 0.55$. In the lightly loaded approximation the phase of both the thrust and torque are the same, hence, but one line is shown for each of the two analyses while the experiments result in a phase difference between the components.

The large difference between the computed and experimental phase angles is disturbing. However, it may be noted that a raising of the experimental phase angles by 40° , putting them into agreement with that value computed by the 3-D theory, requires an angular velocity of rotation of the propeller tunnel stream of less than three quarters of one percent of that of the propeller.

It may be noted that the relation of 2-D and 3-D values in the experimental flow field are the same as in the ideal field of Figures 8.1 and 8.2 at $N = 4$ and $\lambda = 0.2$. In both, the strip theory predicts greater forces than the 3-D analysis while the 3-D force leads the other in phase. The experimental amplitudes are seen to fall somewhere between the two theoretical predictions.

Conclusions

The three-dimensional analysis presented here appears to have the proper behavior with regard to frequency. The predicted blade thrust is in agreement with that of the steady flow lifting line model at zero frequency and converges to the strip theory result, at least for amplitudes, for high harmonic numbers. The phase discrepancies between the three-dimensional analysis and the strip theory at high harmonic numbers is believed due to the inadequacy of the three-dimensional model for disturbances of short wavelength.

The strip theory analysis is greatly in error at low harmonic numbers, but in the case of the four bladed propeller considered may be in error by only 15% at the blade frequency. The strip theory consistently predicts larger loads than the three-dimensional analysis. At high harmonic numbers with narrow blades the slightly greater thrust predicted by the 3-D theory is believed inaccurate.

The proposed approximation to the downwash for low harmonic numbers predicts thrust phase angles that are in good agreement with the three-dimensional analysis. However, a quasi-steady lifting line method results in better amplitude agreement at the low harmonic numbers.

Comparison with applicable and dependable experimental data shows that both the three-dimensional analysis and the strip theory predict reasonably accurate blade frequency thrust and torque for the case considered. Comparison of the experimental and computed phase angles, though showing significant discrepancies, is inconclusive because of the possible presence of rotation of the stream in the experiments. The experimental data helps little in deciding whether the strip or 3-D theory is most accurate at the condition considered because of the closeness of their predictions. Experiments designed to be more revealing in this respect are required. Nevertheless, it seems possible to compute the unsteady loads with error of the order of ten percent by either scheme for the case considered.

Precise definition of the range of applicability of strip theory and the range of necessity of three-dimensional analyses must await a series of comparative computations which take into account variations of the important parameters such as harmonic number, blade area, number of blades, and blade shape.

Examination of the angular distribution of the contributions to the induced velocities shows that the effect of the helical nature of the flow field, which has been the subject of much concern, is not of great importance. As in unsteady wing theory, the significant induction effects are due primarily to the near field.

REFERENCES

- (1) Lewis, F.M., "Propeller Vibration", TRANSACTIONS, S.N.A.M.E., Vol. 43, 1935; Vol. 44, 1936.
- (2) Lewis, F.M., and Tachmindji, A.J., "Propeller Forces Exciting Hull Vibration", TRANSACTIONS, S.N.A.M.E., Vol. 62, 1954.
- (3) Manen, J.D. van, and Wereldsma, R., "Dynamic Measurements on Propeller Models", INTERNATIONAL SHIPBUILDING PROGRESS, Vol. 6, No. 63, Nov. 1959.
- (4) Manen, J.D. van, and Wereldsma, R., "Propeller Excited Vibratory Forces in the Shaft of a Single Screw Tanker", Netherlands Research Centre TNO, for Shipbuilding and Navigation, Amsterdam, Report No. 37M, June 1960.
- (5) Manen, J.D. van, and Kamps, J., "The Effect of Shape of Afterbody on Propulsion", TRANSACTIONS, S.N.A.M.E., Vol. 67, 1959.
- (6) Wereldsma, R., "Experimental Determination of Thrust Eccentricity and Transverse Forces, Generated by a Screw Propeller", INTERNATIONAL SHIPBUILDING PROGRESS, Vol. 9, No. 95, July 1962.
- (7) Krohn, J.K., "Numerical and Experimental Investigations on the Dependence of the Fluctuations of Thrust and Torque on the Blade Area Ratio of Four-Blade Ship Propellers", Hamburg Model Basin, HSVA Report No. 1236, May 1961.
- (8) Krohn, J.K., "Numerical and Experimental Investigations on the Dependence of Transverse Force and Bending Moment Fluctuations on the Blade Area Ratio of Five-Bladed Ship Propellers", Hamburg Model Basin, HSVA Report No. 1268, May 1962.
- (9) Krohn, J.K., and Wereldsma, R., "Comparative Model Tests on Dynamic Propeller Forces", INTERNATIONAL SHIPBUILDING PROGRESS, Vol. 7, No. 76, Dec. 1960.
- (10) Lewis, F.M., "Propeller-Vibration Forces", TRANSACTIONS, S.N.A.M.E., Vol. 71, 1963.
- (11) Tachmindji, A.J., and Dickerson, M.C., "The Measurement of Thrust Fluctuations and Free Space Oscillating Pressures for a Propeller", DTMB Report No. 1107, Jan. 1957.

- (12) Manen, J.D. van, "Invloed van de Ongelijkmatigheid van het Snelheidsveld op het Ontwerp van Scheepsschroeven", Het Nederlandsch Scheepsbouwkundig Proefstation te Wageningen, Publicatie No. 100, 1951.
- (13) Ritger, P.D., and Breslin, J.P., "A Theory for the Quasi-Steady and Unsteady Thrust and Torque of a Propeller in a Ship Wake", ETT Report No. 686, July 1958.
- (14) Tsakonas, S., and Jacobs, W.R., "Theoretical Calculations of Vibratory Thrust and Torque and Comparisons with Experimental Measurements", Stevens Institute of Technology, Davidson Laboratory, Letter Report 827, Feb. 1961.
- (15) Hanaoka, T., "Hydrodynamics of an Oscillating Screw Propeller", Fourth Symposium on Naval Hydrodynamics, Office of Naval Research, Department of the Navy, ACR-73, Vol. 1, August 1962.
- (16) Joosen, W.P.A., "Lifting-Line Theory for Shipscrews in Non-Uniform Flow", Netherlands Ship Model Basin, Laboratory Memorandum No. 9, Jan. 1963.
- (17) Shioiri, J., and Tsakonas, S., "Three-Dimensional Approach to the Gust Problem for a Screw Propeller", Stevens Institute of Technology, Davidson Laboratory, Report 940, March 1963.
- (18) Robinson, A., and Laurmann, J.A., "Wing Theory", Cambridge University Press, 1956.
- X (19) Ashley, H., Biplinghoff, R.L., and Halfman, R.L., "Aeroelasticity", Addison-Wesley Publishing Co., Inc. Cambridge, Massachusetts, 1955.
- (20) Karman, T. Von, and Sears, W.R., "Airfoil Theory for Non-Uniform Motion", Journal of the Aeronautical Sciences, Vol. 5, No. 10, August 1938.
- (21) Sears, W.R., "Some Aspects of Non-Stationary Airfoil Theory and its Practical Application", Journal of the Aeronautical Sciences, Vol. 8, No. 3, Jan. 1941.
- (22) Kemp, N.H., "On the Lift and Circulation of Airfoils in Some Unsteady Flow Problems", Journal of the Aeronautical Sciences, Vol. 19, No. 10, Oct. 1952.
- (23) Lerbs, H.W., "Moderately Loaded Propellers with a Finite Number of Blades and an Arbitrary Distribution of Circulation", TRANSACTIONS, S.N.A.M.E., Vol. 60, 1952.

- (24) Kerwin, J.E., "The Solution of Propeller Lifting Surface Problems by Vortex Lattice Methods", Massachusetts Institute of Technology, Dept. of Naval Architecture and Marine Engineering, June 1961.
- (25) Reissner, E., "On the General Theory of Thin Airfoils for Non-uniform Motion", National Advisory Committee for Aeronautics, Technical Note No. 946, Aug. 1944.
- (26) Laidlaw, W.R., "Theoretical and Experimental Pressure Distributions on Low Aspect Ratio Wings Oscillating in an Incompressible Flow", Massachusetts Institute of Technology, Aeroelastic and Structures Research Laboratory, Technical Report 51-2, Sept. 1954.
- (27) Glauert, H., "The Elements of Airfoil and Airscrew Theory", Sec. Ed., Cambridge University Press, 1948.
- (28) Abbot, I.H., and Doenhoff, A.E. von, "Theory of Wing Sections", Dover Publications, Inc., New York, 1959.
- (29) Hildebrand, F.B., "Introduction to Numerical Analysis", McGraw-Hill Book Co., Inc., New York, 1956.
- (30) Jahnke, E., and Emde, F., "Tables of Functions", Dover Publications, Inc., New York, 1945.
- (31) "The Calculation of Goldstein Factors for Three, Four, Five and Six-Bladed Propellers", DTMB Report No. 1034, March 1956.
- (32) Lammeren, W.P.A. van, "Testing Screw Propellers in a Cavitation Tunnel with Controllable Velocity Distribution over the Screw Disk", TRANSACTIONS, S.N.A.M.E., Vol. 63, 1955.
- (33) Lewis, F.M., and Auslander, J., "Virtual Inertial of Propellers", Journal of Ship Research, Vol. 3 , No. 4 , March 1960.
- (34) Visser, N.J., "Model Tests Concerning the Damping Coefficient and the Increase in the Moment of Inertia Due to Entrained Water of Ship's Propellers", Netherlands Research Centre TNO for Shipbuilding and Navigation, Amsterdam, Report No. 31M, April 1960.
- (35) Wrench, J.W., Jr., "The Calculation of Propeller Induction Factors", DTMB Report No. 1116, 1957.

APPENDICES

APPENDIX A

DERIVATION OF THE CIRCULATION OF AN AIRFOIL IN
SINUSOIDAL GUSTS

Consider a flat plate two-dimensional airfoil of chord length $2b$ flying horizontally with zero average angle of attack with velocity U through a series of vertical sinusoidal gusts of amplitude \bar{w}' . Let the leading edge be the origin of coordinates and denote dimensional quantities by primes.

The vertical velocity due to the gusts at position x' of the foil chord at time t is given by:

$$w'(x',t) = \bar{w}' e^{i\omega(t-x'/U)} \tag{A.1}$$

Now making the x coordinate dimensionless on the basis of b :

$$\left. \begin{aligned} x' &= bx \\ \omega x'/U &= \left(\frac{\omega b}{U}\right) x = kx \end{aligned} \right\} \tag{A.2}$$

this becomes:

$$w'(x,t) = \bar{w}' e^{i\omega t} e^{-ikx} \tag{A.3}$$

The boundary condition for the flat plate airfoil at zero angle of attack, where the normal velocity induced at the airfoil by its own bound vorticity is denoted \bar{w}'_i , is written simply:

$$\bar{w}'(x) + \bar{w}'_i(x) = 0 \quad (0 \leq x \leq 2b) \tag{A.4}$$

If now the quasi-steady bound vorticity over the chord of the foil is given in the form of a complex Birnbaum series: (27) (28)

$$\bar{\gamma} = 2\bar{A}_0 \cot \frac{\psi}{2} + 2 \sum_{n=1}^{\infty} \bar{A}_n \sin n \psi \quad (\text{A.5})$$

where:

$$x = 1 - \cos \psi \quad (\text{A.6})$$

then the induced velocity is given by:

$$\frac{\bar{w}'_i}{U} = -\bar{A}_0 + \sum_{n=1}^{\infty} \bar{A}_n \cos n \psi \quad (\text{A.7})$$

Using the dimensionless form of the velocities:

$$\left. \begin{aligned} \bar{w}'_i &= \bar{w}_i U \\ \bar{w}' &= \bar{w} U \end{aligned} \right\} \quad (\text{A.8})$$

the boundary condition may be rewritten:

$$\bar{w} e^{-ikx} - \bar{A}_0 + \sum_{n=1}^{\infty} \bar{A}_n \cos n \psi = 0 \quad (\text{A.9})$$

or:

$$(\bar{w} e^{-ikx}) e^{ikx} \cos \psi = \bar{A}_0 - \sum_{n=1}^{\infty} \bar{A}_n \cos n \psi \quad (\text{A.10})$$

Now the circulation is given by: (27)

$$\frac{\bar{\Gamma}'}{2\pi bU} = \frac{\bar{\Gamma}}{2\pi} = \bar{A}_0 + \frac{1}{2} \bar{A}_1 \quad (\text{A.11})$$

so we must solve for the coefficients \bar{A}_0 and \bar{A}_1 . Multiplying both sides of (A.10) by $d\psi$ and integrating from 0 to π there results:

$$\pi \bar{A}_0 = \bar{w} e^{-ik^*} \int_0^{\pi} e^{ik^* \cos \psi} d\psi \quad (\text{A.12})$$

or: (30)

$$\bar{A}_0 = \bar{w} e^{-ik^*} J_0(k^*) \quad (\text{A.13})$$

Multiplying both sides of (A.10) by $\cos \psi d\psi$ and integrating from 0 to π there results:

$$\frac{\pi}{2} \bar{A}_1 = -\bar{w} e^{-ik^*} \int_0^{\pi} e^{ik^* \cos \psi} \cos \psi d\psi \quad (\text{A.14})$$

or: (30)

$$\bar{A}_1 = -2i \bar{w} e^{-ik^*} J_1(k^*) \quad (\text{A.15})$$

The dimensionless quasi-steady circulation is therefore given by:

$$\frac{\bar{\Gamma}}{2\pi} = \bar{w} e^{-ik^*} \left[J_0(k^*) - iJ_1(k^*) \right] \quad (\text{A.16})$$

The above is with respect to the gust velocity at the leading edge. Shifting the origin to the midchord this becomes:

$$\frac{\bar{\Gamma}}{2\pi} = \bar{w} \left[J_0(\bar{k}^*) - iJ_1(\bar{k}^*) \right] \quad (A.17)$$

Now according to Kemp (22) the unsteady circulation is directly derivable from the quasi-steady circulation by the formula:

$$\bar{\Gamma}_{us} = \bar{\Gamma}_{qs} e^{-i\bar{k}^*} S(\bar{k}^*) \quad (A.18)$$

where $S(\bar{k}^*)$ is the Sears function:

$$S(\bar{k}^*) = 1/i\bar{k}^* \left[K_0(i\bar{k}^*) + K_1(i\bar{k}^*) \right] \quad (A.19)$$

Forming the product of (A.18) there results:

$$\frac{\bar{\Gamma}_{us}}{2\pi\bar{w}} = -i \frac{\left[J_0(\bar{k}^*) - i J_1(\bar{k}^*) \right]}{\bar{k}^* \left[K_0(i\bar{k}^*) + K_1(i\bar{k}^*) \right]} e^{-i\bar{k}^*} \quad (A.20)$$

which is equivalent to (4.20) whth $s_m = 0$

APPENDIX B

FORM OF THE RADIAL VORTICITY INTEGRAND FOR
SMALL φ at $\eta = 1$

Consider the integrand of (3.15) exclusive of the factor $e^{-iN\varphi}$. As $\varphi \rightarrow 0$ with $\eta_1 < 1 < \eta_2$, the evaluation of the bracketed expression becomes:

$$\left[\frac{\eta - \cos\varphi}{(\eta^2 - 2\eta \cos\varphi + p^2 \varphi^2 + 1)^{1/2}} \right]_{\eta_1}^{\eta_2} = \frac{\eta_2 - 1 + \varphi^2/2}{[(\eta_2 - 1)^2 + (\eta_2 + p^2) \varphi^2]^{1/2}} - \frac{\eta_1 - 1 + \varphi^2/2}{[(\eta_1 - 1)^2 + (\eta_1 + p^2) \varphi^2]^{1/2}}$$

$$= \frac{(\eta_2 - 1) + \varphi^2/2}{[(\eta_2 - 1)^2 + (\eta_2 + p^2) \varphi^2]^{1/2}} + \frac{(1 - \eta_1) - \varphi^2/2}{[(1 - \eta_1)^2 + (\eta_1 + p^2) \varphi^2]^{1/2}}$$

(B.1)

Expanding the denominators by the binomial theorem:

$$\left[(\eta_2 - 1)^2 + (\eta_2 + p^2) \varphi^2 \right]^{-1/2} = (\eta_2 - 1)^{-1} - \frac{1}{2} (\eta_2 - 1)^{-3} (\eta_2 + p^2) \varphi^2$$

$$+ \frac{3}{8} (\eta_2 - 1)^{-5} (\eta_2 + p^2)^2 \varphi^4 - \dots$$

(B.2)

and:

$$\left[(1 - \eta_1)^2 + (\eta_1 + p^2) \varphi^2 \right]^{-1/2} = (1 - \eta_1)^{-1} - \frac{1}{2} (1 - \eta_1)^{-3} (\eta_1 + p^2) \varphi^2$$

$$+ \frac{3}{8} (1 - \eta_1)^{-5} (\eta_1 + p^2)^2 \varphi^4 - \dots$$

(B.3)

The right hand side of equation (B.1) may now be written:

$$\begin{aligned}
 & 1 - \frac{1}{2} (\eta_1 - 1)^{-2} (\eta_2 + p^2) \varphi^2 + \frac{3}{8} (\eta_2 - 1)^{-4} (\eta_2 + p^2) \varphi^2 - \dots \\
 & + 1 - \frac{1}{2} (1 - \eta_1)^{-2} (\eta_1 + p^2) \varphi^2 + \frac{3}{8} (1 - \eta_1)^{-4} (\eta_1 + p^2)^2 \varphi^4 - \dots \\
 & + \frac{\varphi^2}{2} (\eta_2 - 1)^{-1} - \frac{\varphi^4}{4} (\eta_2 - 1)^{-3} (\eta_2 + p^2) + \frac{3}{16} \varphi^6 (\eta_2 - 1)^{-5} (\eta_2 + p^2)^2 - \dots \\
 & - \frac{\varphi^2}{2} (1 - \eta_1)^{-1} + \frac{\varphi^4}{4} (1 - \eta_1)^{-3} (\eta_1 + p^2) - \frac{3}{16} \varphi^6 (1 - \eta_1)^{-5} (\eta_1 + p^2)^2 + \dots \\
 & = 2 + \frac{\varphi^2}{2} \left[\frac{1}{(\eta_2 - 1)} - \frac{1}{(1 - \eta_1)} - \frac{(\eta_2 + p^2)}{(\eta_2 - 1)^2} - \frac{(\eta_1 + p^2)}{(1 - \eta_1)^2} \right] \\
 & + \frac{\varphi^4}{4} \left[\frac{(\eta_1 + p^2)}{(1 - \eta_1)^3} - \frac{(\eta_2 + p^2)}{(\eta_2 - 1)^3} + \frac{3}{2} \frac{(\eta_2 + p^2)^2}{(\eta_2 - 1)^4} + \frac{3}{2} \frac{(\eta_1 + p^2)^2}{(1 - \eta_1)^4} \right] \\
 & + \varphi^6 [\dots] + \dots \\
 & = 2 + A\varphi^2 + B\varphi^4 + \dots
 \end{aligned}$$

(B.4)

As $\varphi \rightarrow 0$ the factor on the left in (3.15) becomes:

$$\left(\frac{\sin \varphi + p^2 \varphi \cos \varphi}{\sin^2 \varphi + p^2 \varphi^2} \right) \rightarrow \frac{1}{\varphi} - \frac{\varphi}{6} \frac{(1 + 3p^2)}{(1 + p^2)}$$

(B.5)

Forming the entire expression, there results:

$$\left\{ \left(\frac{\sin \varphi + p^2 \varphi \cos \varphi}{\sin^2 \varphi + p^2 \varphi^2} \right) \left[\frac{\eta - \cos \varphi}{(\eta^2 - 2\eta \cos \varphi + p^2 \varphi^2 + 1)^{1/2}} \right]_{\eta_1}^{\eta_2} - \frac{2}{\varphi} \right\} +$$

$$\left[A - \frac{1}{3} \left(\frac{1 + 3p^2}{1 + p^2} \right) \right] \varphi + \left[B - \frac{A}{6} \left(\frac{1 + 3p^2}{1 + p^2} \right) \right] \varphi^3 + \dots \quad (\text{B.6})$$

BIOGRAPHICAL NOTE

The author is an instructor in the Department of Naval Architecture and Marine Engineering at the Massachusetts Institute of Technology. He was born February 13, 1936 in Boston and attended public schools in Revere and Swampscott, Massachusetts. He received a B.S. in Naval Architecture and Marine Engineering from Webb Institute of Naval Architecture in July 1957. The author entered the graduate school of M.I.T. in that year, receiving an M.S. in Naval Architecture and Marine Engineering in February, 1958. He began a doctoral program while engaged part-time as a teaching and research assistant. Concurrent work at the General Electric Co. in computer aided engineering analysis culminated in August 1962 in a report entitled, "Periodic Forces on the Rotor Blades of a Turbine Stage". During the 1962-1963 academic year, he was a Fulbright Scholar at the Technical University of Delft, The Netherlands, engaged in original experimental research in unsteady propeller operation, the results of which are presented as part of this thesis.